

GENERATION OF EXTREMELY LOW FREQUENCY WAVES  
VIA MODULATED IONOSPHERIC HEATING FOR  
COMMUNICATIONS APPLICATIONS

A DISSERTATION  
SUBMITTED TO THE DEPARTMENT OF  
ELECTRICAL ENGINEERING  
AND THE COMMITTEE ON GRADUATE STUDIES  
OF STANFORD UNIVERSITY  
IN PARTIAL FULFILLMENT OF THE REQUIREMENTS  
FOR THE DEGREE OF  
DOCTOR OF PHILOSOPHY

George Jin  
December 2012

© 2012 by George YunHao Jin. All Rights Reserved.

Re-distributed by Stanford University under license with the author.



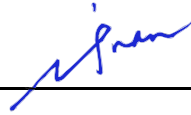
This work is licensed under a Creative Commons Attribution-Noncommercial 3.0 United States License.

<http://creativecommons.org/licenses/by-nc/3.0/us/>

This dissertation is online at: <http://purl.stanford.edu/jr013bh0187>

George Jin

I certify that I have read this dissertation and that, in my opinion, it is fully adequate in scope and quality as a dissertation for the degree of Doctor of Philosophy.



---

(Umran S. Inan) Principal Adviser

I certify that I have read this dissertation and that, in my opinion, it is fully adequate in scope and quality as a dissertation for the degree of Doctor of Philosophy.



---

(Maria Spasojevic)

I certify that I have read this dissertation and that, in my opinion, it is fully adequate in scope and quality as a dissertation for the degree of Doctor of Philosophy.



---

(Donald C. Cox)

Approved for the University Committee on Graduate Studies

---

# Abstract

Extremely low frequency (ELF) electromagnetic waves (0.3–3 kHz) have many applications including communications with submerged submarines, remote sensing of the lower ionosphere, and active wave-particle interaction experiments involving energetic particles trapped in Earth’s radiation belts. However, waves in this frequency range are difficult to generate due to their large wavelengths ( $\sim 100$ – $1000$  km) and therefore the large antennas required for efficient radiation. One relatively new and unconventional technique for ELF generation uses modulated heating of the lower ionosphere. The modulated ionospheric heating technique utilizes a high frequency beam (HF, 3–10 MHz) amplitude modulated at ELF frequencies to create a time-varying change in the conductivity of the lower ionosphere. When performed in regions where natural, large-scale horizontal ionospheric currents exist, such as the auroral electrojet at polar latitudes, the conductivity change results in a time-varying current that radiates at the ELF modulation frequency. While sidestepping the challenges of constructing a conventional ELF antenna, the modulated heating technique introduces new difficulties. The amplitude of the ELF waves depends strongly on the strength of the electrojet and the conversion between HF power and the ELF field is highly nonlinear. The purpose of this work is to characterize the dependence on electrojet strength and mitigate or utilize the nonlinearity between HF power and ELF fields so that experimenters and communication systems operators can optimize the generation of ELF waves using modulated ionospheric heating.

First, we explore how the generation of ELF waves via modulated heating is affected by the ambient ionospheric conditions and construct a model to predict ELF

generation efficiency using several ionospheric diagnostic instruments. The amplitude of generated ELF waves is typically linearly correlated with the strength of the overhead electrojet current as estimated by magnetic deflections measured by ground-based magnetometers. However, the slope of this correlation is highly dependent on the ambient ionospheric electron number density, which is highly variable at auroral latitudes. Higher ionospheric density results in a large increase in the electrojet current strength but only a small increase in the generated ELF amplitude while lower ionospheric density can result in a weaker electrojet but only a small decrease in ELF generation.

Next, we attempt to minimize the harmonic distortion produced by the nonlinear conversion of HF wave energy to ELF wave energy. Modulated heating using sinusoidal amplitude modulation generates ELF waves at integer multiples of the modulation frequency with 1.3% of the total power outside the fundamental harmonic. The harmonic content results from the nonlinear relationship between HF power and the modulated ionospheric conductivity. By inverting a numerical model of HF ionospheric heating, we show that harmonic content can be reduced by transmitting a predistorted HF power envelope that results in a sinusoidal ELF current at a particular altitude. This technique depends on a correct model of the ionosphere, which is highly variable in practice. Other modulation envelopes explored, such as square wave modulation, create stronger harmonics but can also result in higher generated ELF power or greater efficiency.

Finally, we examine how the variability in ELF generation as well as the harmonic content of the ELF waves affects an ELF communications system. We conduct experiments using quaternary phase shift keying (QPSK) to transmit digital data and examine how the bit error rate (BER) varies with generation conditions and changes in transmitter parameters. Variations in received signal-to-noise ratio caused by changes in natural conditions changes the BER by several orders of magnitude. Square wave modulation also reduces bit error rate compared to sine wave modulation since it generates stronger ELF signals and stronger harmonics. Simulations of the QPSK signal show that using additional harmonics can improve the bit error rate, but only when the harmonics are below  $\sim 4.5$  kHz. Mathematical models of the ELF

noise environment show that including harmonics at frequencies above  $\sim 4.5$  kHz can worsen the BER because the noise at these frequencies is highly impulsive.

# Acknowledgements

I am grateful for the support of many individuals who have helped me throughout my research at Stanford and have directly or indirectly contributed to this thesis. First, I thank my advisor, Professor Umran Inan, who welcomed me to the group over five years ago and immediately started me on a path to this thesis. His insight and encyclopedic knowledge of space science are valuable tools in helping my analysis. Just as valuable is his concern for his students' professional development and his willingness to listen to whatever problems or protests arise. Lastly, I thank him for trusting me with field trips to amazing destinations despite what I suspect were his doubts on my fortitude. I'd also like to thank Professor Don Cox for serving on my thesis committee and for our conversations on digital communications at HAARP, as well as Professor Ada Poon for chairing my oral exam committee. Finally, I am very fortunate to have Maria Spasojevic as a mentor. Although her expertise in magnetospheric physics seems like an odd pairing for my ionospheric research, her ability to take complex geophysical systems and boil them down to understandable scientific results was invaluable. Besides analysis skills, she has also been a great aid in developing presentation, writing, and reviewing skills as well as being a social catalyst in assembling the group for happy hours and lunch outings.

HAARP research in the VLF group has been taken place long before my arrival. I am lucky that the work of many others to install receivers, design experiments, and write analysis scripts allowed me to begin research immediately without starting from scratch. Morris Cohen has also been a great mentor and has provided research ideas and model code, secured experimental time, and been the resident expert on HF heating. I also thank Marek Gołkowski, Denys Pidtyachiy, and Nikolai Lehtinen

for their help in HAARP experimental campaigns and modeling. Of course none of the experiments would be possible without the HAARP operators, including Mike McCarrick, Helio Zwi, and David Seafolk-Kopp.

Much credit goes to Shaolan Min and Helen Niu for their work in administering the group, as well as Dan Musetescu for managing the absurd volume of data that passes between Alaska and Stanford, and Jeff Chang for keeping the VLF receiver infrastructure humming smoothly. The senior staff, postdocs, and students in the VLF group have all been a pleasure to work with. Dan Golden, Forrest Foust, Patrick Blaes, and David Strauss have even been useful in their efforts to install and maintain the cluster and servers that make all our lives easier. Kevin Graf and Nick LaVassar have been great friends both inside and outside Packard. Naoshin Haque, Nick Bunch, Fadi Zoghzoghy, Justin Li, Salman Naqvi, Rasoul Kabirzadeh, Vijay Harid, Drew Compston, Bob Marshall, Can Liang, Brant Carlson, and Ryan Said are just some of the other group members I'd like to thank. Outside the group, Austin Lu and Brenna Fong have also been a reliable source of procrastination and stress relief whenever I needed a break from research.

Finally, my uncle William and aunt Linda have been gracious in providing me a home away from home in the Bay Area, and my parents' support have helped me through my time at Stanford.

GEORGE JIN  
*Stanford, California*  
*December 7, 2012*

This research has been carried out with support from HAARP, Office of Naval Research, Air Force Research Laboratory, and Defense Advanced Projects Research Agency, via ONR grants N00014-05-C-0308 and N0014-09-1-0100 and AFRL award FA9453-11-C-0011 to Stanford University, and by a Stanford Graduate Fellowship. Thanks go to Jens Østergaard for maintaining the HAARP riometer and Bill Bristow for assisting with SuperDARN data.



# Contents

|  |            |
|--|------------|
| <b>Abstract</b>  | <b>iv</b>  |
| <b>Acknowledgements</b>                                  | <b>vii</b> |
| <b>1 Introduction</b>                                    | <b>1</b>   |
| 1.1 Extremely Low and Very Low Frequency Waves . . . . . | 1          |
| 1.2 The Ionosphere . . . . .                             | 5          |
| 1.2.1 Ionospheric Instruments . . . . .                  | 8          |
| 1.2.2 Ionospheric Models . . . . .                       | 9          |
| 1.3 Ionospheric Currents . . . . .                       | 9          |
| 1.4 Modulated Heating . . . . .                          | 11         |
| 1.4.1 Early Experiments . . . . .                        | 13         |
| 1.4.2 Tromsø, Norway . . . . .                           | 14         |
| 1.4.3 Other heating facilities . . . . .                 | 16         |
| 1.4.4 HAARP . . . . .                                    | 17         |
| 1.5 Contributions and Approach . . . . .                 | 18         |
| <b>2 HF Heating: Theory and Modeling</b>                 | <b>21</b>  |
| 2.1 Plasma Fundamentals . . . . .                        | 21         |
| 2.2 HF Heating of Electrons . . . . .                    | 22         |
| 2.3 Plasma Conductivity . . . . .                        | 23         |
| 2.4 HF Propagation . . . . .                             | 28         |
| 2.4.1 HF Absorption and Refraction . . . . .             | 28         |
| 2.4.2 1-D Model . . . . .                                | 30         |

|          |  |           |
|----------|--|-----------|
| 2.4.3    | Extension to 3-D . . . . .                           | 33        |
| 2.5      | VLF propagation . . . . .                            | 34        |
| <b>3</b> | <b>Relating ELF Generation to Natural Conditions</b> | <b>38</b> |
| 3.1      | Methodology . . . . .                                | 39        |
| 3.2      | Case Studies . . . . .                               | 42        |
| 3.2.1    | Strong, Positive Correlation . . . . .               | 42        |
| 3.2.2    | Strong Negative Correlation . . . . .                | 46        |
| 3.2.3    | Poor Correlation . . . . .                           | 48        |
| 3.3      | Statistics: Occurrence Probability . . . . .         | 48        |
| 3.4      | Statistics: Correlation . . . . .                    | 52        |
| 3.5      | Expanded Dataset and Observations . . . . .          | 54        |
| 3.6      | Statistical Model . . . . .                          | 58        |
| 3.6.1    | Methodology . . . . .                                | 58        |
| 3.6.2    | Riometer Results . . . . .                           | 62        |
| 3.6.3    | Ionosonde results . . . . .                          | 63        |
| 3.7      | Experimental Summary . . . . .                       | 65        |
| <b>4</b> | <b>Modeling ELF Generation</b>                       | <b>67</b> |
| 4.1      | Theoretical Basis . . . . .                          | 67        |
| 4.2      | Theoretical Modeling . . . . .                       | 69        |
| 4.2.1    | Methodology . . . . .                                | 69        |
| 4.2.2    | Model Inputs . . . . .                               | 70        |
| 4.2.3    | Model Results . . . . .                              | 71        |
| 4.3      | Discussion . . . . .                                 | 75        |
| <b>5</b> | <b>Harmonic Distortion and Modulation Waveforms</b>  | <b>78</b> |
| 5.1      | Background . . . . .                                 | 79        |
| 5.2      | Methodology . . . . .                                | 80        |
| 5.3      | Numerical Modeling . . . . .                         | 82        |
| 5.4      | Experimental Results . . . . .                       | 87        |
| 5.4.1    | Harmonic Minimization . . . . .                      | 87        |

|          |  |            |
|----------|--|------------|
| 5.4.2    | Total Power and Efficiency . . . . .                       | 89         |
| 5.5      | Heating and Cooling Time Constants . . . . .               | 92         |
| 5.6      | Summary . . . . .  | 93         |
| <b>6</b> | <b>ELF Communications with Modulated Heating</b>           | <b>95</b>  |
| 6.1      | Phase Shift Keying . . . . .                               | 97         |
| 6.2      | Experimental Summary . . . . .                             | 98         |
| 6.3      | Simulations . . . . .                                      | 103        |
| 6.4      | Theoretical Performance Models . . . . .                   | 105        |
| 6.5      | Conclusion . . . . .                                       | 110        |
| <b>7</b> | <b>Conclusions and Future Work</b>                         | <b>112</b> |
| 7.1      | Conclusions . . . . .                                      | 112        |
| 7.2      | Future Work . . . . .                                      | 115        |
| 7.2.1    | Correlation with radar data . . . . .                      | 115        |
| 7.2.2    | Electrojet spatial structure . . . . .                     | 115        |
| 7.2.3    | Harmonic minimization with feedback from ELF measurements  | 116        |
| 7.2.4    | Spread spectrum communications and modulated heating . . . | 116        |

# List of Tables

|     |  |    |
|-----|--|----|
| 3.1 | Neural networks constructed . . . . .                                | 59 |
| 5.1 | Inv-sin second harmonic with different ionospheres . . . . .         | 85 |
| 5.2 | Sinusoidal modulation second harmonic with different ionospheres . . | 85 |
| 5.3 | Experimental summary of modulation waveforms . . . . .               | 91 |

# List of Figures

|      |  |    |
|------|--|----|
| 1.1  | Cartoon depicting some applications of ELF/VLF waves . . . . .                             | 3  |
| 1.2  | Typical densities of various species in the ionosphere . . . . .                           | 6  |
| 1.3  | The auroral electrojet system . . . . .  | 10 |
| 1.4  | Modulated heating cartoon . . . . .  | 12 |
| 2.1  | Ions and electrons undergoing E cross B drift. . . . .                                     | 25 |
| 2.2  | Plasma parameters responding to sinusoidal HF heating . . . . .                            | 27 |
| 2.3  | Hall conductivity over time at a set of altitudes . . . . .                                | 32 |
| 2.4  | Hall and Pedersen conductivity at various altitudes . . . . .                              | 33 |
| 2.5  | HAARP HF beam pattern at 2.75 MHz and 60 km altitude . . . . .                             | 34 |
| 2.6  | Horizontal component of B-field magnitude on the ground from the full wave model . . . . . | 36 |
| 3.1  | Spectrogram and filtered amplitude of HAARP generated ELF signals . . . . .                | 40 |
| 3.2  | Case 1: Positive correlation between ELF and $ \Delta H $ . . . . .                        | 43 |
| 3.3  | Case 2: Positive correlation between ELF and $ \Delta H $ with little activity . . . . .   | 44 |
| 3.4  | Case 3: Positive correlation between ELF and $ \Delta H $ with a change in slope . . . . . | 45 |
| 3.5  | Case 4: Negative correlation between ELF and $ \Delta H $ . . . . .                        | 46 |
| 3.6  | Case 5: Poor correlation between ELF and $ \Delta H $ . . . . .                            | 47 |
| 3.7  | ELF amplitude and $ \Delta H $ for all cases . . . . .                                     | 48 |
| 3.8  | Histogram of $ \Delta H $ by ELF amplitude . . . . .                                       | 49 |
| 3.9  | Weakest signals detected at Chistochina . . . . .  | 51 |
| 3.10 | Correlation and slope with respect to peak $ \Delta H $ . . . . .                          | 53 |
| 3.11 | ELF amplitude with data from several diagnostic instruments . . . . .                      | 57 |
| 3.12 | Electrojet current and $ \Delta H $ . . . . .  | 61 |

|      |  |     |
|------|--|-----|
| 3.13 | Nighttime neural network output . . . . .                                    | 63  |
| 3.14 | Daytime neural network output . . . . .                                      | 64  |
| 3.15 | Nighttime neural network output using ionosonde . . . . .                    | 64  |
| 4.1  | Electron density profiles and simulated Hall and Pedersen conductivities     | 71  |
| 4.2  | Ratio of conductivities for most dense and least dense ionospheres . .       | 72  |
| 4.3  | Simulated ELF amplitude and $ \Delta H $ with different ionospheric profiles | 74  |
| 5.1  | HF Power transmission waveforms . . . . .                                    | 81  |
| 5.2  | Simulated Hall conductivity using an inv-sin waveform . . . . .              | 83  |
| 5.3  | Inv-sin Hall conductivity in mismatched ionosphere . . . . .                 | 86  |
| 5.4  | Inv-sin experimental results . . . . .                                       | 88  |
| 5.5  | Power and efficiency at various duty cycles . . . . .                        | 90  |
| 6.1  | Spectrogram of communications experiment . . . . .                           | 96  |
| 6.2  | Bit error rates measured in experiment . . . . .                             | 100 |
| 6.3  | Experimental bit error rates using more harmonics . . . . .                  | 102 |
| 6.4  | Simulated bit error rates . . . . .  | 104 |
| 6.5  | Probability density function of ELF/VLF noise . . . . .                      | 106 |
| 6.6  | Computed bit error rates . . . . .   | 109 |

# Chapter 1

## Introduction

With much of the pioneering work in radio wave generation occurring at ever higher frequencies in the terahertz range (e.g. *Wanke and Lee*, 2011), why is wave generation at the other end of the spectrum an important and interesting topic of study? In this introductory chapter, we address this question by going where only extremely low and very low frequency (ELF/VLF) waves can go, from deep into the Earth's ocean and out to the near-Earth space environment. We then examine the Earth's natural electrical environment and the means by which large-scale currents in the Earth's upper atmosphere can be harnessed to generate ELF/VLF waves.

### 1.1 Extremely Low and Very Low Frequency Waves

The term extremely low frequency (ELF) electromagnetic waves commonly refers to waves with frequencies from 3 Hz to 3 kHz, while very low frequency (VLF) refers to waves with frequencies from 3 kHz to 30 kHz. An interesting feature of the ELF/VLF radio band is that it contains the range of audible frequencies for sound waves (20 Hz–20 kHz). Thus, a simple way to analyze the ELF/VLF band is to simply connect an antenna to a baseband audio amplifier and listen to the output. Many naturally generated electromagnetic emissions such as whistlers, chorus, and hiss were first studied in this way and were given names based on the way they sounded when converted to audio (*Storey*, 1953). Though, a vast amount of research is dedicated

to studying these natural emissions, our focus is on the applications of artificially generated waves.

ELF/VLF waves can be used for communications in spite of the limited bandwidth available at these frequencies. Waves in this frequency range have two primary advantages. First, they reflect from both the ionosphere, a layer of partially ionized gas in the upper atmosphere, and the ground. Thus, they can be guided in the Earth-ionosphere waveguide for long distances with relatively little attenuation and can be used for global communications. Higher frequency waves are restricted to line-of-sight applications and rely on satellites to relay signals over the horizon. Second, ELF/VLF waves can penetrate into seawater and are used by navies to communicate with submarines even when they are submerged. Because of the sensitive nature of military communications, there is little information on this topic in the open literature but *Bernstein et al.* (1974) provides an overview of transmitter, coding, and receiver design. The work also includes an experimental demonstration using the Wisconsin Test Facility (a precursor to the operational Navy ELF transmitters in Wisconsin and Michigan) to transmit a message with a 76 Hz carrier that was successfully received onboard a submerged submarine in the Atlantic Ocean.

Several studies have investigated the challenges of communicating at ELF/VLF frequencies, primarily the impulsive noise environment. The dominant source of noise at ELF/VLF frequencies is from lightning discharges, which generate an impulsive signal known as a radio atmospheric or sferic. While in the analysis of many (non-ELF/VLF) communication systems, noise can be treated simply and accurately with a white Gaussian model, this assumption is not valid in the ELF/VLF band. *Ziemer* (1967) and *Hall* (1966) analyzed the bit error rate (BER) performance of communications receivers optimized for white Gaussian noise in an impulsive noise environment. The measured performance is substantially worse compared to expectations from Gaussian noise particularly at high signal-to-noise ratios. This result is due to the fact that a single strong impulse can cause an error in decoding even a very strong signal. Several other works have proposed non-linear receivers which attempt to deemphasize parts of signals that are “too” strong (*Hall*, 1966; *Bernstein et al.*, 1974; *Ingram*, 1984). *Kassam* (1988, Ch. 3) and the references therein show examples



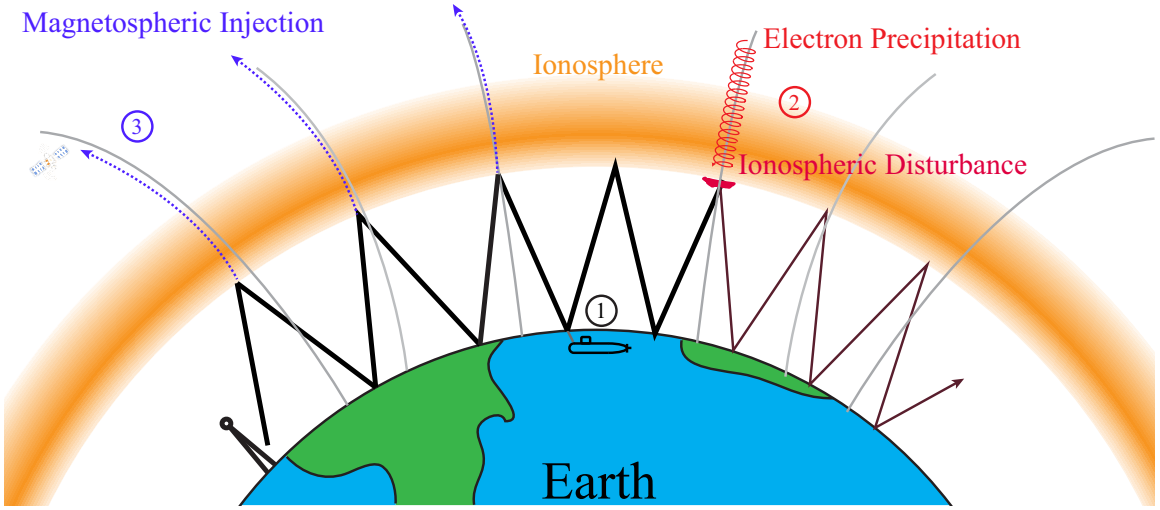


Figure 1.1: Cartoon depicting some applications of ELF/VLF waves including: (1) long-distance propagation in the Earth-ionosphere waveguide and communications with a submerged submarine, (2) remote sensing of an ionospheric disturbance caused by electron precipitation from its effect on waves propagating in the waveguide, and (3) injection of waves into the magnetosphere as they follow electron density irregularities aligned with the Earth’s magnetic field lines (gray).

of the behavior of ELF noise and detecting signals in this noise environment.

ELF/VLF waves are also used in scientific studies. Their ability to penetrate seawater also applies to solid earth. *Velikhov et al.* (1998), discusses the use of ELF waves to perform deep soundings of the Earth’s crust, while also providing some interesting technical details on Zevs, the Russian equivalent to the Navy ELF transmitters.

Besides exploring the Earth, these waves can also probe the upper boundary in the earth-ionosphere waveguide. VLF remote sensing is a technique that exploits the reflection of VLF waves from the lower ionosphere at altitudes from 60–90 km. This region of the atmosphere is difficult to access otherwise because it is unreachable by scientific balloons and is too low for satellites due to orbital drag. A simple receiver can be used to track the amplitude and phase of a VLF transmitter and changes in the received amplitude and phase can be used to remotely sense details of disturbances in the ionosphere along the propagation path due to processes such as lightning induced electron precipitation (*Helliwell et al.*, 1973; *Cotts and Inan*, 2007), solar flares

(*Burgess and Jones, 1969*), auroral electron precipitation (*Thorne and Larsen, 1976; Chevalier et al., 2007*), and ionospheric heating from other transmitters (*Huxley and Ratcliffe, 1949; Graf et al., 2011*).

Although most energy at ELF/VLF is reflected at the ionosphere, some wave energy does leak out into the magnetosphere where it can propagate along the field lines in the so-called “whistler-mode” and where it can resonantly interact with trapped particles in the Earth’s radiation belts. Waves transmitted on the ground are guided along density irregularities aligned with the Earth’s magnetic field lines. The waves can then be received on the ground at the magnetic conjugate point of the transmitter, often with fascinating additional features and properties. Under certain conditions, resonance interactions between the waves and radiation belt particles can amplify the waves, sometimes leading to nonlinear frequency shifts (*Helliwell et al., 1964; Carpenter and Bao, 1983; Gibby et al., 2008; Golkowski et al., 2011*). Figure 1.1 depicts some of these applications, including subionospheric ELF/VLF propagation to a submerged submarine, VLF remote sensing where an ionospheric disturbance affects the VLF wave, and magnetospheric injection where ELF/VLF waves leak through the ionosphere and can propagate in the magnetosphere.

In spite of the rich scientific and practical applications of ELF/VLF waves, only a handful of transmitters operate at these frequencies. For an antenna to radiate efficiently, its length should be similar to a wavelength and VLF waves have wavelengths of between 10-100 km. Navy transmitters, which operate near 20 kHz, use vertical masts that are much smaller than a wavelength but compensate using tuning elements to force the antenna to resonate at that frequency. This type of tuning restricts the transmitter to a very small range of frequencies at which the antenna is resonant, but does allow for reasonable efficiency and reasonably sized antennas. For example, the VLF transmitter at Lualualei, Hawaii (callsign NPM) uses a mast approximately 460 m tall, but smaller VLF transmitters, such as ones equipped on TACAMO (Take Charge And Move Out) can fit on an aircraft (*El-Arini et al., 1990*).

At ELF frequencies however, the wavelengths increase by another order of magnitude and the solutions become more exotic. One way to manage the large-antenna

problem is to construct a horizontal antenna. However, currents flowing in a horizontal antenna induce currents flowing in the opposite direction in the ground below. Because the antenna current and ground current are separated by much less than a wavelength, the two fields largely cancel out, resulting in much lower efficiency. The efficiency can be improved by constructing the antenna over an area with low ground conductivity. For example, the Siple transmitter (*Raghuram et al.*, 1974) operating near 2.5 kHz was constructed over an ice sheet on the Antarctic peninsula, providing some separation from the ground currents. The American and Russian ELF transmitters use an antenna that is grounded at both ends (*Bernstein et al.*, 1974; *Velikhov et al.*, 1998). As long as the ground conductivity is very low, the ground current is forced to travel deep in the earth's crust, and the resulting loop of current flowing through the antenna and the ground can radiate at frequencies below 100 Hz. Very long antennas are also used: 42 km in the case of Siple and 60 km for the Russian Zevs transmitter. More creative solutions include hoisting a vertical antenna on a balloon (*Field et al.*, 1989) or using a wire loop passing between a mountain top and a tunnel through its base (*Barr et al.*, 1993).

A still more exotic means of generating ELF is to modulate natural currents flowing through the ionosphere itself. This technique, referred to as modulated heating, is introduced in the remaining sections.

## 1.2 The Ionosphere

The ionosphere is a region of the upper atmosphere, extending from roughly 60 km above sea level upwards to  $\sim 600$  km. At these altitudes, the gases become partially ionized by solar radiation and are referred to as a plasma. This plasma consists of free electrons, positive and negative ions, as well as neutral molecules. The processes that ionize the neutral gases and recombine the ions depend on altitude and result in the formation of ionospheric layers. The *F*-layer (sometimes divided into the *F2* and *F1*-layers) is the highest and is largely the result of ionization of atomic oxygen from solar radiation with wavelengths below approximately 100 nm. Below that is the *E*-layer where soft X-rays also contribute to much of the ionization of molecular

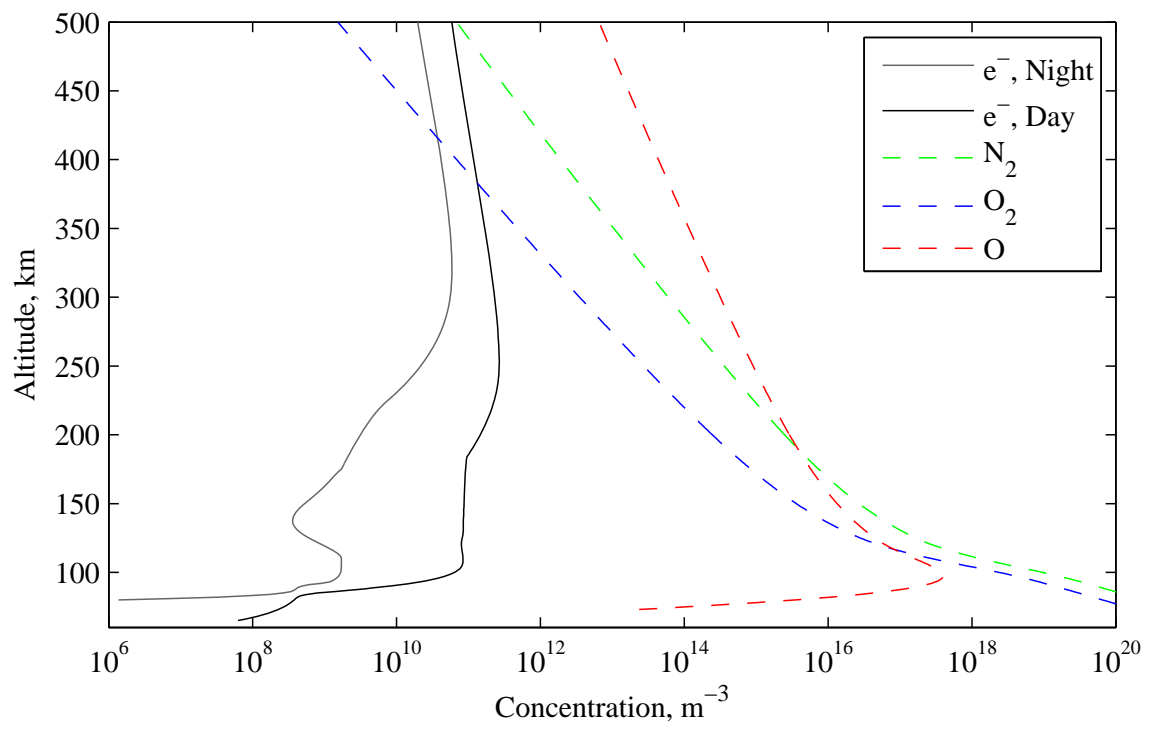


Figure 1.2: Typical densities of various species in the ionosphere

oxygen. Finally, the *D*-layer, lowest in altitude, is ionized during daytime largely by Lyman- $\alpha$  radiation. The *D*-region can have much lower densities at night but is maintained in high-latitude auroral regions by electron precipitation as discussed in the next section.

The most important parameter of the ionosphere is the variation of electron density with altitude as this governs the interaction of the ionosphere with radio waves. The electron density determines the critical or plasma frequency, given by:

$$f_p = \frac{1}{2\pi} \sqrt{\frac{q^2 N_e}{m_e \epsilon_0}} \quad (1.1)$$

This formula is often approximated by  $f_p = 9\sqrt{N_e}$ , where  $f_p$  is the plasma frequency in Hz,  $N_e$  is the electron density in electrons per m<sup>3</sup>,  $q$  is the fundamental charge,  $m_e$  is the mass of the electron, and  $\epsilon_0$  is the permittivity of free space. For example, when the peak electron density in the ionosphere is  $10^{12}$  m<sup>-3</sup>, then the plasma frequency is  $\sim 9$  MHz. If we neglect the effects of collisions between electrons and neutral molecules and the effects of Earth's magnetic field, waves below this frequency are reflected, and waves above this frequency penetrate through the ionosphere.

Though the electron density is a critical parameter of the ionosphere, the composition of the ionosphere, especially in the *D*-region is still dominated by neutral molecules such as molecular nitrogen and oxygen. Collisions between electrons and these neutral molecules also play an important role in the interaction of radio waves with the ionosphere. Figure 1.2 shows the concentrations of electrons and neutral molecules over altitude in the ionosphere. Note that the electron density decreases rapidly in the *D*-region below 90 km and is many orders of magnitude less than the neutral gas density.

### 1.2.1 Ionospheric Instruments

There are several techniques to determine the electron density experimentally. One is to use an ionosonde, an instrument which utilizes the change in plasma frequency with electron density. An ionosonde transmits a pulse at a particular frequency. This

pulse propagates upwards through the ionosphere until it reaches an altitude where the plasma frequency equals the wave frequency, and the pulse is reflected downwards. By measuring the time between reception and transmission of the pulse, the ionosonde can compute a virtual height, or the altitude where the pulse was reflected and the pulse frequency equals the plasma frequency, which then determines the electron density at that altitude. The frequency is then increased and the process repeated to obtain the electron density at many points in altitude. This technique has some limitations. First, it is only effective as long as the electron density increases as altitude increases. Thus once the frequency of the pulse reaches the critical frequency of the densest part of the ionosphere, any waves of higher frequency penetrate the ionosphere entirely without any reflection from higher layers. A similar technique can be used by satellite-based topside sounders such as Alouette 1 and 2 (*Bilitza et al.*, 1998) to obtain electron densities above the altitude of maximum density. Ionosondes, however, are limited in diagnosing the *D*-region ionosphere because the critical frequency at *D*-region altitudes is in the VLF band, which is out of reach for ionosondes whose transmitters typically bottom out near 1 MHz. However, they are sometimes able to measure *E*-region densities when they are high enough.

A riometer is a passive instrument that can provide some coarse information on *D*- and *E*- region densities below  $\sim 100$  km. A riometer receives cosmic radio noise at frequencies near 30 MHz. If the ionosphere remains undisturbed and at an ambient density, then the signal received by the riometer varies over a sidereal day as different parts of the sky are observed. When particles begin precipitating on the ionosphere in auroral regions, the density of the lower ionosphere increases, which increases absorption of the cosmic radio noise resulting in a smaller signal at the riometer. Subtracting an average “quiet” detector value from the actual detector output yields the riometer absorption, which increases with increasing density in the lower ionosphere (*Little and Leinbach*, 1958).

Incoherent scatter radars constitute one more method for measuring densities in the lower ionosphere. These radars must be very powerful to obtain measurable signals from a tenuous lower ionosphere, but the power returned from the radar can be used to obtain electron and ion densities and temperatures above  $\sim 50$ – $70$  km.

*Friedrich and Rapp* (2009) includes a survey of measurements of the lower ionosphere using these instruments.

### 1.2.2 Ionospheric Models

This vast array of ionospheric diagnostic instruments owes its existence to the extreme variability of the ionosphere, particularly in the auroral *D*- and *E*-regions. However, it is still convenient to have a set of standard reference ionospheric profiles available for modeling purposes. These reference profiles are assembled from decades of observations using a combination of ionospheric instruments as well as theoretical work. The International Reference Ionosphere (IRI) provides electron and ion densities as a function of altitude under a variety of conditions. IRI emphasizes the ionosphere above the *E*-region and other models such as the Ionospheric Model for the Auroral Zone (IMAZ) (*McKinnell and Friedrich, 2007*) are developed specifically to model the *D*-region. IRI's counterpart for neutral molecules and temperatures is the Mass Spectrometer and Incoherent Scatter (MSIS) model (*Hedin, 1991*). Lastly, since the ionosphere is permeated by the Earth's magnetic field, the International Geomagnetic Reference Field (IGRF) (*International Association of Geomagnetism and Aeronomy et al., 2010*) provides the data on the strength and direction of the Earth's intrinsic magnetic field as a function of space and time. All of these models are used as inputs in the rest of this work whenever they are needed in numerical computations.

## 1.3 Ionospheric Currents

Since a plasma consists of mobile charge carriers, it can also support a current in the presence of an electric field. Large scale currents do in fact flow through the ionosphere as a result of several processes. The two major current systems are the auroral electrojet and the equatorial electrojet. The equatorial electrojet is part of the solar quiet (Sq) system driven purely by thermal convection, though it is enhanced in a narrow region near the equator by the convergence of the Sq currents from the northern and southern hemispheres, as well as the interaction of these

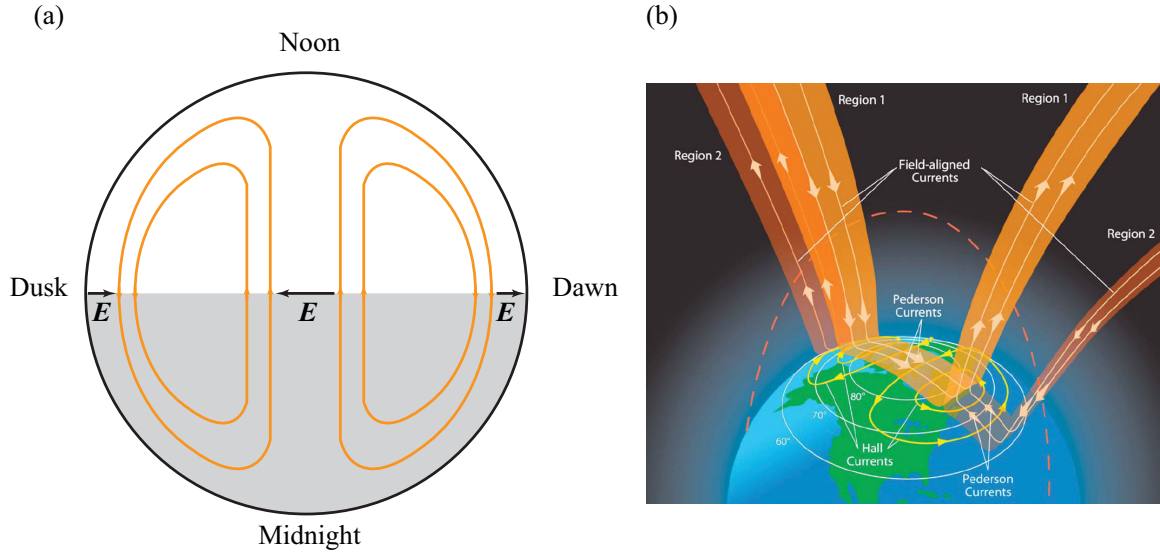


Figure 1.3: (a) A cartoon showing a simplified two-cell convection system with the Hall electrojet currents (orange) driven by dusk-to-dawn electric fields at lower latitudes and a dawn-to-dusk electric field across the polar cap. (b) A cartoon illustrating how the auroral electrojet (the Hall and Pedersen currents) connects with the system of magnetospheric currents (Region 1 and Region 2 currents) (*Le et al.*, 2010).

currents with the Earth's magnetic field, which is nearly horizontal at the equator (*Baumjohann and Treumann*, 1997, pg. 69)

The auroral electrojet system shown in Figure 1.3 is a continuation of convection that occurs in the Earth's magnetosphere that is ultimately driven by the solar wind. Under certain conditions, the solar wind, and the sun's interplanetary magnetic field (IMF) forces the Earth's magnetic flux tubes away from the dayside, over the poles, to the nightside. As these magnetic field lines accumulate on the nightside, they eventually release their energy and flow back towards the Earth on the nightside. This motion of the magnetic field lines antisunward over the pole, and sunward on lines that intersect with Earth at lower latitudes manifests as a convection electric field in the Earth's frame of reference. This electric field, depicted by the black arrows in Figure 1.3a, is from dawn to dusk across the pole, and dusk to dawn at lower latitudes. At the same time, particles that are injected down the magnetic field lines from the release of energy in the nightside precipitate onto the ionosphere and



increase its conductivity in a region known as the auroral oval. The combination of the enhanced conductivity and a dusk to dawn electric field in the oval drives the auroral electrojet current. Since a magnetized plasma is anisotropic, currents do not always follow the electric field direction. In fact, the current (shown in orange) mostly flows in a east-west direction perpendicular to both the electric field (pointing over the pole, or in the north-south direction), and the magnetic field (nearly vertical at high latitudes). This is a simplified view that ignores the corotation electric field, induced by the Earth's rotation dragging plasma around it, and the substorm electrojet, which is strongly enhanced during geomagnetic disturbances. *Baumjohann and Treumann* (1997, Ch. 5) contains a more thorough description of the electrojet currents.

The horizontal ionospheric currents in the auroral electrojet can be measured by the magnetic field they create. Ground-based magnetometers typically measure the magnetic north-south ( $H$ ), east-west ( $D$ ) and vertical ( $Z$ ) components of Earth's geomagnetic field. *Kamide et al.* (1982) and others have shown that the  $H$  deviation ( $\Delta H$ , the  $H$  component minus its quiet time value in the absence of overhead currents) is proportional to the east-west electrojet current density. Ionospheric radars can also infer the electric field driving the auroral currents by measuring the drift velocity of the electrons as they move through the ionosphere (e.g. *Chisham et al.*, 2007).

## 1.4 Modulated Heating

Modulated heating utilizes the natural electrojet currents flowing through the ionosphere as a current source for radiating ELF/VLF waves, thus sidestepping the need to construct a long wire antenna to achieve the same purpose. Because large areas of the ionosphere (on the order of tens of kilometers) can be made to act as an antenna and because the source is located within the ionosphere and elevated over 60 km above the ground, this technique also avoids the problems of an electrically short horizontal antenna that induces ground currents. To make the electrojet currents oscillate in magnitude, high power radio transmitters on the ground operating at a few MHz are used to alter the conductivity of the ionosphere. When a transmitter is turned on, the ionospheric plasma begins to absorb the HF energy and increase

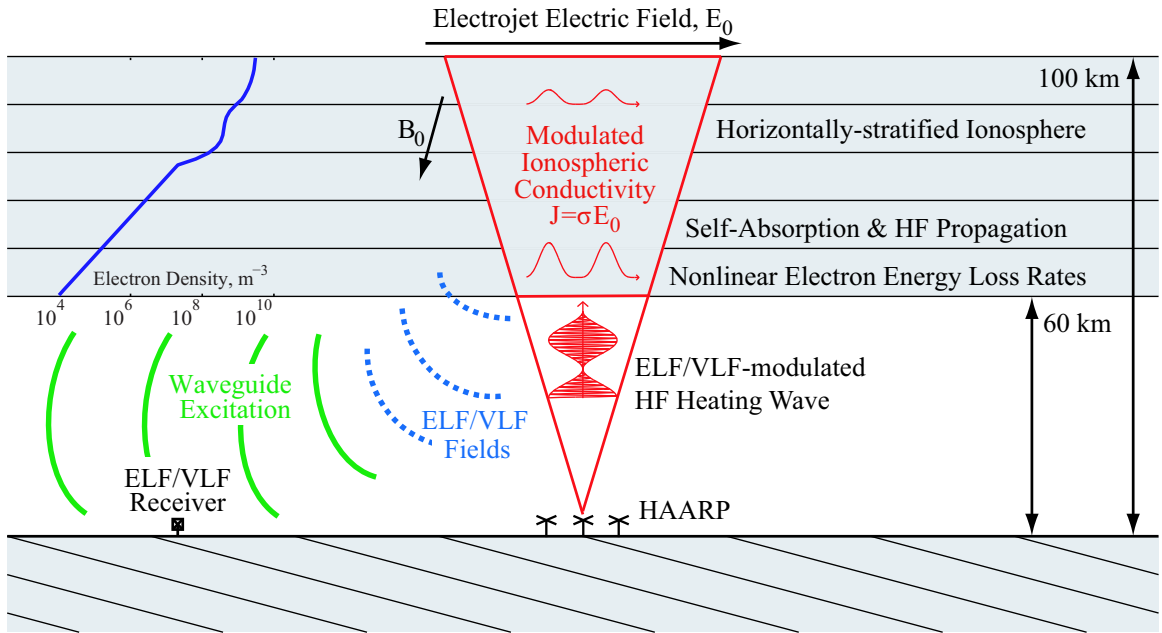


Figure 1.4: Cartoon depicting ELF/VLF waves generated via modulated ionospheric heating. A HF heating wave is amplitude modulated at an ELF/VLF frequency leading to modulation of the ionospheric conductivity and current (red). The radiated ELF/VLF fields (dashed blue) propagate in the Earth-ionosphere waveguide where they are detected on the ground by the receiver. The electron density in the ionosphere is also shown in the upper left. Adapted from *Moore* (2007) pg. 14.

in temperature. The heating typically reduces the conductivity of the plasma as the more energetic electrons in the plasma collide more frequently with neutral molecules, impeding their motion. When the transmitter is turned off, the plasma cools to its ambient temperature and its conductivity returns to its ambient value. Thus, by varying the transmitter power at an ELF/VLF frequency, the ionospheric plasma conductivity ( $\sigma$ ) also varies at the same frequency as shown in red in Figure 1.4. Because the relationship between the transmitter power, and the plasma conductivity is highly nonlinear, the variations in the plasma conductivity also include harmonics or frequency components at integer multiples of the modulation frequency. The ionospheric currents flowing through the plasma vary along with the conductivity and act as the desired ELF/VLF radiator. The technique described above is known as modulated ionospheric heating, and research utilizing this technique has taken place at ionospheric heating facilities since the 1970's. We now briefly review some of this research.

#### 1.4.1 Early Experiments

The first observations of ELF/VLF waves generated by modulated ionospheric heating were made by *Getmantsev et al.* (1974) at Gorky (now Nizhny Novgorod), Russia. Using a 150 kW transmitter at 5.75 MHz, modulated between  $\sim 1 - 7$  kHz, they were able to generate waves that were clearly detected with a receiver located 180 km away. This heater is located at mid-latitudes and thus can only modulate weak thermally driven Sq currents. *Kapustin et al.* (1977) performed this experiment again at a facility located near Monchegorsk, Russia at a more polar latitude and first noted a correlation between (uncalibrated) received ELF amplitudes and magnetometer measurements of the auroral electrojet current. *Belyaev et al.* (1987) summarizes much of these early Russian experiments.

#### 1.4.2 Tromsø, Norway

Construction of a 1.2 MW ionospheric heater at Ramfjordmoen near Tromsø, Norway was completed by 1980 (*Stubbe, 1996*). The higher power available at this facility and

its excellent high latitude location under the auroral electrojet made it well suited for ELF/VLF generation experiments, which were undertaken even before the facility was completed (*Stubbe et al.*, 1981). The facility was upgraded in 1990 with a larger antenna array and is now operated by the European Incoherent Scatter (EISCAT) association.

Experiments at this facility explored in much greater detail the relationship between natural ionospheric conditions and ELF/VLF generation. *Rietveld et al.* (1983) found positive, linear correlations between magnetometer deviations of less than 100 nT and received ELF signal strength in a seven hour experiment. A 32 hour experiment with more detailed analysis followed in *Rietveld et al.* (1987). During the experiment, large magnetic disturbances with H deviations of 300 nT were observed. The authors show ten three-hour scatter plots of ELF amplitude versus  $\Delta H$ . The strongest correlation coefficient was 0.93 and occurred when the electrojet was roughly uniform and centered over the heater. However, half of the three-hour periods have correlations less than 0.34 with the lowest being  $-0.47$ . Magnetic activity was strong, with  $\Delta H > 100$  nT throughout the experiment. The best correlation occurred between 0300–1200 UT corresponding to nighttime through late morning. *Oikarinen et al.* (1997) also found a highly variable relationship between magnetometer measurements and ELF amplitude.

Besides a magnetometer, the Tromsø facility also includes a riometer as well as the Scandinavian Twin Auroral Radar Experiment (STARE) incoherent scatter radar. Measurements from these instruments can be used to estimate the ionospheric electric field and electron density. *Rietveld et al.* (1987) found the correlation between ELF amplitude and the electric field measured by STARE to be always positive with correlation coefficients ranging from 0.17 to 0.89. Correlation coefficients for  $\Delta H$  were mixed ranging from  $-0.23$  to 0.93, and correlation with riometer absorption was worse. However, the riometer-ELF correlation coefficients with the highest magnitude were always negative. *Rietveld et al.* (1987) mentions that this negative correlation may be the result of lower electric fields that accompany periods of high absorption.

Along with the wealth of new experimental observations at the Tromsø facility came new efforts at modeling the HF heating process. For example, *Barr and Stubbe*

(1984) found that different ionospheric electron density profiles had very subtle effects on both generation of the current moment and propagation in the Earth-ionosphere waveguide. While higher densities resulted in less excitation of the ionosphere, this effect was compensated for by decreasing source altitudes and better waveguide excitation suggesting little overall effect of electron density on measured ELF amplitude.

Experiments at Tromsø also began analyzing the harmonic content of the generated ELF waves. The harmonics generated in modulated heating are influenced by several variables. One of the most important is the waveform used to modulate the HF power as the harmonic content of the waveform is a component of the harmonic content of the radiated ELF waves. Square wave modulation, where the HF beam is turned on and off at an ELF frequency is a simple modulation waveform that intrinsically has strong odd harmonics but no even harmonics. *James* (1985) presented observations and simulations of harmonic content and square-wave amplitude modulation at 525 Hz. In modeling with daytime electron density and temperature profiles, they noted a change in the conductivity spectrum due to the fact that heating and cooling time constants increased with altitude. Below 65 km, the conductivity closely approximated a square wave with very weak even harmonics ( $>30$  dB below the fundamental). Between 65–85 km, the heating and cooling time constants are comparable to the ELF period ( $\sim 1$  ms), hence the evolution of the conductivity with time became a double-exponential with stronger even harmonics ( $\sim 15$  dB below the fundamental). Above 85 km, the recovery time is substantially longer than the ELF period so that the conductivity function is a triangular wave with weaker even harmonics again. The third harmonic decreased from 10 dB below the fundamental at 60 km to nearly 20 dB below at 100 km. Nighttime results were similar except the transition to a more triangular wave occurs at 95 km. These simulations failed to reproduce experimental results shown in *James et al.* (1984) where ground receivers 17 km from the heater detected a third harmonic nearly the same amplitude as the fundamental and a fifth harmonic only 4 dB below the fundamental. Even harmonics were approximately 10 dB below the fundamental. Measurements on the International Satellites for Ionospheric Studies (ISIS 1) satellite corresponded more closely

to the simulations and the authors suggested that waveguide effects were partly responsible for the discrepancies in ground observations. *Barr et al.* (1993) attempts to correct for waveguide effects by normalizing the received amplitude of each harmonic with the received amplitude of a wave with a fundamental frequency that was the same as the harmonic. After normalizing, the harmonic content was similar to that of a square wave though there are still even harmonics 29 dB below the fundamental.

A second important factor influencing the spectrum of the radiated signal is the nonlinearity of the HF heating process, such that scaling the HF power does not scale the generated signal. For this reason, sinusoidal modulation, with no inherent harmonic content, still results in substantial received harmonics. For example, *Oikarinen et al.* (1997) showed significant harmonic content of a 1375 Hz signal generated with sinusoidal modulation.

### 1.4.3 Other heating facilities

Though the Tromsø and the early Russian experiments are discussed in detail because the body of previous work at these facilities relates directly to the work presented here, it is also worth noting some of the modulated heating experiments at other locations. Although most ELF generation experiments occur at higher latitudes near the auroral electrojet, there have also been experiments at lower latitudes. *Ferraro et al.* (1982) first reported ELF waves with amplitudes near 1 fT directly below the heated region generated using a heater at Arecibo, Puerto Rico. Later experiments by *Ferraro et al.* (1984) and *Lunnen et al.* (1985) reported received amplitudes in the tens of fT, still over two orders of magnitude below the amplitudes generated at Tromsø despite the fact that the two heaters have similar power. The lack of an electrojet over Arecibo renders ELF generation much weaker, though not impossible.

*Lunnen et al.* (1984) first observed ELF waves from modulated heating under the equatorial electrojet using a Very High Frequency (VHF) radar at Jicamarca, Peru. The ELF amplitudes reported in *Lunnen et al.* (1985) are still only  $\sim 1$  fT. These amplitudes are still impressive considering the Jicamarca radar operates with a much higher frequency and narrower beamwidth compared to other ionospheric heaters

and neither characteristic is conducive for *D*-region ionospheric heating (*Cohen et al.*, 2012).

The High Power Auroral Stimulation (HIPAS) facility was the next high latitude heater to be constructed and is located outside Fairbanks, Alaska. *Ferraro et al.* (1989) made the first observations of ELF signals generated at this facility. Experiments at this facility showed similar results to ones at Tromsø, but advancements include detection of signals as far away as Connecticut. *Barr* (1998) includes a thorough review of modulated heating experiments prior to the construction of the newest facility, HAARP.

#### 1.4.4 HAARP

The newest and most powerful ionospheric heater is part of the High Frequency Active Auroral Research Program (HAARP) facility, located in Gakona, Alaska. The preliminary version of the transmitter was completed in 2003 with 960 kW of power before it reached its present state in 2007 with a 15x12 array of antennas capable of generating 3.6 MW of RF power. The first observations of ELF waves from modulated heating at HAARP were presented by *Milikh et al.* (1999) (as with Tromsø, before even the preliminary facility was completed). The high power of the transmitter allows for reliable detection of ELF/VLF waves near the transmitter even during poor generation conditions. However, the large number of antenna elements also allows for more creative experiments. For example, the beam can be steered electronically by varying the phase at each antenna. Thus, the beam can be left at full power continuously and swept back and forth at an ELF frequency instead of being amplitude modulated at a ELF frequency. This technique, known as geometric modulation, can result in ELF waves with amplitudes  $\sim 10$ dB better than amplitude modulation *Cohen et al.* (2010a).

Other scientific advances realized with modulated heating experiments at HAARP include further analysis of the harmonic content generated due to nonlinear distortion. *Moore et al.* (2006) conducted experiments at HAARP using a sinusoidally modulated 3.25 MHz beam and examined the amplitudes of the fundamental, second, and third

harmonics as a function of ELF frequency as well as HF power (up to 771 kW). The second harmonic was typically  $\sim 8$  dB below the fundamental with the third harmonic  $>15$  dB below, depending on the HF power. Numerical models also agreed with those experimental results.

HAARP has also been used to study injection of waves into the magnetosphere much as the Siple transmitter was used in *Helliwell and Katsufurakis* (1974). *Gołkowski et al.* (2008) observed ELF signals that were generated by HAARP and propagated along magnetospheric “ducts” to the magnetic conjugate point in the southern Pacific Ocean, as well as signals that then returned along the same path back to HAARP. The ELF waves can also be detected by satellite instruments such as the Detection of Electro-Magnetic Emissions Transmitted from Earthquake Regions (DEMETER) ELF/VLF receiver. *Piddyachiy et al.* (2008) showed that the ELF waves generated by HAARP were concentrated in a narrow column above the transmitter with weaker signals detected in more distant regions.

## 1.5 Contributions and Approach

Modulated heating experiments at HAARP have led to many scientific results that have improved our understanding of how waves interact with plasmas both in the ionosphere and the magnetosphere. In contrast, the focus of this thesis is on the practical aspects of using modulated heating purely as an ELF/VLF source. Compared with a traditional horizontal wire transmitter such as Siple station or the Navy ELF transmitter, modulated heating has several important differences. The first is a dependence on a highly variable auroral electrojet. Understanding how natural conditions, including the strength of the electrojet, affects ELF/VLF generation is important in assessing the reliability of modulated heating as an ELF source. After an overview of HF heating physics and modeling in Chapter 2, we examine ELF experimental data collected from over two years of experiments in Chapter 3. By correlating measured ELF amplitudes with measurements from other ionospheric diagnostics, we investigate how changes in the ionosphere relate to changes in ELF generation, eventually leading to a statistical model that can be used to estimate the



ELF generation given data from other ionospheric diagnostics. In Chapter 4, we turn to numerical modeling to explore the physical mechanisms for why changes in the ionosphere affect ELF generation in the way it does.

A second important difference between modulated heating and traditional ELF antennas is the nonlinear distortion between the transmitted waveform and the ionospheric current variation. This distortion can create strong harmonics at integer multiples of the modulation frequency. In Chapter 5, we design waveforms in an attempt to minimize harmonics in the generated ELF signal and compare these waveforms to more traditional ones. The choice of waveform affects not only the harmonic content of the ELF signal but also its power and its generation efficiency.

Finally, in Chapter 6, we apply lessons from the earlier chapters to examine how natural variations in ELF generation and choice of modulation waveforms affects transmission of digital data using ELF waves generated via modulated heating. Although the theme of this work centers on practical issues of modulated heating, we do not ignore scientific results we discover along the way. Throughout Chapters 4 and 5, we use theoretical models to explain why particular ionospheric conditions or modulation waveforms affect the characteristics of ELF waves as we observe them in experiments.

The formal contributions of this work are:

- Quantified the relationship between the amplitude of ELF waves generated via modulated ionospheric heating and the strength of the electrojet current demonstrating strong changes in this relationship with geophysical conditions.
- Showed that changes in the proportionality constant between ELF wave amplitude and electrojet current are driven by changes in the ionospheric electron density profile, which independently affect the electrojet current and ELF generation.
- Characterized the sensitivity to ionospheric parameters of a pre-distortion technique for harmonic minimization in modulated heating experiments and compared the harmonic distortion, total power, and efficiency of this technique to standard modulation waveforms.

- Designed an experiment for digital data transmission via modulated ionospheric heating and characterized the resulting bit error rate as a function of signal to noise ratio and harmonic content.

# Chapter 2

## HF Heating: Theory and Modeling

### 2.1 Plasma Fundamentals

Despite being the state of matter most common in the universe, plasmas are less familiar to those on the Earth's surface than are the solids, liquids, and gases we usually associate with everyday matter. A plasma is essentially a gas, but one in which some of the molecules have had their electrons stripped. At equilibrium, there must be overall charge neutrality in a plasma, as large coulomb forces would otherwise exist and not allow equilibrium. If there were an excess amount of positive charge in one area for example, negative charges would be attracted around the positive charge maintaining overall charge neutrality in that area. The length scale on which this shielding occurs is known as the Debye length. Since we would like to deal with plasma as a macroscopic material and focus on the collective behavior of the particles that make up the plasma, the dimensions of the material should be much larger than a Debye length, and there should be a very large number of particles within a sphere with a radius of a Debye length.

A plasma has fluid properties, such as temperature, pressure, velocity, and diffusion coefficients, as well as electromagnetic properties, such as conductivity and permittivity, and changes in each property can affect the others. To understand modulated heating of a plasma, we examine how an electromagnetic wave can affect a physical property of the plasma (the temperature) and how that physical change

translates back into an electrical change (conductivity) before going into more details on how the entire system can be modeled.

## 2.2 HF Heating of Electrons

A plasma is a collection of particles, each moving at a different velocity. Fortunately, tracking the velocity of each of these individual particles is unnecessary in this case, when we can use the concept of a distribution function,  $f(v)$ , to model the statistics of how many particles are moving at a particular velocity. In this work, all plasmas can be modeled using the Maxwell-Boltzmann distribution:

$$f(v) = N \left( \frac{m}{2\pi k_B T} \right)^{3/2} e^{-\frac{mv^2}{2k_B T}} \quad (2.1)$$

$v$  is the particle velocity,  $N$  is number of particles,  $m$  is the mass of a particle,  $k_B$  is Boltzmann's constant, and  $T$  is the temperature. To find the number of particles in a velocity range, we must integrate the distribution function over that range. With  $f(v)$ , we are able to describe the velocity of a collection of particles, using a distribution function parameterized by only one variable: temperature. For our purposes, electrons are the species of particles we are interested in since the HF heating waves primarily affects electrons as opposed to the much more massive ions and neutral molecules. Tracking the changes in the electron temperature allows us to know everything we need about the behavior of the plasma as it undergoes HF heating.

The average kinetic energy of an electron under a Maxwellian distribution is  $\frac{3}{2}k_B T_e$  (*Bittencourt*, 2004, pg. 178), where the  $e$  subscript represents electrons. Thus the change in the average kinetic energy of a collection of electrons in time is represented by  $\frac{3}{2}N_e k_B \frac{dT_e}{dt}$ . This change in electron energy must be caused by a net absorption of power which, in the case of modulated ionospheric heating comes from the incident HF beam. The HF wave accelerates the electrons in the plasma. Without collisions there is no net increase in the electron energy because the HF wave field reverses itself every half period. However, the plasma in the  $D$ -region ionosphere consists of

many more large neutral molecules than electrons, so there is a large probability for an electron accelerated by the electromagnetic wave to collide with a large neutral molecule. These collisions provide a mechanism to damp the HF wave and transfer energy from the wave to the electrons, thus increasing the electron temperature. The power absorbed by the HF wave is given by  $2k\chi S$ , where  $k$  is the HF wavenumber,  $\chi$  is the imaginary component of the refractive index of the plasma (to be discussed more later), and  $S$  is the power density of the HF wave.

While the electron temperature increases due to absorption of the HF wave, the temperature of the neutral molecules is largely unaffected. Thus the high temperature electrons tend to transfer energy to the lower temperature neutrals during collisions, leading to energy loss in the electrons. The loss rate is a sum of the losses from elastic collisions with molecular nitrogen and oxygen (*Banks*, 1966), as well as rotational excitation (*Mentzoni and Row*, 1963; *Dalgarno et al.*, 1968) and vibrational excitation (*Stubbe and Varnum*, 1972), as compiled in *Rodriguez* (1994).

Balancing the rates of energy gained due to absorption of the HF wave ( $2k\chi S$ ) and the energy lost due to collisions ( $L_e$ ) with the change in the electron energy results in the energy balance equation

$$\frac{3}{2}N_e k_B \frac{dT_e}{dt} = 2k\chi S - L_e \quad (2.2)$$

A numerical solution to this equation given the HF power density for a uniform volume of plasma reveals the variation of the electron temperature as a function of time.

## 2.3 Plasma Conductivity

With an understanding of how the electron temperature evolves under HF heating, we can now study the dependence of the conductivity of the ionospheric plasma on electron temperature. The Earth's geomagnetic field makes the ionosphere a magnetized plasma, which is anisotropic, meaning that currents do not necessarily flow in the same direction as the electric field, and the conductivity of the plasma must be

expressed as a tensor. First, let us consider a plasma without a magnetic field, and only a static electric field. This electric field accelerates ions in the direction of the field and electrons in the opposite direction. This acceleration results in a net current in the same direction as the electric field. The acceleration of the charged particles is impeded by collisions with neutral molecules. Thus, the higher the collision rate, the smaller the conductivity.

Now let us add a static magnetic field. The force acting on a charged particle under the influence of electric and magnetic fields is given by the Lorentz force equation

$$\mathbf{F} = q(\mathbf{E} + \mathbf{v} \times \mathbf{B}) \quad (2.3)$$

where  $\mathbf{F}$  is the force on the particle,  $q$  is the fundamental charge,  $\mathbf{E}$  is the electric field,  $\mathbf{v}$  is the particle's velocity, and  $\mathbf{B}$  is the magnetic field. Note that any component of the electric field parallel to the magnetic field only causes motion parallel to the magnetic field. The magnetic field has no effect on particles travelling parallel to it ( $\mathbf{v}_{\parallel} \times \mathbf{B} = 0$ , where  $\mathbf{v}_{\parallel}$  is the component of the velocity parallel to  $\mathbf{B}$ ). The particles moving parallel to the magnetic field can be treated as if the magnetic field was not present. The motion caused by the component of the electric field perpendicular to the magnetic field can be treated separately.

If there were no electric field, electrons and ions would move in a circular orbit about a magnetic field line with an angular frequency called the cyclotron frequency

$$\omega_c = \frac{|q|B}{m} \quad (2.4)$$

where  $m$  is the mass of the particle and a corresponding cyclotron radius given by

$$r_c = \frac{mv_{\perp}}{|q|B} \quad (2.5)$$

Adding a electric field perpendicular to  $\mathbf{B}$  accelerates the particle for half its circular trajectory and decelerates it for the other half. This effect increases the cyclotron radius where the particle is moving faster, causing drift perpendicular to both  $\mathbf{E}$  and  $\mathbf{B}$ . Figure 2.1 illustrates the trajectories for electrons and ions undergoing  $\mathbf{E}$  cross

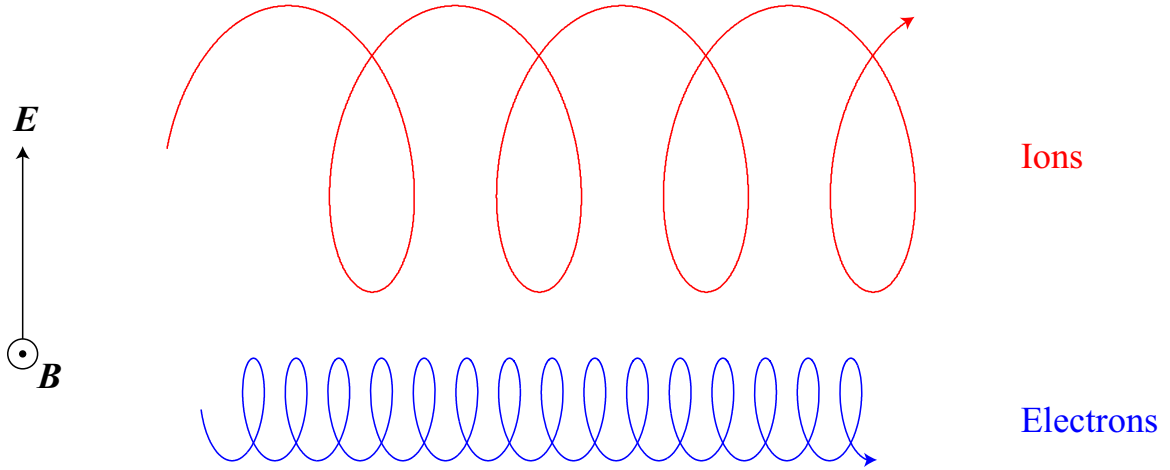


Figure 2.1: Cartoon depicting how electrons and ions undergo  $\mathbf{E} \times \mathbf{B}$  drift. The upward pointing electric field accelerates ions upwards and electrons downward while the magnetic field pointing out of the page, forces both ions and electrons to gyrate. The velocity and thus gyroradius are larger at the top of the figure for ions and at the bottom for electrons because of the acceleration from the electric field. Both electrons and ions drift to the right. Note the larger gyroradius of the ions due to the larger ion mass.

$\mathbf{E} \times \mathbf{B}$  drift with an electric field pointing upwards and a magnetic field pointing out of the page. Both electrons and ions move in the plane of the page while drifting to the right.

Electrons and ions under the influence of electric and magnetic fields thus undergo  $\mathbf{E} \times \mathbf{B}$  drift, where in the absence of collisions, they move with a velocity given by

$$\mathbf{v} = \frac{\mathbf{E} \times \mathbf{B}}{B^2} \quad (2.6)$$

Both electrons and ions drift with the same velocity and direction so this drift does not result in a net current. However, if neutral molecules are present, collisions affect the much larger ions more so than the electrons. An ion such as  $\text{O}_2^+$  has a mass roughly 60,000 times greater than the electron mass and a corresponding cyclotron frequency 60,000 smaller. The ion cyclotron frequency, which is on the order of 100 Hz is much smaller than the neutral collision frequency in the  $D$ -region ionosphere on the order

of a Megahertz and thus ions can not effectively gyrate around a magnetic field line and undergo  $\mathbf{E} \times \mathbf{B}$  drift before a collision occurs. The electron cyclotron frequency is roughly the same order of magnitude as the collision frequency and electrons are able to undergo some  $\mathbf{E} \times \mathbf{B}$  drift. This discrepancy between the ion and electron mobility leads to a Hall current carried by electrons in the  $-\mathbf{E} \times \mathbf{B}$  direction. Note that at higher altitudes in the  $F$ -region where collisions are rare, the electron and ion currents are in balance and no Hall current flows.

Collisions between charged particles and neutrals also leads to the Pedersen currents flowing in the same direction as  $\mathbf{E}$  but still perpendicular to  $\mathbf{B}$ .

To formalize the parallel, Hall, and Pedersen currents, we define a coordinate system so that the  $z$ -axis points in the direction of the magnetic field. We can then write Ohm's law as

$$\mathbf{J} = \begin{bmatrix} \sigma_P & -\sigma_H & 0 \\ \sigma_H & \sigma_P & 0 \\ 0 & 0 & \sigma_{\parallel} \end{bmatrix} \mathbf{E} \quad (2.7)$$

where  $\sigma_H$ ,  $\sigma_P$ , and  $\sigma_{\parallel}$  are the Hall, Pedersen, and parallel conductivities. Expressions for these conductivities are derived from *Tomko* (1981, pg. 137) and can be written as

$$\sigma_H = \frac{4\pi q^2}{3m_e} \int \frac{\omega_{ce} v_e^3}{\nu_{av}^2 + \omega_{ce}^2} \frac{\partial f_e}{\partial v_e} dv_e \quad (2.8)$$

$$\sigma_P = \frac{4\pi q^2}{3m_e} \int \frac{\nu_{av} v_e^3}{\nu_{av}^2 + \omega_{ce}^2} \frac{\partial f_e}{\partial v_e} dv_e \quad (2.9)$$

$$\sigma_{\parallel} = \frac{4\pi q^2}{3m_e} \int \frac{\nu_{av} v_e^3}{\nu_{av}^2} \frac{\partial f_e}{\partial v_e} dv_e \quad (2.10)$$

Here,  $v_e$  is the electron velocity, and  $f_e$  is the electron velocity distribution function, which is the Maxwellian distribution in Equation 2.1.  $\nu_{av}$  represents the average modified collision frequency (the sum of  $\nu_{\text{eff}}^{\text{N}_2}$  and  $\nu_{\text{eff}}^{\text{O}_2}$ ),

$$\nu_{\text{eff}}^{\text{N}_2} = \frac{5}{3} \cdot 2.33 \times 10^{-17} N_{\text{N}_2} (1 - 1.25 \times 10^{-4} T_e) T_e \quad (2.11)$$

$$\nu_{\text{eff}}^{\text{O}_2} = \frac{5}{3} \cdot 1.82 \times 10^{-16} N_{\text{O}_2} (1 + 1.36 \times 10^{-2} \sqrt{T_e}) \sqrt{T_e} \quad (2.12)$$



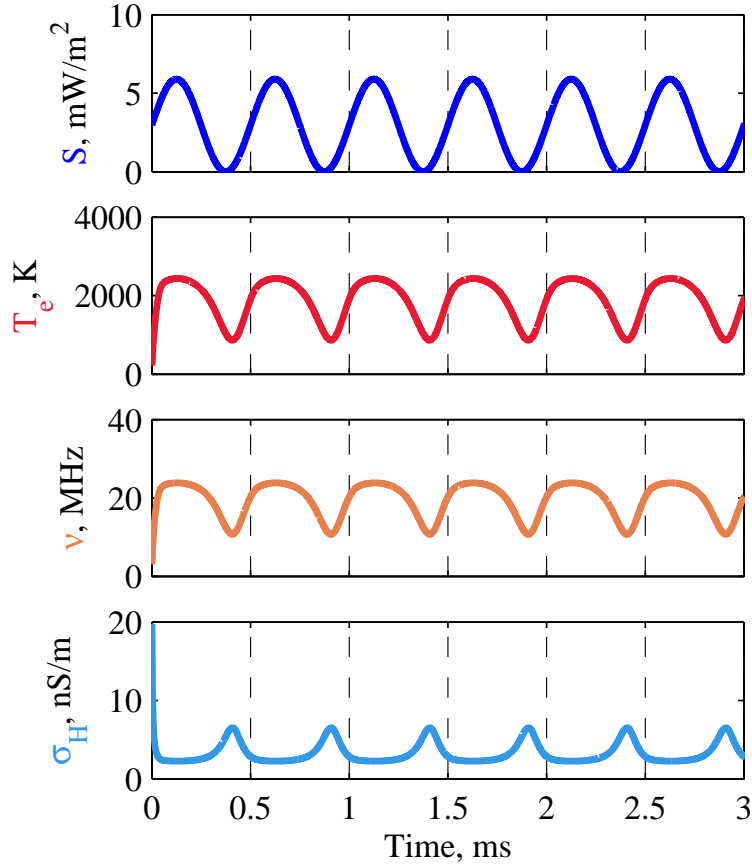


Figure 2.2: Simulation of the temperature, collision rate, and Hall conductivity of ionospheric plasma at 75 km altitude when heated with a 2.75 MHz HF beam sinusoidally modulated at 2 kHz.

from *Banks* (1966) with the 5/3 term derived from *Sen and Wyller* (1960).  $N_{N_2}$  and  $N_{O_2}$  are the concentrations of molecular nitrogen and oxygen.

We now have the tools we need to determine the effect of modulated HF heating on the conductivity of a uniform block of plasma. Figure 2.2 shows the manner in which the electron temperature, collision rate, and Hall and Pedersen conductivities change when a plasma absorbs HF power that is sinusoidally modulated. In this example, a 2.75 MHz HF beam modulated at 2 kHz is used. The electron temperature is determined by solving Equation 2.2 numerically. The collision rate is computed using

Equations 2.11 and 2.12, and the Hall conductivity is determined from Equation 2.8. The plasma parameters are typical for those in the ionosphere at 75 km in altitude:  $N_e = 10^7 \text{ m}^{-3}$ ,  $N_{N_2} = 5.105 \times 10^{20} \text{ m}^{-3}$ ,  $N_{O_2} = 1.364 \times 10^{20} \text{ m}^{-3}$ , and  $T_0 = 216.8 \text{ K}$ . As the HF power increases in the first 100  $\mu\text{s}$ , the temperature rapidly increases from a few hundred Kelvin to a few thousand Kelvin. Although the heating power continues to increase, the temperature saturates because the loss rates increase as the temperature increases until the energy gained by the electrons equals the energy lost. As the heating power decreases, the temperature also decreases, though the cooling occurs relatively slowly and the temperature never returns back to the ambient temperature before increasing again. Higher temperatures lead to higher collision rates and lower values of the Hall conductivity.

## 2.4 HF Propagation

The energy balance equation determines the manner in which a uniform volume of plasma reacts when it absorbs a certain amount of energy. The ionosphere is not a uniform volume of plasma, so that calculating its response to heating by HF waves involves dividing the ionosphere into a grid. Plasma in each element of a grid can be assumed to be uniform if the grid size is small enough. The HF power incident at each grid point is also different. Grid points farther away from the transmitter receive less power density than grid points nearer. In addition, power is absorbed and refracted as it passes through the ionosphere. Computing the incident power at each point requires an understanding of how waves propagate through plasmas.

### 2.4.1 HF Absorption and Refraction

The behavior of a wave as it passes through a material is described by the refractive index,  $n$ . The real part of  $n$  can be used in Snell's Law to account for refraction of the HF wave as it passes through the ionosphere, while the imaginary part accounts for the absorption of the wave power by the plasma. The refractive index of a cold, magnetized plasma is given by the Appleton-Hartree equation (*Budden*, 1985, pg.

74):

$$n^2 = 1 - \frac{X}{1 - jZ - \frac{Y^2 \sin^2(\theta)}{2(1 - X - jZ)} \pm \sqrt{\frac{Y^4 \sin^4(\theta)}{4(1 - X - jZ)^2} + Y^2 \cos^2(\theta)}} \quad (2.13)$$

where

$$X = \frac{\omega_{pe}^2}{\omega^2} \quad (2.14)$$

$$Y = \frac{\omega_{ce}}{\omega} \quad (2.15)$$

$$Z = \frac{\nu_{\text{eff}}}{\omega} \quad (2.16)$$

$\theta$  is the angle between the wave normal and the geomagnetic field. The quantities  $X$ ,  $Y$ , and  $Z$  are convenient because they express the HF wave frequency,  $\omega$  in terms of the electron plasma frequency  $\omega_{pe}$ , the electron cyclotron frequency  $\omega_{ce}$ , and the effective electron-neutral collision frequency  $\nu_{\text{eff}}$ . Thus the magnitude of  $X$ ,  $Y$ , and  $Z$  denotes the importance respectively of debye shielding, the geomagnetic field, and collisions to propagation of the HF wave. For example, if the wave frequency is very high and  $X$ ,  $Y$ , and  $Z$  are very small, then  $n \simeq 1$ , and the wave propagates as if in free space without being affected by the plasma. If  $Y$  and  $Z$  are very small, indicating that the effects of a magnetic field and collisions are negligible, then  $n$  simply decreases as the wave frequency decreases (and  $X$  increases) until  $\omega = \omega_{pe}$  and  $X = 1$  and the wave must reflect as discussed in Section 1.2. Note also that the  $\pm$  in Equation 2.13 indicates the presence of two modes. When the wave propagates parallel to the Earth's geomagnetic field as is approximately the case at high latitudes where the geomagnetic field is nearly vertical, a '+' yields a left hand circularly polarized wave, while a '-' sign yields a right hand circularly polarized wave. In ionospheric heating terminology, these are referred to as O-mode and X-mode polarizations respectively. We focus herein exclusively on X-mode polarization as it results in more effective ELF wave generation (e.g., *Stubbe et al.*, 1982).

The index of refraction from the Appleton-Hartree equation gives all the information needed to track the HF waves propagating through the ionosphere. Refraction of the wave from one grid point to another obeys Snell's Law:

$$\frac{\sin \theta_1}{\sin \theta_2} = \frac{\Re(n_1)}{\Re(n_2)} \quad (2.17)$$

where the wave is propagating from a grid point with refractive index  $n_1$  at an angle  $\theta_1$  with the normal to the boundary between the points, to a grid point with refractive index  $n_2$  at a new angle  $\theta_2$  with respect to the boundary normal. The direction in which energy flows is actually different from the direction of the wave normal and the difference is given by

$$\tan \delta = \frac{1}{n} \frac{\partial n}{\partial \theta} \quad (2.18)$$

where  $\delta$  is the angular difference between the direction of energy flow and the wave normal vector (*Budden*, 1985, pg. 110). The velocity at which this energy travels through the ionosphere is the group velocity (*Budden*, 1985, pg. 130)

$$v_g = \frac{c}{\frac{\partial \omega}{\partial \omega n} \cos \delta} \quad (2.19)$$

Finally, the HF power absorbed at a particular point is given by  $-2k\chi$ , where  $\chi = \Im \mathbf{m}(n)$ , as used in Equation 2.2.

Knowing now the direction in which HF energy propagates, the velocity at which it travels, the amount of energy absorbed, and the relationship between the energy absorbed and the plasma conductivity, all that remains is the implementation into a HF heating code. The lineage of several codes developed in the Stanford VLF group based on the work of *Tomko* (1981) includes *Rodriguez* (1994); *Moore* (2007); *Payne* (2007); *Cohen* (2009). In this work we use the code described in detail in *Cohen* (2009) and our discussion of its implementation is thus only a brief summary.

### 2.4.2 1-D Model

Obtaining the modified ionospheric conductivity tensor over a range of altitudes above the HAARP heater is one basic application of the HF heating code. This application requires tracking the HF power only in a narrow column, with a one dimensional grid of cells in the vertical direction. Each cell is 2 km x 2 km in the horizontal direction and 1 km in the vertical direction. By aligning this grid along the center of the HAARP beam, where most of the transmitted power is concentrated, we can estimate the altitude dependence of the modified conductivities over HAARP.

The power density incident at the lowest cell at 60 km in altitude is known from HAARP's effective radiated power and is used to compute the modified temperature, collision frequency, and conductivity at that altitude. The power absorbed at this altitude is then used to compute the power remaining to heat the next layer where the computation is repeated. The model also accounts for  $1/r^2$  dissipation, where  $r$  is the distance from the transmitter. The final result is the modified conductivity time series as in Figure 2.2 at each cell in altitude.

Figure 2.3 shows the normalized Hall conductivity resulting from a sinusoidal heating envelope at altitudes from 60 to 90 km. The plotted conductivity is normalized so that the curves at each altitude are the same size. The amplitude of the conductivity variation actually changes dramatically as a function of altitude but this figure is intended to highlight the shape of the conductivity variation as a function of altitude. Although sinusoidal heating is used, the modified Hall conductivity is distorted and not sinusoidal, and its characteristics are highly dependent on altitude.

The magnitude of the Hall and Pedersen conductivities at the fundamental frequency are shown in Figure 2.4. The solid lines represent the ambient value of the conductivity while the dashed lines represent the conductivity when the heater power,  $S$  is at a maximum. Note that heating reduces the value of the Hall conductivity at all altitudes as increasing numbers of electron-neutral collisions impair the Hall current. The Pedersen conductivity is also reduced by heating below  $\sim 80$  km but is increased at higher altitudes. At lower altitudes, where there are already many collisions, a further increase in the collision rate impedes the Pedersen current. However, collisions are necessary for the Pedersen current to exist and at higher altitudes where

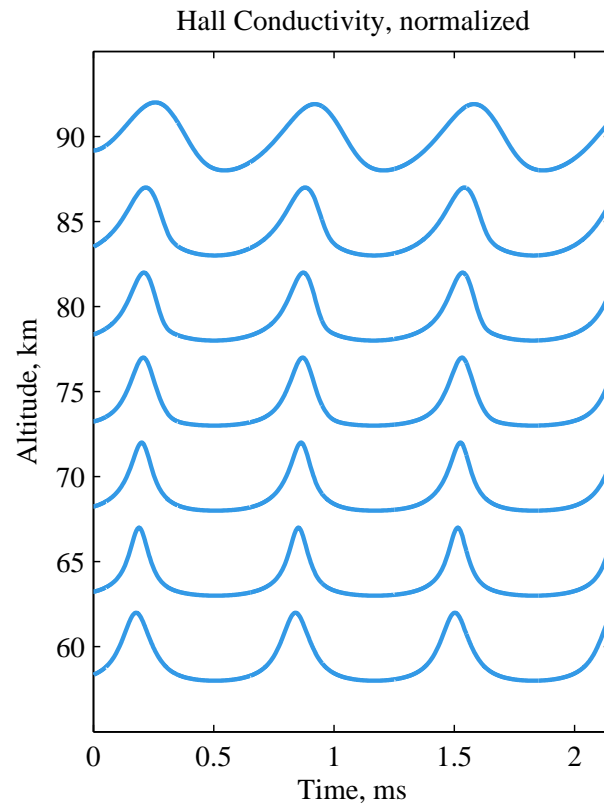


Figure 2.3: Simulated Hall conductivity over time from 60 to 90 km in 5 km increments when using a 2.75 MHz HAARP HF beam sinusoidally modulated at 1510 Hz. Each conductivity curve is normalized to have the same amplitude so that the shape of each curve is more distinct.

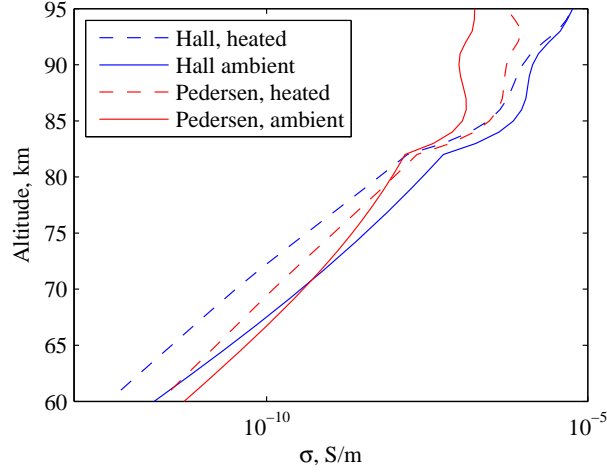


Figure 2.4: Hall and Pedersen conductivity as a function of altitude. Blue lines represent ambient (solid) and heated (dashed) Hall conductivity. Red lines similarly represent Pedersen conductivity. Heating always reduces the Hall conductivity but increases the Pedersen conductivity above  $\sim 80$  km.

collisions become rarer, the increased collision rate induced by heating increases the Pedersen conductivity. During modulated heating, the lower altitude Pedersen currents are out of phase with the higher altitude Pedersen currents and these currents partially cancel out. This cancellation is one reason why the modulated Hall currents contribute more to ELF generation than the Pedersen currents.

While performing the computation, the code also accounts for a phenomenon known as self-absorption. As the HF energy propagates through the plasma, it simultaneously heats it, thus altering the imaginary part of the refractive index and thus the rate of absorption before propagation to the next layer. Since the heating is time dependent, the self-absorption is as well, and the HF heating waveform itself changes accordingly.

### 2.4.3 Extension to 3-D

If the spatial distribution of the modified ionospheric conductivity is needed, then the 1-D model can be extended to three dimensions. The 1-D grid of cells becomes a 3-D

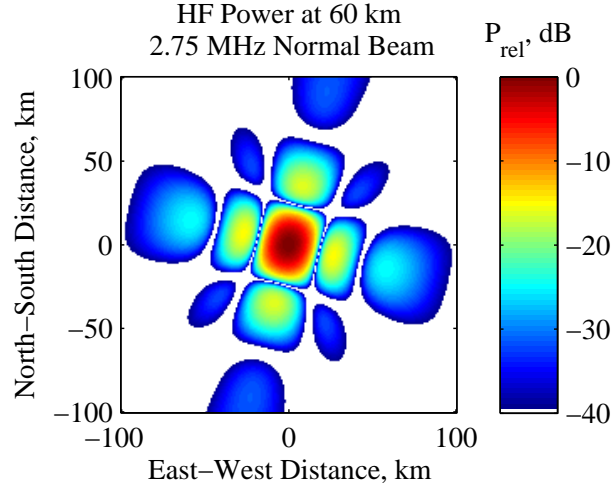


Figure 2.5: HAARP HF beam pattern at 2.75 MHz and 60 km altitude

grid of cells, and the HF power is tracked along several rays emanating from each of the grid cells on the lowest layer instead of only along the center of the beam. As each ray propagates to the next layer of cells in altitude, the ray may not be aligned with the center of any cell. Thus a two-dimensional interpolation is used at each layer to obtain the HF power and direction at the cell centers. New rays then propagate from the cell centers to the next layer.

To obtain the power and direction of the initial rays at the base of the ionosphere at 60 km altitude, some assumption of the characteristics of the HAARP HF beam is needed. In *Payne* (2007), the power in the HF beam was assumed to have a Gaussian profile fitted so the point at which the HF-power has dropped by a half corresponds to the half-power beam width of the main lobe of the transmitter. However, since HAARP transmits using a rectangular phased array of finite extent, the actual beam pattern includes sidelobes, and the *Cohen* (2009) model uses the actual complete beam pattern for the HAARP transmitter. Figure 2.5 depicts the HF power at 60 km altitude relative to the power in the center of the beam.



## 2.5 VLF propagation

The 3-D HF heating model is used to determine the variations of the conductivity of the ionosphere with time over a volume above the HAARP heater. The final modeling step involves the determination of the ELF electromagnetic fields created by the modified ionospheric conductivity structure. First, the ELF source currents are computed from the conductivity variation using Ohm's Law (Eq. 2.7). The conductivity tensor is calculated by the HF heating model. The electric field is assumed to point towards geomagnetic north. Its magnitude is taken as 1 mV/m since the numerical value is not important as all the modeling from this point is linear. For example, an electric field that is 10 mV/m would simply result in electromagnetic fields that are 10 times larger.

Once the currents have been computed, an electromagnetic solver is used to compute the fields at the desired locations in space. The solvers must account for the anisotropic nature of the magnetized ionospheric plasma. Several numerical methods can be used, and many have been implemented in the context of previous PhD dissertation studies within the Stanford VLF group. These include finite difference time domain (FDTD) (*Payne et al.*, 2007), finite difference frequency domain (FDFD) (*Chevalier and Inan*, 2006), and Discontinuous-Galerkin (DG) (*Foust et al.*, 2011) solvers. Each of these methods has advantages and disadvantages, but they are all capable of solving 2-D (with the dimensions usually being altitude and distance from source to receiver), and 3-D problems where ionospheric properties can change along any dimension. However, if the ionosphere is assumed to be horizontally stratified, so that its properties vary only in vertical direction, then the ELF fields can be solved much more quickly and accurately using a full-wave method.

The full wave method solves for the electric and magnetic field components throughout a 3-D space and is ideal for solving problems in this work where the fields are needed in areas no more than a few 100 kilometers wide, and the ionosphere can be reasonably assumed to be uniform over such a horizontal extent. Its computational speed when compared to FDTD, FDFD, and DG methods also makes it more practical for repeated iterations over many different ionospheric profiles, HAARP

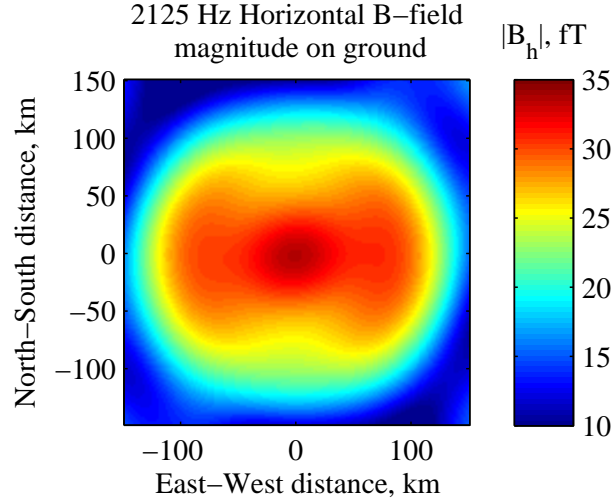


Figure 2.6: Horizontal component of B-field magnitude on the ground from the full wave model. The input currents were taken from the 3-D HF heating model.

transmitter parameters, or other variables. The Stanford Full Wave Model, developed within the VLF group and described in *Lehtinen and Inan* (2008) has been used in many HAARP modeling problems within the group (e.g. *Piddyachiy et al.*, 2008; *Cohen et al.*, 2010b; *Jin et al.*, 2011; *Cohen et al.*, 2012) and is also utilized here.

In the technique of *Lehtinen and Inan* (2008) the ionosphere is divided into horizontal layers in altitude. Each layer has a different permittivity due to the different electron density and collision rate at each altitude. Between each layer an incident wave is partially reflected and partially transmitted, and the electromagnetic boundary conditions between the layers also specify that the horizontal component of the refractive index vector must be conserved. The solution for the fields inside each layer then derives from the solution of the reflection and transmission coefficients at each boundary. Figure 2.6 shows the magnitude of the horizontal component of the ELF wave magnetic field computed by the full wave model using input currents generated from the 3-D heating model. These are the same fields that would be measured using orthogonal loop antennas and an ELF receiver allowing for direct comparisons between the full wave model output and experimental data. The input currents were

computed from the HF heating model using a 2.75 MHz HF beam sinusoidally modulated at 2125 Hz.

Generation of ELF waves via modulated ionospheric heating is theoretically complex due to the factors such as the anisotropy of the ionospheric plasma and the nonlinear relationship between HF power and the ionospheric plasma conductivity. The combination of the HF heating and full wave models incorporates all the complex physics and is used to analyze the manner in which changes in natural conditions, such as the ionospheric density profile, and experimental parameters, such as the HF power envelope affect the properties of ELF waves generated via modulated ionospheric heating.

## Chapter 3

# Relating ELF Generation to Natural Conditions

Having introduced the physics behind modulated ionospheric heating, we now discuss experimental measurements of ELF signals generated by the HAARP ionospheric heater. When browsing years of ELF experiments at HAARP, it is quickly apparent that ELF generation can vary wildly, with resulting amplitudes varying by nearly three orders of magnitude. This variation results from the dependence of modulated heating on the highly variable natural electrojet current. It is natural to assume that ELF amplitude would then be directly correlated to the strength of the electrojet, and some works still lean on arguments that a very weak electrojet necessarily implies that modulated *D*-region heating cannot generate ELF waves (*Kuo et al.*, 2012). However, work by *Rietveld et al.* (1987) and *Oikarinen et al.* (1997) has shown that the correlation between electrojet strength and ELF amplitude is not always positive.

To assess the manner in which ELF generation is impacted by natural conditions, we statistically analyze how ELF amplitude relates to measurements from other ionospheric diagnostics. We start by correlating ELF amplitude with magnetometer measurements of the electrojet more comprehensively than has been done in the past. We then incorporate data from other instruments, and show that measurements of ionospheric electron density can be combined with magnetometer measurements to more accurately predict ELF amplitudes. Much of the work described in this and the

next chapter is published in *Jin et al.* (2009) and *Jin et al.* (2011).

### 3.1 Methodology

An ELF/VLF wave receiver (*Cohen et al.*, 2010c) located in Chistochina, Alaska, roughly 37 km northeast from HAARP records the generated ELF/VLF signals. The receiver consists of two orthogonal triangular (4.2 m height, 8.4 m base) antennas oriented in the magnetic north-south and east-west directions. Prior to August 2007, the antenna consisted of orthogonal square (4.9 m per side) loops with one oriented towards HAARP, and the different antenna sizes are accounted for during calibration. The receiver is capable of measuring magnetic fields of a few femtotesla. The outputs of the two antenna channels pass through an anti-aliasing filter and are each sampled at 100 kHz with 16-bit resolution. To extract the amplitude of individual tones and ramps in post-processing, the digital data passes through an anti-aliasing filter before being down sampled to 12.5 kHz. The segments of data corresponding to times when HAARP transmits a tone or ramp of interest are then mixed down to baseband and digitally filtered with a low-pass finite impulse response (FIR) filter with a 100 Hz bandwidth ( $\sim 12$  dB half-width). In order to mitigate effects of impulsive noise such as lightning generated sferics, the amplitude of each tone is taken to be the median value for the duration of the tone (usually 1 sec). The total ELF/VLF amplitude of the generated tone is then obtained by combining the signals from each antenna in quadrature. A particular transmission format can take as long as a minute to repeat so that the time resolution for amplitude measurements of a given frequency tone within that format can be as coarse as one minute. This is sufficient for observing electrojet changes over several minutes although there do exist changes that take place less than one minute that can not be resolved using this method (*Rietveld et al.*, 1988).

Figure 3.1 shows an example Chistochina recording from 28 Feb 2007 when HAARP was generating 2-sec tones at 2130 Hz. The top two panels show spectrograms from each of the two antenna channels. The bottom panel shows the filtered amplitude of the 2130 Hz tone and the 12 median values, one for each tone in the minute of data. The spectrograms are visually examined to ensure HAARP transmissions are

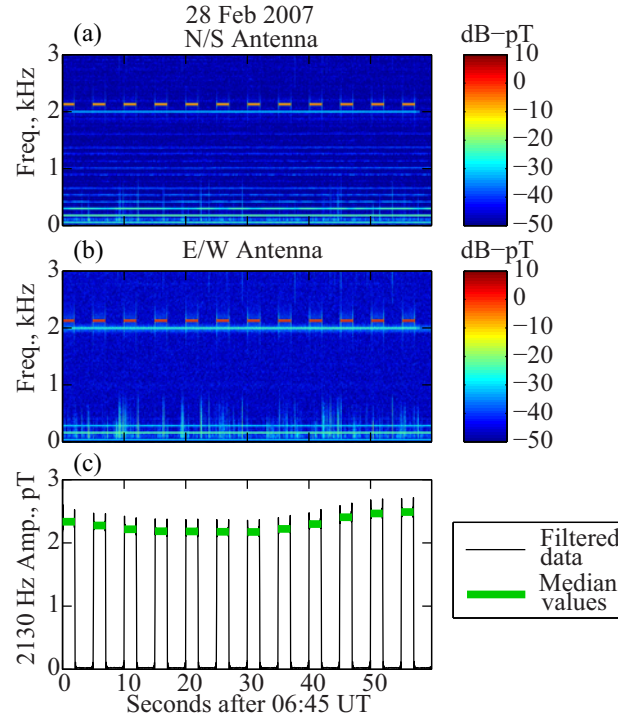


Figure 3.1: (a)-(b) Spectrogram showing ELF signals received at Chistochina, Alaska on 28 February 2007 beginning 0645 UT. (c) Amplitude of the 2130 Hz tone with both channels combined, anti-alias filtered, and downsampled for clarity. The position of the green bars on the time axis corresponds to when the 2130 Hz tone was being transmitted, and the data values used to take the median. The height corresponds to the median value for that tone.

not corrupted by natural or artificial noise.

The HAARP facility also houses many diagnostic instruments, including a fluxgate magnetometer, part of the Geophysical Institute Magnetometer Array (*Wilkinson and Heavner, 2006*), which is used to assess the strength of the overhead currents in the auroral electrojet. The data provide the  $H$ ,  $D$ , and  $Z$  components of the magnetic field sampled every second. The quiet-time magnetic field for a particular day is obtained by taking the mean value of each component on nearby quiet days. We find  $\Delta H$  by subtracting the quiet-time  $H$  value from the  $H$  component in the magnetometer data.

To gather statistics on the relationship between the electrojet strength and generated ELF/VLF amplitude, we searched the database of ELF/VLF generation experiments for formats that contained HAARP transmissions modulated at 2125 or 2130 kHz. Observations at both Tromsø (*Stubbe et al., 1982*) and HAARP (*Papadopoulos et al., 2003*) indicate strongest generation with ELF/VLF frequencies at multiples of 2 kHz due to resonance in the Earth-ionosphere waveguide. For this study, all heating is performed with a 2.75 or 3.25 MHz X-mode, full power, vertical beam, and the ELF tones are amplitude modulated with a 40–50% duty cycle square wave. We focus only on nighttime observations, and thus further limit the database to between one hour after sunset at 100 km altitude to one hour before sunrise at 100 km.

The analysis presented here contains HAARP transmissions and magnetometer recordings from 28 Feb–2 Mar 2007; 13,14,16,17,19, and 31 Jan 2008; 3,5, and 6 Feb 2008, and 1, 3, 9, 10, 11, 15 and 19 Mar, 2008. Each experiment is broken into 18-min segments, with any leftover time discarded. This data selection yields 128 segments containing a total of 2304 minutes of data. For each segment, a linear correlation coefficient ( $r$ ) is calculated between the magnitude of  $\Delta H$  and the total ELF signal amplitude. For segments with significant statistical correlation, we calculate the slope ( $a$ ) of the linear least squares fit assuming  $|\Delta H|$  is a function of the ELF amplitude, an “x on y” regression as in *Rietveld et al. (1987)*. For each segment, the correlation coefficient, slope, and the peak  $\Delta H$  are recorded.

## 3.2 Case Studies

Before examining the statistics for the entire database, we first present several case studies that illustrate key trends.

### 3.2.1 Strong, Positive Correlation

Case 1 in Figure 3.2 is an example of strong positive correlation between the strength of the electrojet current and the HAARP generated ELF signal amplitude. The transmitted format consists of repetitions of a 2-sec tone at 2130 Hz followed by continuous wave transmission at 37.5% power, all with a HF frequency of 3.25 MHz. Note that the first minute of this experiment is shown in Figure 3.1. Because the tone is transmitted every 5 seconds, there are a large number of data points from this run. During this 30-min interval, the electrojet is relatively strong with a peak  $\Delta H$  of 225 nT, and the ELF amplitude closely tracks the magnetometer deviations. The correlation coefficient is 0.98 and the slope of the linear least squares fit is 0.01 pT/nT.

However, the correlation can be strong even with much weaker variations in  $\Delta H$ . Figure 3.3 shows Case 2 where the ELF amplitude variations of tens of femtoteslas track  $\Delta H$  variations of only a few nanoteslas. Maxima at 06:08, 06:16, 06:21 and 06:27 UT are seen in both the magnetometer and the ELF signal amplitude. Note, that the slope of the linear fit in Case 2 (weak electrojet) is double that of Case 1 (strong electrojet).

The effect of changing slope can be seen dynamically in the event of 15 March 2008 (Figure 3.4) when magnetic activity suddenly increases at around 0815 UT. While  $\Delta H$  increases from tens of nanotesla to hundreds of nanotesla, the ELF amplitude only increases from about one picotesla to two picotesla. The two regimes are also seen as two different slopes when plotting ELF amplitude against  $\Delta H$ . The weak electrojet interval corresponds to the points along the steep slope (filled circles), while stronger magnetic activity corresponds to points along the shallow slope (open circles). While both intervals have significant statistical correlation, the slope differs by a factor of almost 20.



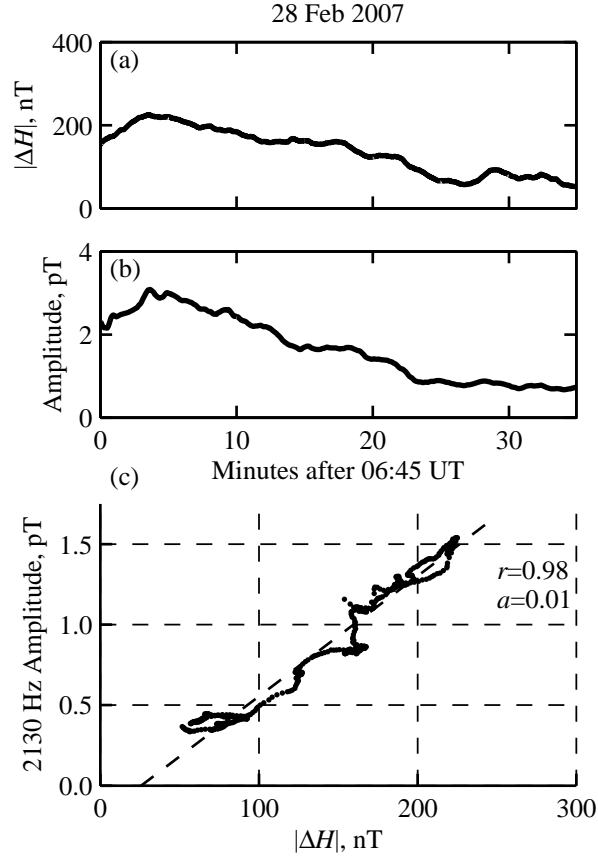


Figure 3.2: Case 1: ELF amplitude and  $|\Delta H|$  on 28 February 2007 from 0645 to 0720 UT. (a)  $|\Delta H|$ , (b) amplitude of ELF tones, (c) ELF amplitude plotted against  $|\Delta H|$ . Each point corresponds to the ELF amplitude of a single tone and the H deviation at the time the tone was transmitted. The dashed line is the linear least squares fit of the data with the correlation ( $r$ ) and slope ( $a$ ) shown. This case illustrates strong, positive, linear correlation between ELF amplitude and  $|\Delta H|$  during a period with an enhanced electrojet.

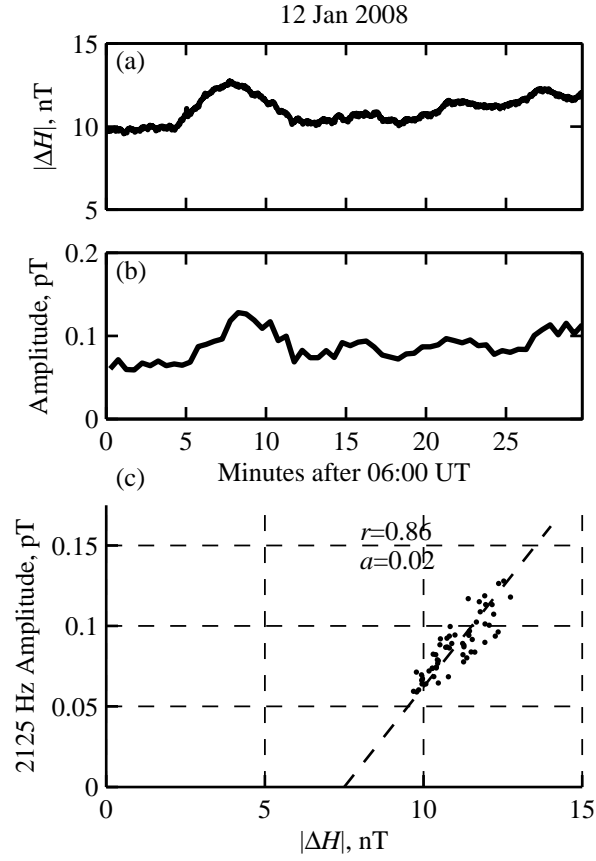


Figure 3.3: Case 2: ELF amplitude and  $|\Delta H|$  on 12 January 2008 from 0600 to 0630 UT as in Figure 3.2. There is strong correlation despite a very weak electrojet.

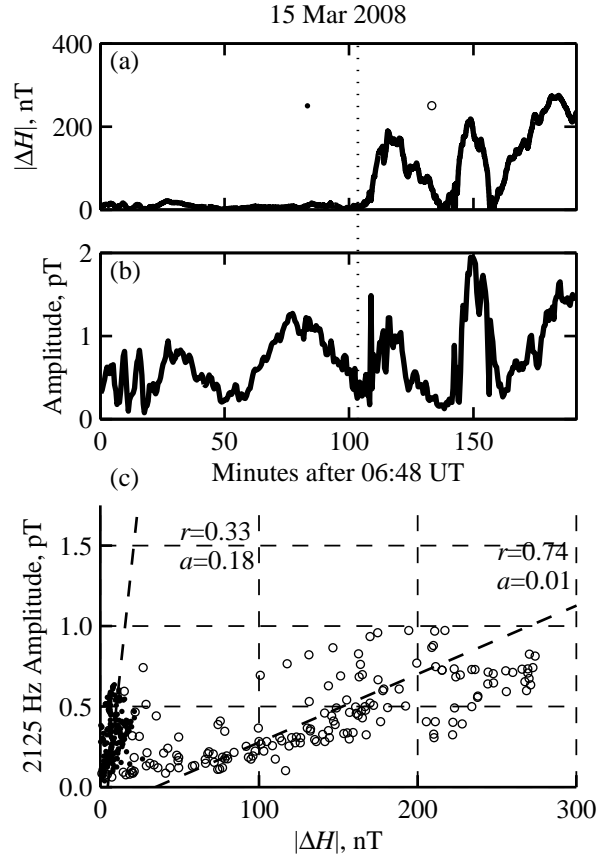


Figure 3.4: Case 3: ELF amplitude and  $|\Delta H|$  on 15 March 2008 from 0648 to 0959 UT as in Figure 3.2. (c) Points before the dotted line at 0836 UT in (a)-(b) are shown as solid dots, and points after as open circles. Changes in ELF amplitude are of similar magnitude before and after 0836 UT despite the fact that electrojet intensity changes dramatically. This is seen as a slope change in (c).

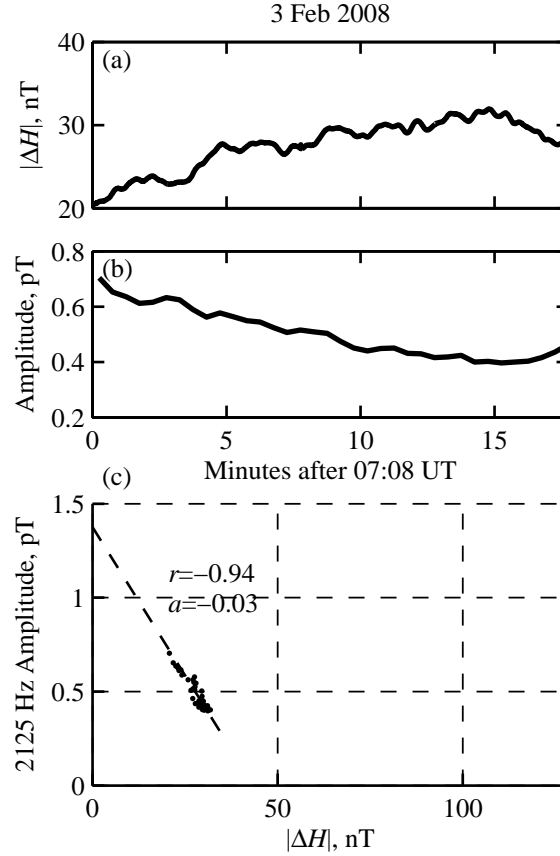


Figure 3.5: Case 4: ELF amplitude and  $|\Delta H|$  on 3 February 2008 from 0708 to 0726 UT as in Figure 3.2. There is a strong negative correlation where ELF amplitude decreases as  $|\Delta H|$  increases.

### 3.2.2 Strong Negative Correlation

At other times  $\Delta H$  and ELF amplitude remain strongly correlated but in a negative sense. Case 4 (Figure 3.5) illustrates an example of highly statistically significant negative correlation with ELF amplitude decreasing as  $\Delta H$  increases. Overall electrojet activity is relatively weak at this time with the peak  $\Delta H$  remaining below 32 nT.

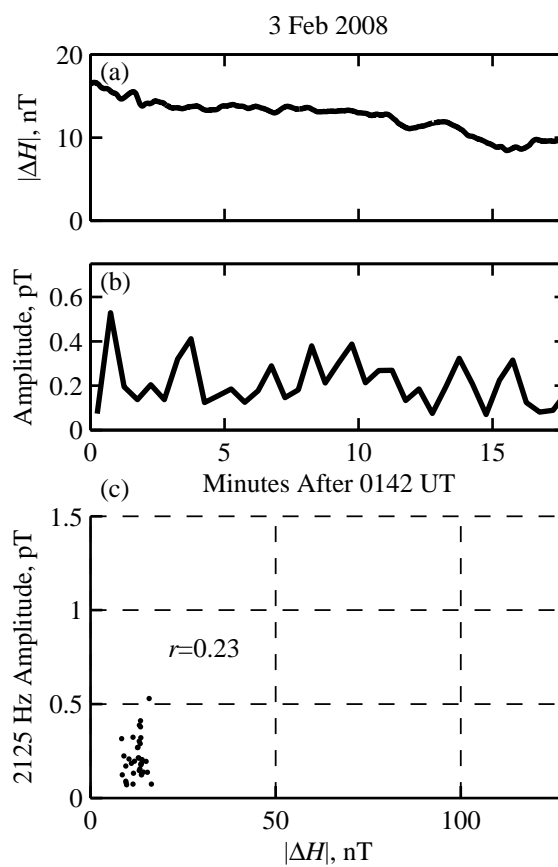


Figure 3.6: Case 5: ELF amplitude and  $|\Delta H|$  on 3 February 2008 from 0142 to 0200 UT as in Figure 3.2. The ELF amplitude is uncorrelated with  $|\Delta H|$ .

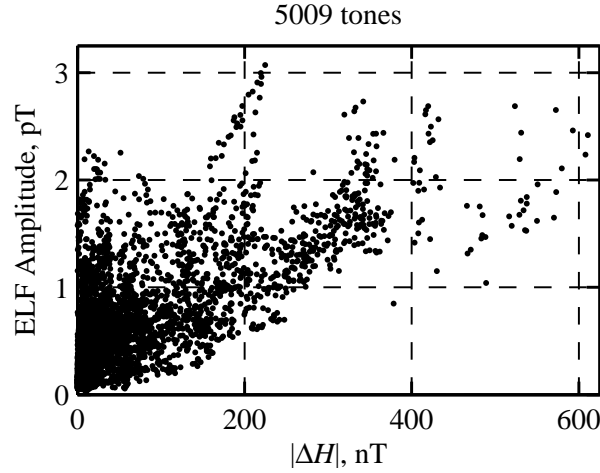


Figure 3.7: 2125 Hz and 2130 Hz ELF amplitude as a function of  $|\Delta H|$  for all cases studied. Each point corresponds to the ELF amplitude of a single tone and the  $|\Delta H|$  at the time the tone was transmitted. Experiments where the tone was repeated more often than every 30 seconds were downsampled to 1 point every 30 seconds.

### 3.2.3 Poor Correlation

Finally, Case 5 (Figure 3.6) shows an example of poor correlation. In this event, the ELF signal amplitude varies by as much as 100% between subsequent HAARP transmissions spaced 30-sec apart. In contrast,  $\Delta H$  remains fairly steadily decreasing throughout the interval. The correlation coefficient is low ( $r = 0.23$ ). The overall electrojet activity is weak, as in Case 2 of strong positive correlation and Case 4 of strong negative correlation.

## 3.3 Statistics: Occurrence Probability

We now examine statistics for all 2304 minutes of HAARP transmission during the study intervals. Figure 3.7 is a scatter plot of ELF amplitude versus  $\Delta H$ . Each point corresponds to the ELF amplitude of a single tone, at 2125 or 2130 Hz, and the  $\Delta H$  at the time the tone is transmitted. Experiments where the tone is repeated more often than every 30-seconds are down sampled to 1 point every 30 seconds. For low

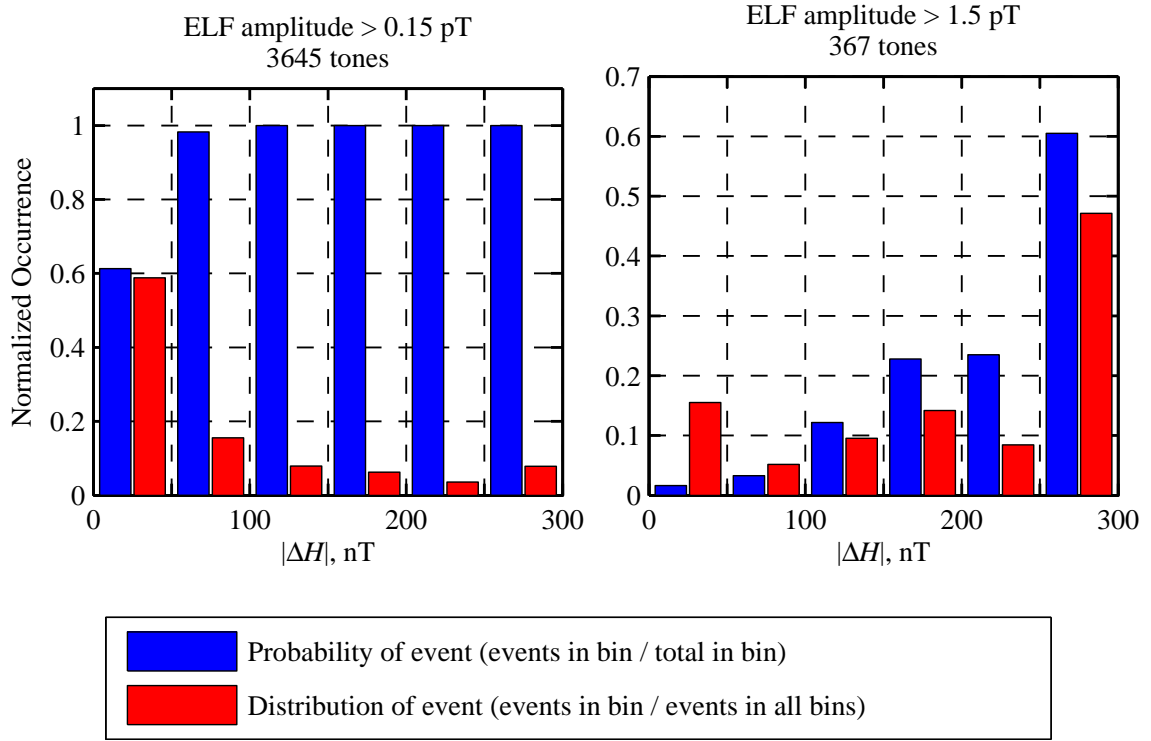


Figure 3.8: Distribution of magnetic conditions for generated ELF tones greater than 0.15 pT and 1.5 pT in amplitude. The blue bars show the probability of the ELF amplitude exceeding 0.15 or 1.5 pT for the H deviation in each bin. The red bars show the distribution of magnetic conditions for tones with ELF amplitude greater than 0.15 or 1.5 pT. Experiments where the tone was repeated more often than every 30 seconds were downsampled to 1 point every 30 seconds to avoid skewing the statistics.

values of  $\Delta H$  ( $\lesssim 100$  nT), the ELF amplitude is highly variable ranging from  $\sim 0.025$  to 2.3 pT. As  $\Delta H$  increases, the average observed ELF amplitude increases. However, the peak ELF amplitude of  $\sim 3.1$  pT observed for strong electrojet activity ( $\Delta H > 100$  nT) is only slightly higher than the peak ELF amplitude of  $\sim 2.3$  pT observed for weak electrojet conditions ( $\Delta H < 100$  nT).

The distribution of the ELF amplitudes as a function of electrojet strength is further explored in Figure 3.8. Shown are normalized occurrence probabilities for ELF amplitude which exceed a specific event threshold. The event thresholds on the left panel and right hand panels are respectively 0.15 pT and 1.5 pT. The blue and

red bars indicate two different types of normalization. The blue bars indicate the probability that the ELF amplitude exceeds the event threshold for a given range of  $\Delta H$ , i.e., the number of events in the  $\Delta H$  bin divided by the total number of events and non-events in that bin. It can be seen that for  $\Delta H > 50$  nT the ELF amplitude almost always exceeds 0.15 pT. Even for weak electrojet activity, e.g.,  $\Delta H < 50$  nT, the ELF amplitude exceeds 0.15 pT more than 60% of the time. For the higher event threshold of 1.5 pT (right hand panel), the event occurrence probability increases with increasing  $\Delta H$ , and only during the most active periods ( $\Delta H > 250$  nT) does the occurrence probability exceed 50%.

The red bars in Figure 3.8 indicate the event distribution as a function of electrojet activity. Stated another way, it is the probability that  $\Delta H$  is within a specific range when an event occurs, calculated as the number of events in the given range of  $\Delta H$  divided by the total number of events for all values of  $\Delta H$ . The sum of the red bars in each panel is equal to 1. For an event threshold of 0.15 pT, almost 60% of the events occur during low electrojet activity ( $\Delta H < 50$  nT). This result is simply due to the fact the probability that the ELF amplitude exceeds 0.15 pT is high for any level of activity and weak electrojet activity occurs far more often than strong activity. For the higher event threshold of 1.5 pT (right panel), events are most likely to occur during strong electrojet intervals ( $\Delta H > 250$  nT). However, 16% of events occur during the weakest activity, and this is the second mostly likely activity range.

To summarize the results of Figure 3.8, we find that the probability of generating ELF signal with moderate amplitude ( $\geq 0.15$  pT) is extremely high under all electrojet conditions. Strong ELF amplitudes ( $\geq 1.5$  pT) are more likely to occur when  $\Delta H$  exceeds several hundred nanotesla, yet there is still a small probability of occurrence of such large amplitudes with small values of  $\Delta H$ . This small probability is partially offset by the fact that  $\Delta H$  is small most of the time, such that the total number of strong tones generated with small  $\Delta H$  is not negligible.

It is worthwhile to note that for every HAARP transmission examined here, a detectable ELF signal is observed at Chistochina, 37 km away. The interval with the weakest ELF signal strength in the data set analyzed here is shown in Figure 3.9.



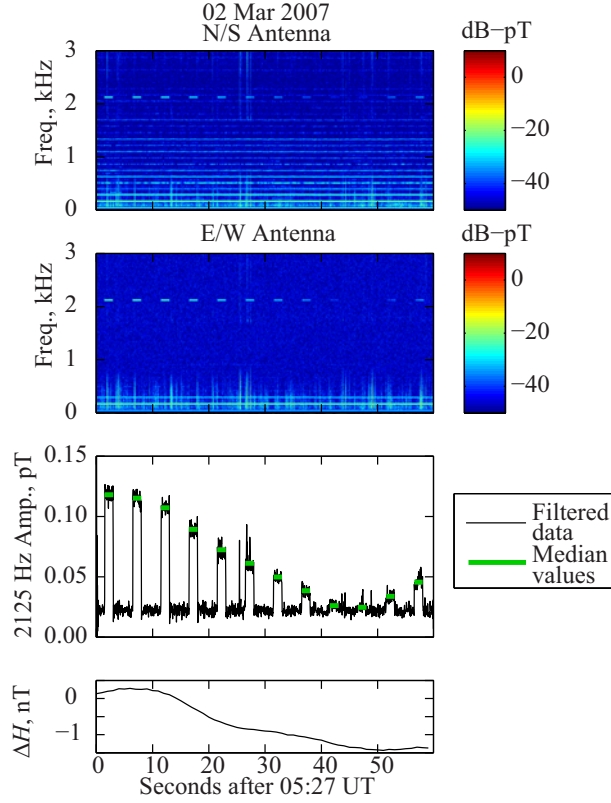


Figure 3.9: (a)-(b) Spectrogram showing ELF signals received at Chistochina, Alaska on 02 March 2007 beginning 0527 UT. (c) Amplitude of the 2125 Hz tone with both channels combined, anti-alias filtered, and downsampled for clarity. The position of the green bars on the time axis corresponds to when the 2125 Hz tone was being transmitted, and to the data values used to take the median. Their height corresponds to the median value for that tone. (d)  $|\Delta H|$ .

Electrojet activity at this time is negligible with  $\Delta H$  less than 2 nT. The ELF amplitude steadily decreases during the 1-min period shown, and the weakest pulse at 05:27:47 UT can be faintly seen in the N/S spectrogram. The amplitude of the pulse is 0.025 pT which is 0.9 dB above the background atmospheric noise during the off transmission period.

### 3.4 Statistics: Correlation

We next investigate the degree of correlation between variations in the observed ELF signal amplitude and in  $\Delta H$ . The top panel of Figure 3.10 shows the correlation coefficient,  $r$ , for each of the 128 18-min data blocks (see Section 3.1) as a function of the peak value of  $\Delta H$  in that block. Overall, 55% of the intervals exhibit statistically significant positive correlation (blue), 15% negative correlation (red) and in 30% of intervals, ELF amplitude is uncorrelated with  $\Delta H$  (black). In addition, the negative and uncorrelated intervals primarily occur during the weakest electrojet intervals with 90% of the negative intervals and 73% of the uncorrelated intervals occurring when  $\Delta H < 50$  nT. Complementarily, during strong electrojet intervals ( $\Delta H > 200$  nT), the intervals are primarily (82%) positively correlated.

The bottom panel of Figure 3.10 shows the distribution of the slope ( $a$ ) of the linear least squares fit for all intervals with statistically significant correlation as a function of the peak  $\Delta H$ . The absolute value of the slope is plotted, and red points indicate the intervals with a negative slope. Although there is considerable scatter, a trend of decreasing slope with increasing peak  $\Delta H$  is clearly evident. In other words, during weak electrojet intervals, small changes in  $\Delta H$  can result in large changes in the ELF signal amplitude. On the other hand during stronger electrojet intervals, larger changes in  $\Delta H$  are needed to observe an increase in the ELF signal amplitude. This trend is well illustrated by the case in Figure 3.4. The log scale in peak  $\Delta H$  in the bottom panel of Figure 3.10 brings out one additional trend. There appears to be slight preference for negative correlations to occur during the absolute quietest intervals with 55% of negative correlations occurring when  $\Delta H < 10$  nT.

Since our estimates of electrojet strength depend on the quiet time values of  $H$ , it

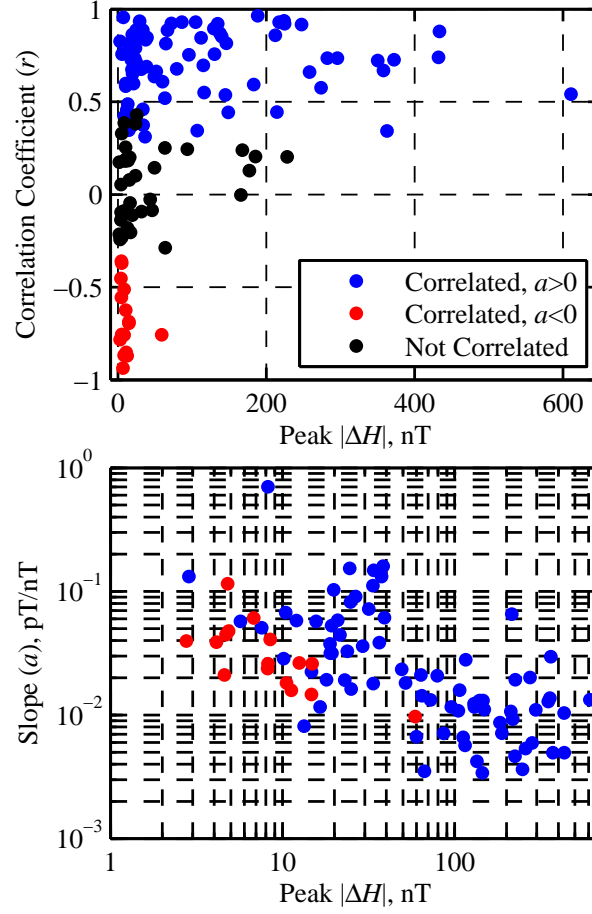


Figure 3.10: (a) Correlation coefficient of 2125 or 2130 Hz ELF amplitude and  $|\Delta H|$  plotted against peak  $|\Delta H|$  in 18 minute blocks for nighttime runs. (b) Slope of 2125 or 2130 Hz ELF amplitude and  $|\Delta H|$  plotted against peak  $|\Delta H|$  in 18 minute blocks for nighttime runs with strong correlation.

is possible that some of the negative and uncorrelated cases could be a result of errors in  $H$  causing a strengthening electrojet to be misinterpreted as a weakening one or vice versa. We observed variations in  $H$  of approximately  $\pm 10$  nT over very quiet 24-hour periods, possibly accounting for half of the negative correlation cases when  $\Delta H < 10$  nT. These errors may also explain some of the uncorrelated cases although only 30% of the uncorrelated cases occur when  $\Delta H < 10$  nT.

### 3.5 Expanded Dataset and Observations

In the previous section we explored several case studies showing good correlation between ELF amplitude and magnetometer measurements and an overall majority (55%) of periods with good correlation. However, it is also apparent from the changing ELF/ $\Delta H$  slope and periods of poor or negative correlation that magnetometers alone cannot account for all the observed variation in ELF amplitude. Fortunately, the HAARP facility has an array of other ionospheric diagnostic instruments and combining their measurements with ones from the magnetometer leads to better knowledge of how natural conditions other than the electrojet strength affects ELF generation.

First we slightly expand our dataset, still using data taken from 2007 and 2008 when HAARP was transmitting with a full-power (3600 kW), vertical, X-mode beam, modulated at 2125–2130 Hz with a 40–50% duty cycle. This totals 2596 minutes of experiment time over 20 days during nighttime at 100 km altitude. In addition we also include the 2127 minutes of daytime experiments over 20 days. Again taking the ELF amplitude as the median amplitude of a pulse (typically 1–2 seconds long), there are 6262 such pulses during nighttime and 4328 during daytime.

We continue to use  $\Delta H$  from the HAARP magnetometer as an estimate of the overhead current, i.e. the current available for HAARP to modulate. However, at times strong currents at further distances (primarily to the north as HAARP is typically located equatorward of peak electrojet) produce magnetic perturbations on the Gakona magnetometer, but they are not subject to modulation using HAARP. To explore how the spatial distribution of the currents affects ELF generation, we use the Geophysical Institute’s Geospace Environment Data Display System (GEDDS)

which provides estimates of equivalent horizontal currents at latitudes in one degree increments from  $59^\circ$  N to  $71^\circ$  N (*Sun et al.*, 1993) with 1 minute time resolution based on measurements from a chain of 6 magnetometers.

Riometer data are used to infer changes in the  $D$  and  $E$ -region ionospheric densities and are taken from the HAARP classic (non-imaging) riometer, which receives radio noise from the sky at 30 MHz. The quiet day curve containing the expected signal from the detector under quiet geomagnetic conditions is subtracted from the actual detector signal to yield the absorption in dB. Interference can result in negative absorption values when the detector signal is greater than the quiet day curve. These values are clipped to 0 dB. Data are sampled every minute.

Ionosonde data are also used to estimate changes in the  $E$ -region density. The HAARP ionosonde provided by the University of Massachusetts at Lowell uses automated algorithms to determine ionospheric parameters from ionograms. Of interest here are the  $E$  and sporadic  $E$  critical frequencies ( $f_0E$  and  $f_0Es$ ). Although such automated processing is not completely reliable, assembling a large number of observations may reveal trends in how  $E$ -region parameters affect ELF generation. The time resolution of the ionosonde dataset is 15 minutes so the relevant value corresponding to each ELF pulse is defined as the value of the closest 15 minute interval if it is given. Using this technique, 46% of the ELF receptions in this dataset are associated with sporadic  $E$  values. The software did not report  $f_0E$  for any of the nighttime cases.

An estimate of the electric field above HAARP would be an ideal diagnostic for examining ELF generation efficiency. As part of the Super Dual Auroral Radar Network (SuperDARN), the coherent scatter HF radar at Kodiak provides coverage over HAARP. These radars require the presence of ionospheric density irregularities to act as scatterers in order to determine the electric field, but unfortunately irregularities are absent at Kodiak for almost all of the ELF experiments conducted at HAARP. Thus, in order to estimate the local electric field, we use global convection maps derived from the SuperDARN array (*Ruohoniemi and Baker*, 1998; *Shepherd and Ruohoniemi*, 2000). In this approach, ionospheric convection velocities derived from the SuperDARN network are fitted to an expansion of the electrostatic

potential in terms of spherical harmonic functions. A statistical model, which is dependent on the IMF direction, is used to constrain the solution in regions where no SuperDARN data are available. The resulting convection maps are optimized towards large scale convection patterns and are not ideal for resolving small-scale features over HAARP (*Chisham et al.*, 2007). The local electric field at HAARP is interpolated from the global convection map and the northward component of the field is available every 10 minutes.

Figure 3.11 summarizes data from each of the instruments. The data are from an approximately 3-hour experiment starting on 15 March 2008 at 06:48 UT, the same period as Case 3 shown in Figure 3.4. The panels from top to bottom show a) ELF amplitude at Chistochina, b)  $\Delta H$  from the Gakona magnetometer, c) riometer absorption at HAARP, d) the magnitude of the estimated northward component of the electric field at HAARP from the SuperDARN network ( $|E_N|$ ), e) the spatial distribution of the electrojet current density ( $J$ ) derived from the magnetometer array. There were only a few points where the ionosonde detected a sporadic  $E$  layer so  $f_0E_s$  is not shown. Near 0836 UT a substorm occurred with  $\Delta H$  approaching 300 nT. However, ELF amplitude during the substorm only reaches 2 pT compared to amplitudes around 1 pT during the quiet period. Riometer absorption is very low in the hour before substorm onset, then increases to  $\sim 1$  dB. The electric field is varying throughout. The electrojet currents in Figure 3.11e also intensify during the substorm but mostly at latitudes between  $65^\circ$  N to  $70^\circ$  N, which are north of HAARP ( $62.39^\circ$  N). ELF generation is correlated with  $|\Delta H|$  both before (correlation coefficient = 0.33) and after (correlation coefficient = 0.74) the substorm. The proportionality constant (0.18 pT/nT before the substorm and 0.01 pT/nT after) is clearly different. This disparity and its relationship to the larger values of riometer absorption and other ionospheric parameters during the substorm is quantified below with statistical and theoretical models.

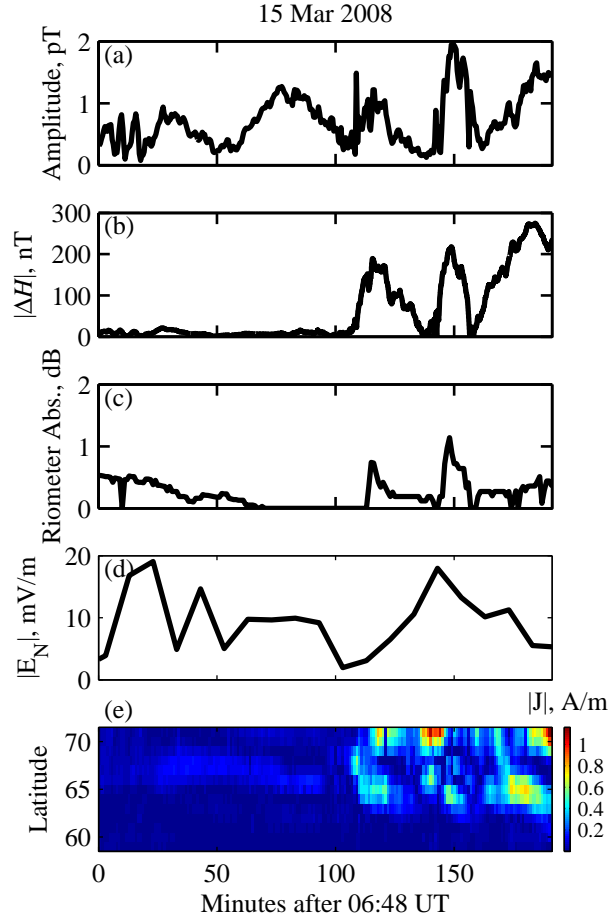


Figure 3.11: (a) 2125 Hz ELF amplitude at Chistochina, Alaska from 0648 to 0959 UT; (b)  $|\Delta H|$  at Gakona, Alaska over the same period showing an increase in activity at 0836 UT. The increase in ELF amplitude after 0836 UT is less dramatic. (c) Riometer data show low absorption immediately before 0836 UT and high absorption afterwards; (d) northward component of the electric field from SuperDARN is not substantially stronger after 0836 UT than before; (e) electrojet intensifies substantially after 0836 but mostly at higher latitudes.

## 3.6 Statistical Model

### 3.6.1 Methodology

In order to further examine the efficiency of ELF generation, we create a statistical model of ELF strength as a function of multiple ionospheric parameters. We use a neural network to fit the detected ELF signal strength at Chistochina to different combinations of magnetometer, riometer, E and sporadic E critical frequency, and electric field inputs. A neural network is one technique for fitting a multidimensional input data set to an output set. Once the network is trained by fitting known measurements, it can then estimate the ELF strength when given new values for the inputs.

The neural network used here consists of a layer of 10 hidden neurons and an output layer of a single neuron. The hidden layer neurons each receive the inputs, find a weighted sum, apply a bias, and pass them through a hyperbolic tangent function. The output neuron receives the outputs from the hidden layer neurons, weighs and biases them, and then passes the result through a linear function whose output is the output of the model. The weights and biases are determined with a training algorithm on data randomly selected from 70% of the input data with the remaining 30% used for testing and validation. Training involves choosing a set of weights and biases that minimizes the network's squared error (the squared difference between the network's output and the measured data). This can be a difficult problem because of the large number of parameters that must be adjusted. For example, the 10 neurons in the hidden layer with 2 inputs have 20 weights and 10 bias values that must be chosen. Several algorithms can be used to find a local minimum for the network's error over this 30 dimensional space. These are usually iterative algorithms that start at some value for the network's parameters, choose a new value for the parameters (based on the gradient of the network's error function for example) and repeat until it meets some stopping criteria. We use the Levenberg-Marquadt training algorithm as it provides good performance and is fast for the size of the network we use (*Hagan and Menhaj, 1994*). See *Fine (1999)* for a good introduction to this neural network architecture including a summary of training algorithms. The Neural



| Inputs                           | Night |          | Day  |          |
|----------------------------------|-------|----------|------|----------|
|                                  | $r$   | # points | $r$  | # points |
| $ \Delta H ,  E_N $              | 0.81  | 6262     | 0.6  | 4322     |
| $ \Delta H $ , Riometer          | 0.87  | 6262     | 0.6  | 4326     |
| $ \Delta H $ , Riometer, $ E_N $ | 0.88  | 6262     | 0.67 | 4322     |
| $ \Delta H , f_0 E$              | -     | 0        | 0.79 | 1175     |
| $ \Delta H , f_0 E_s$            | 0.90  | 2875     | 0.85 | 922      |
| $ \Delta H , f_0 E_s$ , Riometer | 0.94  | 2875     | 0.92 | 922      |
| J, Riometer                      | 0.75  | 5209     | 0.73 | 3661     |
| J, $f_0 E_s$                     | 0.88  | 2604     | 0.78 | 893      |

Table 3.1: Neural networks constructed, the correlation coefficient ( $r$ ) between model output and measurements, and number of ELF receptions available for training.

Network Toolbox in the MATLAB software package was used to perform the fitting.

Neural networks have a disadvantage in that the weights and biases that compose the inner workings of the neural network provide no insight as to how the inputs affect the outputs. For example, multiple linear regression, an alternate technique for multidimensional fitting, assigns coefficients to each input and the magnitude and sign of these coefficients can indicate the significance of each input to the output and whether the input is directly or inversely related to the output. For neural networks, an alternative is to sweep one or two inputs at a time while holding the remaining ones constant. Plotting how the output changes with input can then reveal any relationships between the inputs and output. We choose to use neural networks because they have the advantage of scaling easily as the number of input vectors increase and fitting complex relationships between outputs and inputs where it is more difficult to achieve good results using other techniques such as multiple linear regression.

We construct several neural networks each with ELF amplitude measured at Chistochina as the output and combinations of  $|\Delta H|$  from the HAARP magnetometer, electrojet current from a magnetometer chain,  $E$  and sporadic  $E$  layer critical frequencies, and  $|E_N|$  from SuperDARN as inputs. The results are summarized in Table 3.1 which lists the inputs to each network, the correlation coefficient between the model

output and measured output of ELF amplitude, and the number of data points available for training and testing the model.

The statistical model using only  $|\Delta H|$  and riometer absorption performs well with a correlation coefficient of 0.87 between the model output and measured ELF amplitudes for all nighttime data. The model using  $|\Delta H|$  and  $|E_N|$  also performs well with a correlation coefficient of 0.81. Including all 3 instruments only increases the correlation to 0.88 indicating that a model using only a magnetometer and either the riometer or the electric field is sufficient. We choose to drop the electric fields and focus on models utilizing the magnetometer and riometer. Although a statistical model utilizing only the magnetometer and electric field was able to reproduce measured data reasonably well, the actual output of the model is difficult to interpret and not physically intuitive. We could not discern any clear relationship between the electric field and ELF generation, which may indicate that the SuperDARN data are not reliable for this purpose due to the lack of irregularities above HAARP. A time resolution of 10 minutes also forced us to interpolate which may increase errors further though both linear and cubic spline interpolation were tried.

A similar model using sporadic  $E$  critical frequency measurements from the HAARP ionosonde instead of riometer absorption performed slightly better in nighttime cases when this measurement was available, resulting in a correlation coefficient of 0.90. When combined with riometer data, a correlation coefficient of 0.94 was achieved.

The daytime model using  $|\Delta H|$  and riometer has worse performance than the nighttime model with a correlation coefficient near 0.6. Including  $E$  and sporadic  $E$  critical frequency in the model improves the correlation but only over a very narrow range of input values. The largest daytime value for  $|\Delta H|$  was only 61 nT when only including cases with sporadic E data and only 50 nT when only including cases with  $E$  layer data.

A concern with relying on the HAARP magnetometer is detection of strong currents much further north than HAARP that would not contribute to ELF generation. Figure 3.12a shows the intensity of the current at each of these latitudes for HAARP transmissions which resulted in ELF amplitudes along the  $x$ -axis. The ELF amplitudes are sorted by amplitude. When ELF amplitudes were stronger (towards the

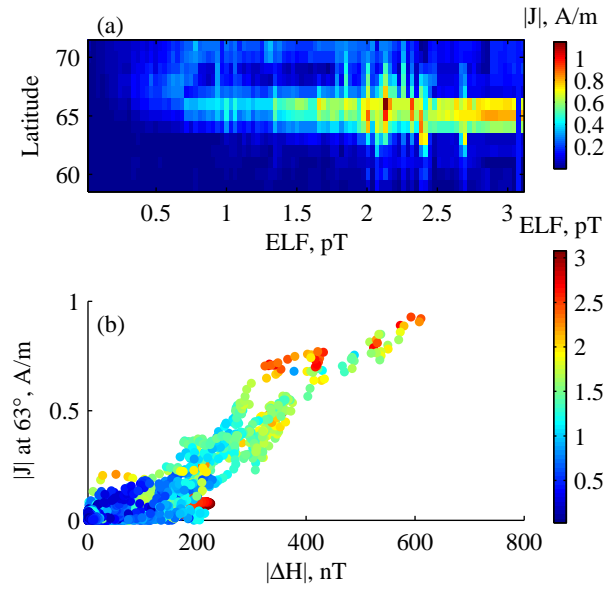


Figure 3.12: (a) Median electrojet current over latitude in cases where ELF intensity was in a given bin. (b) Electrojet current at HAARP’s latitude plotted against  $|\Delta H|$  showing generally good correlation, but with cases where  $|\Delta H|$  is high compared to the overhead current. ELF intensity is shown in color.

right), the currents not only intensify but also move southwards. To ensure that the magnetometer is a reasonable measure of the overhead current we plot the current at HAARP's latitude as a function of  $|\Delta H|$  measured with the Gakona magnetometer in Figure 3.12b. ELF amplitude is shown in color. The correlation between the two is strong, indicating that the magnetometer is an acceptable diagnostic of the overhead currents although there are still points where the magnetometer overestimates the overhead current. However, using the equivalent current at HAARP's latitude instead of the Gakona magnetometer resulted in slightly worse correlation between the statistical models and data (e.g. 0.75 versus 0.87 when also using riometer data). The magnetometer has better time resolution, sits directly under the heated region, and is thus more sensitive to local variations in the current instead of being a single current estimate over a swath of latitude. Thus we use  $|\Delta H|$  in all the statistical models instead of the computed electrojet current.

We present detailed results of three models, the  $|\Delta H|$  and riometer model for both daytime and nighttime and the  $|\Delta H|$  and  $f_0 E_s$  model for nighttime. Models with more than two input variables are more difficult to visualize and not discussed.

### 3.6.2 Riometer Results

The results of the nighttime neural network model using magnetometer and riometer data as input show that for a given value of  $\Delta H$ , lower values of riometer absorption result in stronger ELF amplitudes. Figure 3.13 shows the output of the model, ELF amplitude, by color plotted against input values of  $|\Delta H|$  and absorption. The black dots indicate the measurements that were used to train the model, and the model output is blanked out where there was insufficient input training data. The statistical model shows that the strongest ELF occurs when  $\Delta H$  is high and riometer absorption is near zero. Figure 3.13 also plots the predicted ELF intensity against  $\Delta H$  at 10 riometer values. ELF increases roughly linearly with  $\Delta H$  with all lines crossing near the origin as expected. As riometer absorption increases from 0 dB to  $\sim 0.2$  dB, the slope of the lines decreases from 0.01 pT/nT to 0.005 pT/nT. As the absorption increases further, the slope stops decreasing and starts increasing again to roughly

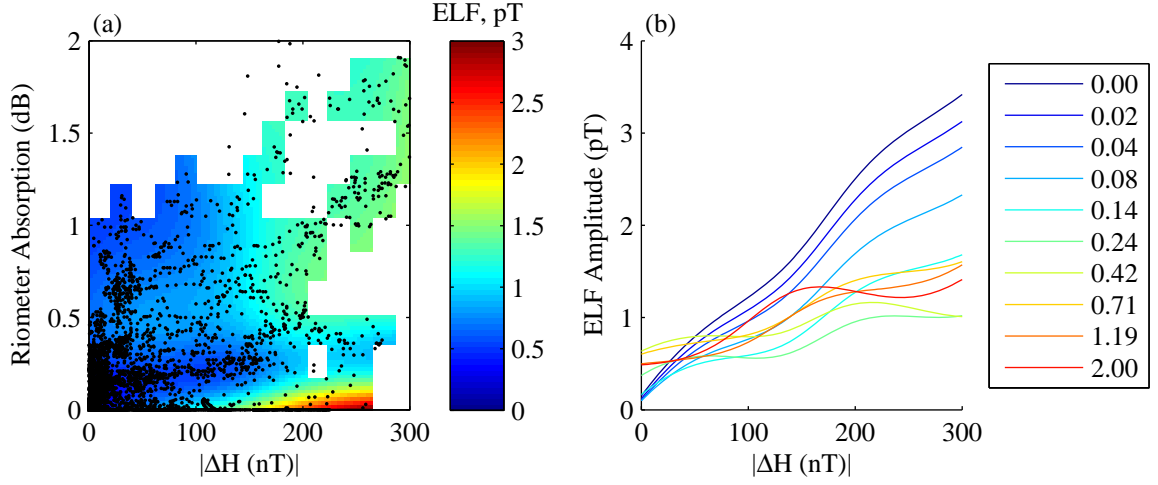


Figure 3.13: (a) Output of nighttime neural network model showing predicted ELF amplitude as a function of input values of riometer absorption and  $|\Delta H|$ . ELF amplitude increases with  $|\Delta H|$  but more so with lower absorption values. Black dots indicate the measurements that were used to train the model. (b) ELF amplitude as a function of  $|\Delta H|$  shows decreasing slope as riometer absorption increases.

0.007 pT/nT although this is still smaller than the slopes at low absorption values less than 0.1 dB. The model may be less accurate at higher absorption values because less data are available. The range of slopes is consistent with those found by least squares fitting to 18 minute blocks of data shown in Section 3.4.

The results of the daytime model in Figure 3.14 again with  $\Delta H$  and riometer shows similar results. Because the range of  $\Delta H$  and absorption values is more limited, we only show the output to 100 nT of  $|\Delta H|$  and 1 dB of absorption. ELF amplitude still linearly increases with  $|\Delta H|$ , with higher absorption values corresponding to smaller proportionality constants.

### 3.6.3 Ionosonde results

The result of the nighttime neural network using  $\Delta H$  and sporadic E critical frequency ( $f_o E_s$ ) is shown in Figure 3.15. The results are similar to the neural network model using riometer absorption where the strongest ELF for a given  $|\Delta H|$  occurs at smaller

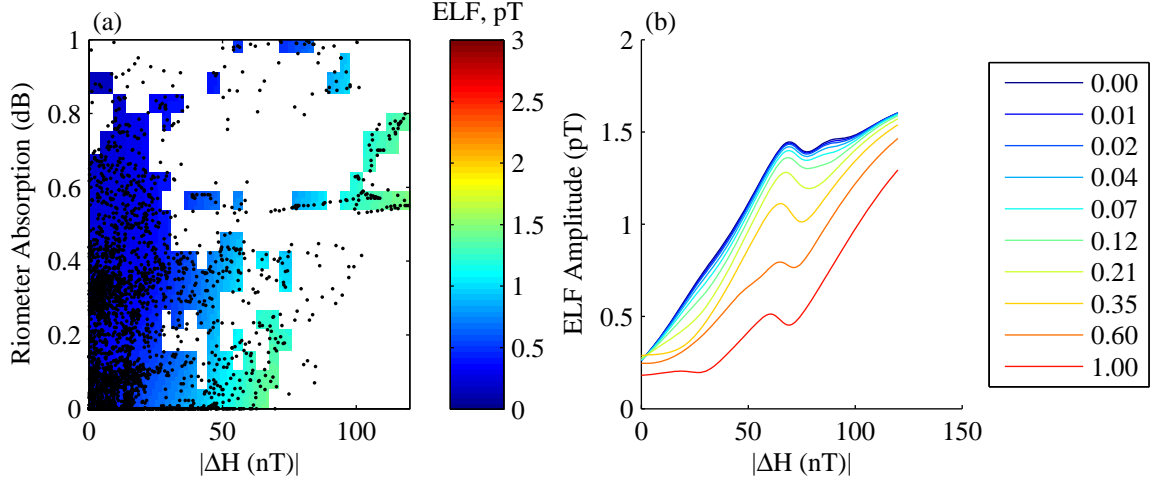


Figure 3.14: Output of daytime neural network model as in Figure 3.13. ELF still increases with  $|\Delta H|$  with decreasing slope as riometer absorption increases.

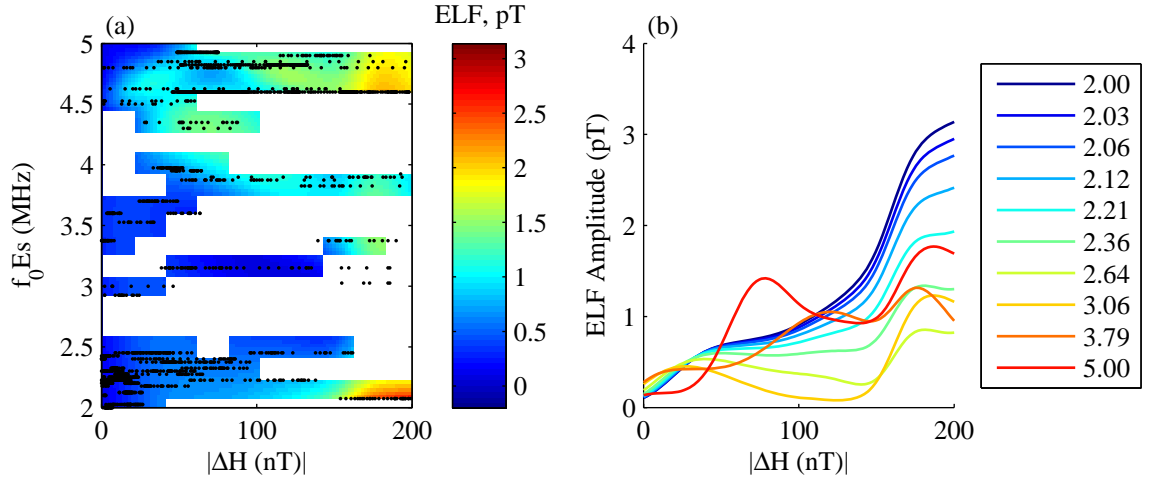


Figure 3.15: Output of nighttime neural network model showing predicted ELF amplitude as a function of input values of sporadic E critical frequency and  $|\Delta H|$ . ELF amplitude increases with  $|\Delta H|$  but more so with lower critical frequencies. Black dots indicate the measurements that were used to train the model. ELF amplitude as a function of  $|\Delta H|$  shows decreasing slope as critical frequency increases.

values of  $f_0Es$  and ELF increases with  $|\Delta H|$  with a proportionality constant that decreases as  $f_0Es$  increases. The slopes of the lines decrease from 0.016 pT/nT to 0.005 pT/nT as  $f_0Es$  increases from 1 MHz to 2.6 MHz before increasing slightly to 0.008 pT/nT as  $f_0Es$  reaches 5 MHz. This is consistent with higher  $E$ -region densities favoring strong electrojets and  $\Delta H$  more than ELF generation in the lower  $D$ -region resulting in lower proportionality constants. Direct examination of ionograms for a large number of cases could lead to a more nuanced understanding of what ionospheric conditions lead to better ELF generation.

### 3.7 Experimental Summary

HAARP is capable of ELF generation under all magnetic conditions. For the intervals examined here, all generated ELF tones are detectable at a distance of 37 km away from HAARP with 73% of the tones having an amplitude exceeding 0.15 pT. The strongest ELF amplitudes ( $>1.5$  pT) most often occur during periods of enhanced electrojet, but weak electrojet activity at times can result in equally high signal amplitudes. The relative change in ELF amplitude per unit change in electrojet current strength is dependent on the absolute strength of the current with large (small) ELF amplitude changes occurring when the electrojet is weak (strong).

When both  $|\Delta H|$  and data from the riometer or ionosonde are included in statistical models, both the  $|\Delta H|$ -Riometer and  $|\Delta H|$ -Ionosonde statistical models show that ELF intensity increases with  $|\Delta H|$  for any fixed value of riometer absorption or  $f_0Es$  respectively. How much ELF increases with  $|\Delta H|$  depends on riometer absorption and  $f_0Es$ , where higher values of either lead to smaller increases in ELF intensity (smaller ELF/ $|\Delta H|$  slopes) and smaller values lead to larger increases in ELF (larger ELF/ $|\Delta H|$  slopes). Both riometer absorption and  $f_0Es$  are measurements of density in the lower ionosphere, indicating that for a given electrojet current, one flowing through a less dense ionosphere is more favorable for ELF generation than one flowing through a more dense ionosphere. This result is also consistent with the ELF/ $|\Delta H|$  slope decreasing as peak values of  $|\Delta H|$  in an interval increased as peak  $|\Delta H|$  and

density in the lower ionosphere are both associated with increased geomagnetic activity.



# Chapter 4

## Modeling ELF Generation

In the previous chapter, we presented case studies and statistical models showing that ELF amplitude is typically well correlated with electrojet current, though ionospheric electron density also affects the relationship. While statistical modeling is helpful in uncovering relationships between many variables, it does not reveal why those relationships arise. In this chapter we use numerical models to verify that changes in the electron density profile affect ELF generation as observed in experiments and to reveal the physics behind the interaction between electron density, the electrojet current, and ELF generation.

### 4.1 Theoretical Basis

One interesting result of our analysis is that the slope of the linear least squares fit of ELF amplitude to  $\Delta H$  (Figure 3.10b) decreases with increasing strength of the electrojet current and with increasing ionospheric density as measured by a riometer or ionosonde (Figures 3.13 and 3.15). We can interpret this result in terms of high-latitude electrodynamics and HF heating efficiency. The auroral current system ( $\mathbf{J}$ ) is dynamically driven by the global convection electric field in the presence of the high conductivity auroral ionosphere, expressed as:

$$\mathbf{J}(t) = \bar{\sigma}_0(t) * \mathbf{E}(t) \tag{4.1}$$

where we explicitly recognize that both the large-scale electric field ( $\mathbf{E}$ ) and the anisotropic conductivity tensor ( $\bar{\sigma}$ ) can vary with time on the scale of several minutes and  $*$  is the convolution operator. Thus, an increase in strength of the electrojet current can result from an increase in the electric field or from enhanced auroral particle precipitation, which leads to higher conductivity, or both. The  $\Delta H$  determined from ground-based magnetometers measure deflections in the Earth's main field caused by the east-west component of the auroral electrojet current, predominately a Hall current given by the north-south component of  $\mathbf{E}$  multiplied by the Hall conductivity (*Baumjohann, 1982*).

Similarly, source currents ( $\Delta \mathbf{J}_\omega$ ) for the radiated ELF waves depend on the electric field and modulated conductivity ( $\Delta \bar{\sigma}_\omega$ ) produced by the HF heating amplitude modulated at frequency  $\omega$ :

$$\Delta \mathbf{J}_\omega(t) = \Delta \bar{\sigma}_\omega(t) * \mathbf{E}(t) \quad (4.2)$$

where once again the time variation refers to several minute-scale variations in these parameters rather than ELF modulation time scale. The magnitude of  $\bar{\sigma}_\omega$  depends on the ambient  $\bar{\sigma}_0$  (in turn a function of the electron density and temperature) and the change in electron temperature caused by the HF beam. While changes in  $\mathbf{E}$  affect both  $\mathbf{J}$  and  $\Delta \mathbf{J}_\omega$  resulting in positive linear correlation, it is possible for  $\bar{\sigma}_0$  and  $\bar{\sigma}_\omega$  to change independently of each other. Changes in the ionosphere associated with an increase in electrojet intensity may also be responsible for decreases in heating efficiency. For example, past work using ionospheric heating models have shown that the HF-induced electron temperature change is inversely proportional to the ambient electron density (*Tomko, 1981*).

Thus, the slope change that occurs in the relationship between ELF amplitude and  $\Delta H$  could directly result from poorer heating efficiency during periods of strong magnetic activity. During periods of weak activity, even though  $\mathbf{E}$  is weak, auroral particle precipitation is also weak, so that  $\bar{\sigma}_0$  is low and heating efficiency,  $\bar{\sigma}_\omega$ , is high, accounting for the relatively frequent occurrence of high ELF amplitudes during quiet conditions. During a geomagnetic substorm,  $\mathbf{E}$  increases but auroral particle

precipitation is also enhanced, thus heating efficiency decreases as seen by the decrease in the rate of change of ELF amplitude as a function of  $\Delta H$ .

The interplay between the effects of changes in  $\mathbf{E}$  and changes in particle precipitation (affecting  $\bar{\sigma}_0$ ) could also explain the occurrence of intervals of negative correlation between ELF amplitude and  $\Delta H$ . First, note that 90% of negative correlations occur when  $\Delta H < 50$  nT. Suppose that during these intervals,  $\mathbf{E}$  remains at a low and constant amplitude, and thus, changes in the observed electrojet current ( $\mathbf{J}(t)$ ) are solely due to changes in  $\bar{\sigma}_0$ . If particle precipitation is enhanced,  $\bar{\sigma}_0$  and thus  $\mathbf{J}$  increase, but heating efficiency,  $\bar{\sigma}_\omega$ ,  $\Delta \mathbf{J}_\omega$ , and ELF amplitude decrease.

## 4.2 Theoretical Modeling

### 4.2.1 Methodology

To verify this theoretical explanation of how auroral electron precipitation and ionospheric density changes affect the electrojet-ELF amplitude relationship, we model the ELF generation using a HF heating model to determine the ELF source current and a full-wave propagation model (*Lehtinen and Inan, 2008*) to obtain the ELF source fields on the ground. In addition, we calculate the height integrated steady-state electrojet current to determine  $\Delta H$ , the change in the Earth's north-south magnetic field detected on the ground.

The HF heating and ELF/VLF propagation components of the model are described in detail in Chapter 2 and are used to obtain simulated ELF amplitudes on the ground at Chistochina's location.

The ambient electrojet conductivity tensor is calculated directly from the electron density and collision rates of the ionosphere assuming they do not vary across the horizontal direction. Assuming an electric field and applying Ohm's law gives the ambient currents. These are the DC currents of the electrojet and entirely separate from the ELF source current computed using the HF heating model. The ambient currents are integrated in height and scaled according to *Kamide et al. (1982)* to obtain a simulated value for  $\Delta H$  on the ground.

### 4.2.2 Model Inputs

Since both the ELF source currents and the electrojet current scale linearly with the electric field, we assume a constant (geomagnetic) northward electric field of 1 mV/m and assume that changes in ELF generation and electrojet current are due to changes in the electron density profile. Density changes affect the ELF conductivity modulation and ambient conductivity differently and thus the ELF and ambient currents differently. Because the *D*-region is poorly understood, reliable electron density profiles do not exist. Three profiles that have provided good agreement with experimental data in mid-latitude lightning studies are Profiles I, II, and III in *Pasko and Inan (1994)*. The empirical model of *McKinnell and Friedrich (2007)* is also available and uses solar zenith angle, riometer absorption, Ap index (a index of geomagnetic activity at mid-latitudes), and F10.7 (an index of solar UV activity). The model incorporates data from incoherent scatter radars, which are plentiful at higher altitudes, but below 60 km, data are sourced from small numbers of rocket measurements. As a compromise, we use the *McKinnell and Friedrich (2007)* model but replace electron densities below 82 km with an exponentially decreasing profile consistent with Profiles I, II, and III. As an input to the auroral ionosphere model, we use the latitude and longitude from HAARP and time of Mar. 15, 2008, 01:00 UT and a F10.7 value of 140. The actual F10.7 values through 2008 were much lower due to an extended solar quiet so a higher value was chosen as the *McKinnell and Friedrich (2007)* model has better data coverage at the higher F10.7 values. Ten ionospheric profiles were then created by selecting 10 values of riometer absorption logarithmically spaced between 0 and 2 dB and corresponding values of Ap linearly spaced between 0 and 30. Figure 4.1a shows each of the 10 electron density profiles colored by the riometer absorption value used to create them. Higher values of absorption generally lead to higher electron densities. The HF heating model then determines the electron-neutral collision frequency using an empirical formula from *Banks (1966)* and a neutral density profile from the MSIS model. The HF heating simulation is conducted with a vertical full-power beam profile at 2.75 MHz in X-mode, consistent with the experiments used in the dataset.

The same electron density profiles are used in the HF heating model, full-wave propagation model, and the ambient current calculation. In all cases we assume

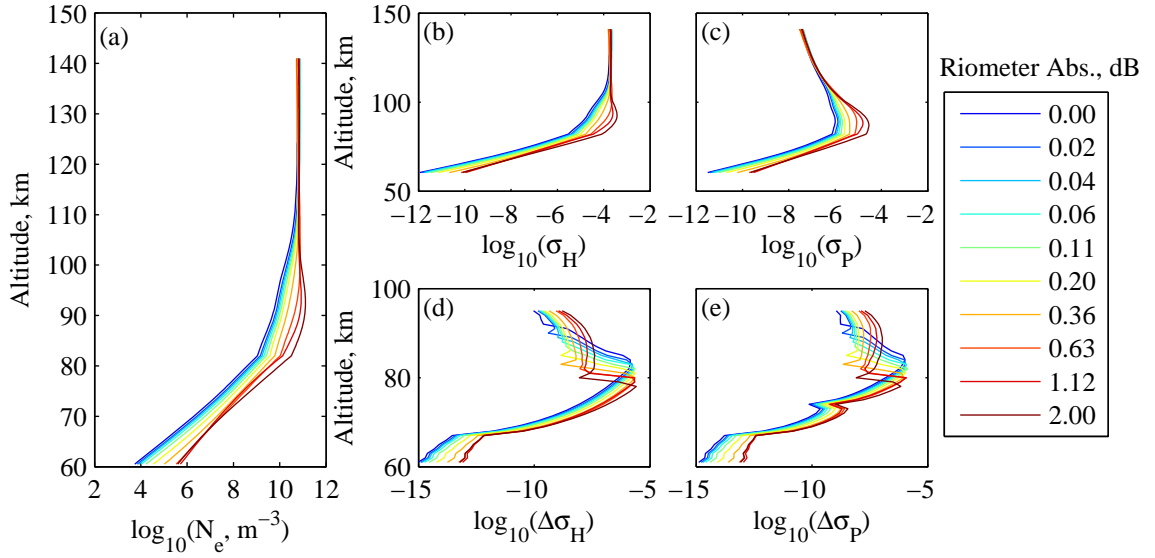


Figure 4.1: (a) Electron density profiles; (b)-(c) resulting Hall and Pedersen ambient conductivities; (d)-(e) modulated ELF conductivities from simulation. The ambient conductivities increase with electron density uniformly. Modulated ELF conductivities also increase with electron density with decreasing altitude of peak modulation.

the ionosphere does not vary horizontally at a fixed altitude. We perform the HF simulation at altitudes from 60–95 km where the majority of the ELF currents are produced. The ambient current calculations are performed over a wider altitude range from 60–140 km (the maximum valid altitude of the ionospheric density model) to include the higher altitude range where the peak of the electrojet flows.

### 4.2.3 Model Results

Figure 4.1b-c shows the Hall and Pedersen conductivities respectively computed directly from each of the electron density profiles in Figure 4.1a. Both conductivities are higher when the electron densities are increased, with the Hall conductivity being more dominant than the Pedersen conductivity especially above 100 km. Thus, elevated ionospheric densities indicated by higher riometer absorption leads directly to elevated ambient conductivities in the ionosphere and stronger currents for a given

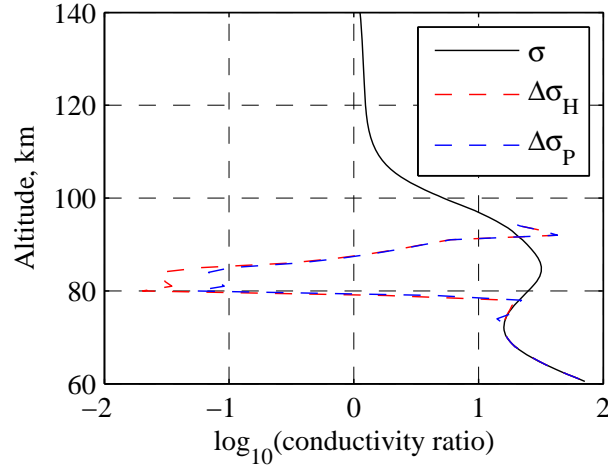


Figure 4.2: The ratio between simulated conductivities for the most dense ionosphere to conductivities for the least dense ionosphere as a function of altitude. The ambient Hall and Pedersen conductivities scale with electron density in the same way and are higher with the most dense ionosphere at all altitudes. The modulated Hall and Pedersen conductivities do not improve as much as the ambient conductivities.

electric field.

Figure 4.1d-e shows the modified Hall and Pedersen conductivities from the HF heating model at each altitude in the center of the HAARP beam. In contrast to the ambient conductivities these do not show an obvious trend as ionospheric density increases. The modified Hall conductivity is generally larger than the Pedersen conductivity and increases with altitude before reaching a maximum near 80-90 km after which it drops off as most of the HF power has already been absorbed. The altitude of this maximum decreases for profiles with higher ionospheric density a result consistent with *Payne* (2007) and *Barr and Stubbe* (1984). Current sources lower in altitude typically improve coupling into the Earth-Ionosphere waveguide. However, while the magnitude of the modified Hall conductivity increases with higher ionospheric density below the peak altitude, above the peak the modified conductivity decreases more rapidly for the denser profiles. This is more apparent in Figure 4.2 which shows the ratio between the conductivities simulated with the most dense profile and least dense profile. For example a ratio of 1 indicates that the conductivity

for the most dense profile is the same as for the least dense profile. The ambient conductivity ratio is shown in the solid line and is the same for both the Hall and Pedersen conductivities as they both respond to electron density in the same way. The ambient conductivity is an order of magnitude larger for the densest profile compared to the least dense profile below 95 km. The ratio for the modulated conductivity is smaller than the ambient conductivity. The densest ionosphere actually produces less conductivity modulation than the least dense ionosphere above 80 km ( $\sigma$  ratio less than 1). At most altitudes, the ambient conductivity benefits more from a denser ionosphere than the modulated conductivity. To directly compare the effect of different density profiles on the ambient DC electrojet current and the modulated ELF source current, we use the results of the full-wave model to obtain the magnetic fields on the ground.

The outputs of the full-wave model are shown in Figure 4.3a along with the simulated value of  $|\Delta H|$  obtained from the ambient conductivities. Each point corresponds to one of the ionospheric density profiles from Figure 4.1a with its position showing the resulting ELF amplitude from the full-wave model against the resulting  $|\Delta H|$  from the ambient currents when normalized using an electric field of 1 mV/m. The points corresponding to the denser profiles show increased ELF amplitudes, but this increase is smaller than increases in  $|\Delta H|$ . For example, the point furthest right has a  $|\Delta H|$  value over twice as large as the point furthest to the left but an ELF amplitude only 1.6 times as large.

Since changes in the electric field would affect both the ELF and electrojet fields linearly, the proportionality constant between ELF and  $|\Delta H|$  is fixed for a given density and found by dividing the normalized ELF fields by the normalized electrojet field. Figure 4.3b shows the ELF/ $|\Delta H|$  slope, ranging from 0.024 pT/nT for an absorption value of 0.36 dB to 0.016 pT/nT for an absorption value of 2 dB. Figure 4.3c shows an ELF versus  $|\Delta H|$  plot for half of the different ionospheric profiles. This plot is similar to Figure 4.3a except that each point now sweeps out a line when the electric field is varied. The slope of each line generally decreases with denser ionospheric profiles.

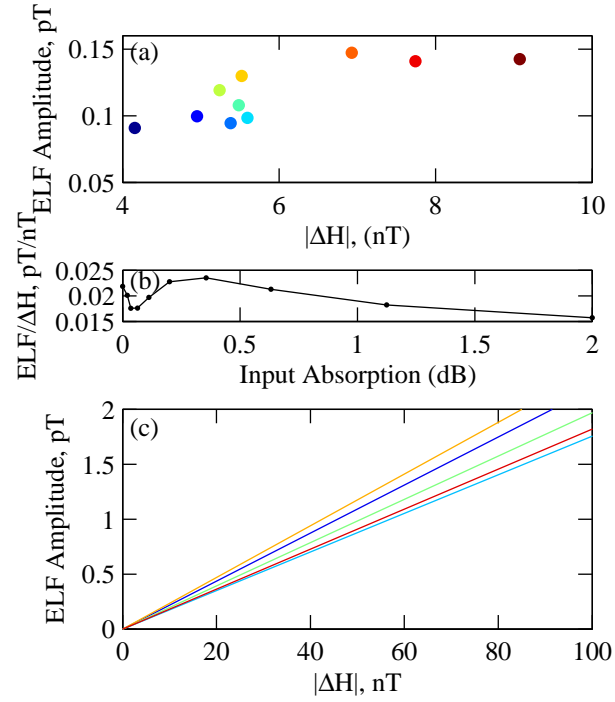


Figure 4.3: (a) Simulated ELF amplitude as a function  $|\Delta H|$  using  $E = 1\text{mV/m}$  using ionospheric density profiles generated from riometer absorption values; (b) ELF amplitude/ $|\Delta H|$  slope as a function of riometer absorption values.  $|\Delta H|$  increases more quickly with higher absorption than ELF amplitude resulting in decreasing slope of  $\text{ELF}/|\Delta H|$ . (c) How ELF amplitude and  $|\Delta H|$  vary for each ionosphere as electric field changes. For clarity only half the lines are shown.



This range of proportionality constants is consistent with that determined statistically. This also accounts for the two distinct regimes in the example of March 15, 2008 from Figure 3.11, where the quiet period corresponds to a higher proportionality constant and a less dense ionosphere, and the disturbed period to a lower proportionality constant and a more dense ionosphere. There is however an increase in slope with higher riometer absorption when the absorption was between 0.04 and 0.36 dB. This is likely due to the ionospheric density profiles used. The density at low altitudes increases with higher absorption, but it can decrease at higher altitudes (Figure 4.1a) with the result that the height-integrated conductivity fails to increase as much as expected. ELF generation improves slightly from the enhanced low-altitude density while  $|\Delta H|$  remains roughly constant leading to the increasing slope in this regime. There is still an overall trend of decreasing slope with higher absorption.

### 4.3 Discussion

The results from the statistical and theoretical models can provide insight into how natural ionospheric conditions affect ELF generation. At nighttime, in the simplest case, if ionospheric density is steady and there are only variations in the electric field, then ELF generation and magnetometer measurements will be well correlated. The proportionality constant between the two is then related to ionospheric density, which can be estimated using riometer absorption. The statistical model showed this as a linear increase in ELF intensity with  $|\Delta H|$  for a fixed value of riometer absorption.

Rapidly changing densities in the ionosphere however can result in much less predictable behavior especially if the electric field is also changing. In the statistical model, this manifests as a decrease in the  $\text{ELF}/|\Delta H|$  proportionality constant during periods of high riometer absorption or high sporadic  $E$  critical frequency. During these periods of high absorption, changes in ELF intensity are smaller than changes in  $|\Delta H|$ . The theoretical model shows the same result and confirmed that the effect was due to denser ionosphere resulting in increases in ambient conductivity and  $|\Delta H|$  but smaller increases or decreases in HF modulated conductivities and ELF. Both the statistical and theoretical models predict similar changes in the  $\text{ELF}/|\Delta H|$

proportionality constant from a range of 0.01–0.005 pT/nT for the statistical model to a range of 0.024–0.016 pT/nT for the theoretical model.

The discrepancy between the values of the proportionality constant from the theoretical and statistical models is likely due to underestimation of the magnetometer measurement in the theoretical model. The ionospheric profiles from *McKinnell and Friedrich* (2007) stop near 140 km though currents above that altitude may still contribute to magnetic deviations on the ground. It is also possible that the statistical model is underestimating the proportionality constant at very low absorption values. In quiet cases where background conductivity is very low, but electric fields are changing substantially, ELF amplitude can change significantly despite little response in the electrojet and thus magnetometer. In such cases, it does not make sense to assign a proportionality constant between ELF amplitude and  $|\Delta H|$  as the two quantities are essentially uncorrelated and a neural network model tends to simply give an average value for the ELF output. If such a proportionality constant were to be assigned, it would approach infinity and a plot of ELF amplitude as a function of  $|\Delta H|$  (e.g. Figure 4.3c) would be a vertical line. These conditions are conducive to strong ELF generation despite little signature of an electrojet on magnetometers because of very low conductivity. Examples of such conditions can be found in *Kirkwood et al.* (1988), which also concludes that short intervals of strong electric fields can precede substorm onset by 2–20 minutes, a result consistent with the sudden increase in ELF intensity before substorm onset in Figure 3.11.

Results from the theoretical model may also explain negative correlation between magnetometer measurements and ELF generation. For example if the electron density (and ambient conductivity) increase substantially, but the electric field weakens slightly, the electrojet may intensify as the increased conductivity overcomes the reduced electric field while ELF generation weakens as the decreased electric field overcomes any gain in modulated conductivities. There are points in Figure 4.3a, including the second and third points, where for a fixed electric field, ELF intensity actually decreases when  $|\Delta H|$  increases, allowing for negative correlation if the ionosphere is changing in this region without any change in the electric field.

Radar measurements of electric field over HAARP would help complete our understanding of how ELF generation is affected by natural conditions. However, it may also be possible for ELF amplitude to be used in an inverse model to determine electric fields when the ionosphere is not significantly changing. ELF generation is reliable and sensitive to electric fields even when magnetometers do not detect any electrojet and riometers do not detect any absorption making it a potentially powerful diagnostic.

In summary, during disturbed conditions, the *E*-region electron density and conductivity increase resulting in a much stronger electrojet and higher  $|\Delta H|$ . Even if *D*-region density also increases, the gain in ELF intensity is much smaller. Increases in electric field which also contribute to the stronger electrojet are the larger factor in better ELF generation during increased geomagnetic activity.

## Chapter 5

# Harmonic Distortion and Modulation Waveforms

Statistics and simulations detailing the variation of ELF generation with natural conditions are one step in utilizing modulated ionospheric heating as a practical ELF source. Modulated heating differs from conventional ELF/VLF transmitters in another critical way however: the strong harmonics generated as a result of the nonlinear conversion of HF power to an ELF current. These harmonics consume bandwidth and can interfere with other signals in communications applications. Novel HF modulation waveforms may reduce generated harmonics compared to basic sine or square wave modulation. Besides harmonic distortion levels, the modulation waveforms also dictate the total ELF power as well as the conversion efficiency between the HF transmitter power and the radiated ELF power. Finding waveforms to optimize each of these metrics is another vital step towards using modulated heating for practical ELF generation.

To the author's knowledge, there has not been a published work that directly compares the harmonic content and received power of standard modulation waveforms such as sine wave and square wave of different duty cycles. There has also not been an attempt to use numerical modeling to create novel waveforms that have a particular property, such as minimizing generated harmonics. We describe herein a technique for using a numerical HF heating model to determine the waveform

required to induce a sinusoidal variation in the Hall conductivity at a particular altitude, essentially via predistortion. We show that the HF heating model can be adapted to compute these waveforms. Next we conduct simulations to verify that the waveforms are effective in reducing harmonic distortion and examine the sensitive dependence of the distortion performance to the assumed ambient ionospheric electron density profile. Finally, we present experimental results and compare the measured harmonic content of ELF waves generated using these waveforms to ones generated using traditional sinusoidal modulation and square wave modulation of varying duty cycles. In addition to harmonic content, we also compare the received power and efficiency of each modulation waveform.

## 5.1 Background

Two basic forms of amplitude modulation used in heating experiments are square wave (beam is switched between full power and zero power) and sinusoidal modulation (HF amplitude varies sinusoidally). Square modulation waveforms can also have variable duty cycles, that is, variable percentages of an ELF period that the HF beam is turned on. *Cohen* (2009, Ap. E) examined the harmonic content when an HF beam is modulated with a square wave over a range of duty cycles. A 40% duty cycle resulted in the highest received fundamental amplitude because the time constant for electron heating is faster than that for cooling. The HF beam needs to be on only long enough for the electron temperature to reach saturation. Leaving the beam off for a slightly longer time allows the electrons more time to cool to their ambient temperature. The smallest duty cycle used (15%) was the most efficient in the fundamental, where efficiency is defined as the fundamental amplitude divided by the duty cycle.

Sinusoidal modulation, though it should not have any inherent harmonic content, can still result in substantial harmonic generation. For example, *Oikarinen et al.* (1997) showed significant harmonic content of a 1375 Hz signal generated with sinusoidal modulation. *Pashin and Lyatsky* (1997) presents simulated values of the second and third harmonic ratios of the height integrated conductivity for sinusoidal modulation as a function of ERP at modulation frequencies below 100 Hz and at

1375 Hz. The results depended on HF power, but the second harmonic of the Hall conductivity is sometimes only 10 dB below the fundamental at frequencies below 100 Hz and 20 dB below at 1375 Hz. The third harmonic ratios were roughly  $-25$  dB and  $-30$  dB respectively. *Moore et al.* (2006) conducted experiments at HAARP using a sinusoidally modulated 3.25 MHz beam and examined the amplitudes of the fundamental, second, and third harmonics as a function of ELF frequency as well as HF power (up to 771 kW). The second harmonic was typically  $\sim 8$  dB below the fundamental with the third harmonic  $>15$  dB below depending on the HF power. Numerical heating models also agreed with those experimental results.

## 5.2 Methodology

The HF heating model described in Chapter 2 is used to compute the change in the ionospheric conductivity over a range of altitudes when the ionosphere is heated with a given HF power envelope. In order to reverse the nonlinear conversion between HF power and conductivity and minimize radiated harmonics, we reverse the model. We begin with the condition that the Hall conductivity be sinusoidally varying at some altitude and determine the HF power modulation needed at the base of the ionosphere to obtain that waveform by running the forward model in reverse. We choose to make the Hall conductivity sinusoidal since previous studies showed that the Hall currents contribute more to the ELF source currents than the Pedersen currents (*Barr and Stubbe*, 1984; *Cohen et al.*, 2008). Since the ionospheric parameters change with altitude, the Hall conductivity can only be sinusoidal at a specified altitude. Equation 2.8 can be inverted numerically or by a lookup table to obtain  $\nu_{\text{eff}}$ . From there,  $T_e$  and  $\frac{dT_e}{dt}$  can be calculated from Equations 2.11 and 2.12 and  $S$  can be determined from Equation 2.2.  $S$  is now the power waveform that must reach the plasma in order for the modified Hall conductivity to be sinusoidal. The amplitude of the specified sinusoid is determined by using the HF heating equations in the forward direction to determine the conductivity difference induced in the plasma at a particular altitude when heated by a full power beam. If, after inversion, the power density needed to achieve that sinusoidal conductivity variation is non-physical

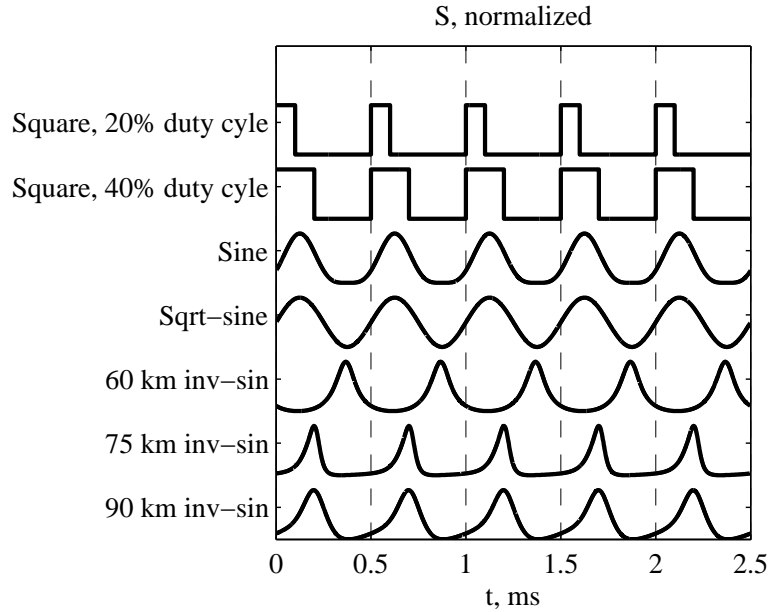


Figure 5.1: Examples of HF power transmission waveforms including square wave at two duty cycles, sine, sqrt-sine, and three inv-sin waveforms designed to minimize harmonics at 60, 75, and 90 km.

(greater than the power that can reach that altitude or negative), then the amplitude of the specified conductivity is iteratively reduced until the power density is valid. Finally, the absorption and spreading losses from propagation through the ionosphere are reversed by integrating the absorption downward from the target altitude and undoing the  $1/r^2$  spreading. The resulting power waveform is then used to modulate the HF power of the HAARP array.

These waveforms are referred to herein as inverse-sine (inv-sin) waveforms. A waveform designed to induce a sinusoidal variation in the Hall conductivity at 75 km, for example, is referred to as a 75 km inv-sin waveform. Intuitively, the waveform should minimize harmonic distortion at the altitude that experiences the most conductivity modulation. This altitude depends significantly on ionospheric density with higher densities corresponding to a lower altitude of peak modulation (*Barr and Stubbe, 1984; Payne, 2007; Jin et al., 2011*). To increase the chances of reducing generated harmonics overall, we generate multiple inv-sin waveforms, each

optimized for a different altitude. Figure 5.1 shows an example of three of these inv-sin waveforms, optimized for 60, 75, and 90 km. Also included for comparison are square waves with duty cycles of 20% and 40%, as well as sinusoidal waveforms. In these experiments, sinusoidal modulation refers to a sinusoidal HF amplitude, in which case the HF power ( $S$  in Equation 2.2) actually varies as sin-squared. Square-root of sine (sqrt-sin) modulation results in a sinusoidal HF power. We note that past studies have found that generated ELF amplitude scales with HF power, not HF amplitude. The inv-sin waveforms have narrower peaks, where the beam is on for a shorter time compared to sinusoidal modulation. The narrower peaks effectively compensate for the discrepancy in the heating and cooling time constants in the ionosphere in the same way smaller duty cycles did for square wave modulation in *Cohen* (2009, Ap. E).

### 5.3 Numerical Modeling

To verify that the resulting HF power transmission waveforms do reduce or eliminate generated harmonic content, the inv-sin waveforms are run back through the forward model. The harmonic content of the resulting change in the Hall conductivity,  $\Delta\sigma_H$  is examined and compared to sinusoidal modulation to verify that the inv-sin waveforms are suppressing harmonics as they were designed to.

First, we generate seven inv-sin waveforms optimized for altitudes from 60 to 90 km in 5 km increments using an electron density profile from the International Reference Ionosphere above 82 km and extrapolate at lower altitudes with an exponentially decaying density. This profile closely approximates an ionosphere given by *Wait and Spies* (1964) with parameters  $h' = 84$  km and  $\beta = 0.5$  km<sup>-1</sup> and is typical of a quiet nighttime ionosphere. The inv-sin waveforms are then simulated with the HF heating model in the forward direction under the same ionosphere and the results compared with sinusoidal modulation.

Figure 5.2 shows the results of running an inv-sin waveform back through the forward model. Panel (a) shows how the conductivity variation changes with altitude, where it becomes sinusoidal at 75 km as expected but is distorted at other altitudes.



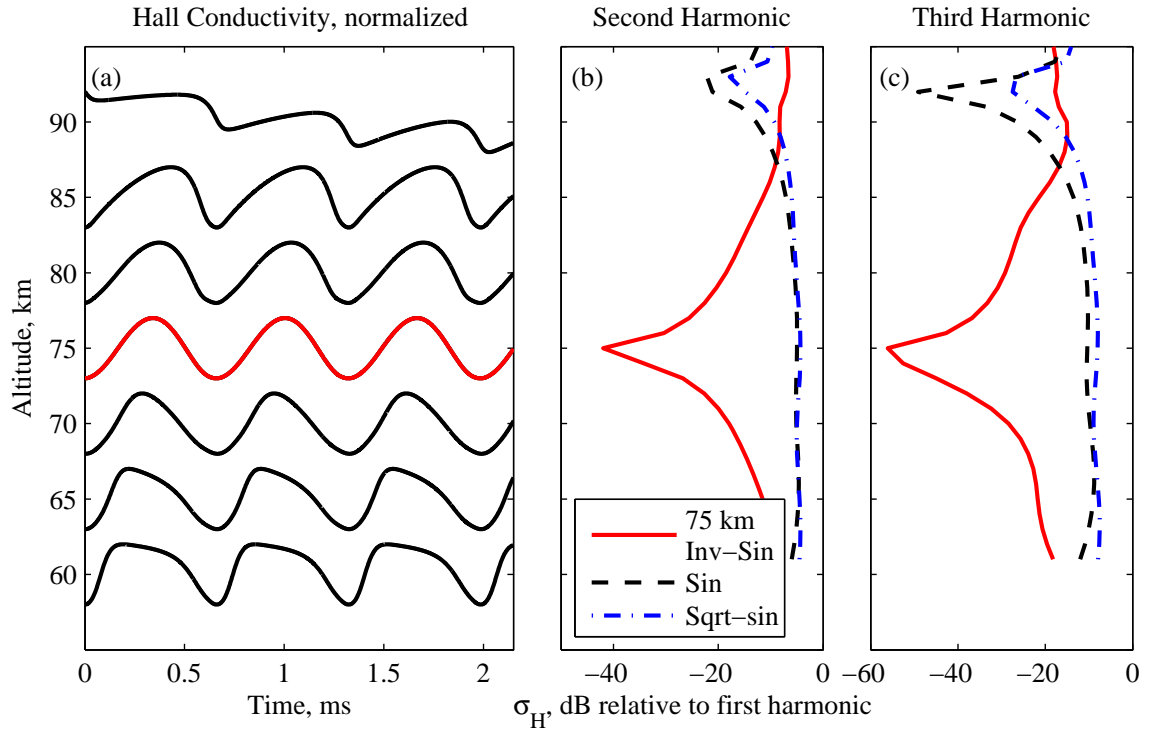


Figure 5.2: Simulated Hall conductivity at several altitudes from 60 to 90 km when using a 75 km inv-sin waveform (a). Hall conductivity is sinusoidal at 75 km but not at other altitudes. Second (b) and third (c) harmonics of the modified Hall conductivity as a function of altitude in dB relative to the first harmonic. Harmonics at 75 km are suppressed substantially compared to sin and sqrt-sin modulation. Sqrt-sin has greater harmonic distortion compared to sin wave modulation.

Panels (b) and (c) show the second and third harmonic of the modified Hall conductivity for three different modulation waveforms. The 75 km inv-sin waveform was designed to minimize harmonic distortion at an altitude of 75 km and does in fact show a null at that altitude. The second harmonic is  $\sim 40$  dB below the fundamental and the third harmonic is  $\sim 56$  dB below the fundamental. Sin and sqrt-sin modulation show more distortion with the second and third harmonic only  $\sim 5$ – $10$  dB below the fundamental below 85 km with a minimum in distortion between 92–93 km. Note that sqrt-sin modulation has higher harmonic content than sinusoidal modulation over almost all altitudes.

However, inversion of the numerical HF heating model to create the inv-sin waveforms assumes knowledge of the ionospheric electron and neutral density profile as well as an ambient temperature profile. If the resulting waveforms are used when the actual ionosphere has a different profile from the one assumed, then the harmonic content of the ELF waves may be higher than expected. To examine the effect of an electron density profile that differs from the assumed one, we simulate waveforms generated using the assumed profile with electron density profiles different from the assumed profile. To create a family of electron density profiles for simulation, we use a simple two parameter model for ionospheric electron density (*Wait and Spies, 1964*). This model represents an electron density that changes exponentially with altitude and is parameterized by  $h'$ , an effective altitude, and  $\beta$ , a steepness parameter. The assumed electron density profile is one with  $h' = 84$  km and  $\beta = 0.5$  km $^{-1}$  and is used to generate inv-sin waveforms. These waveforms are then simulated on 20 electron density profiles with  $h'$  values of 72, 78, 84, and 90 km, and  $\beta$  values of 0.3, 0.4, 0.5, 0.6, and 0.7 km $^{-1}$ . We examine the harmonic content produced when the inv-sin waveforms are used for each of the 20 different ionospheres to examine how closely  $h'$  and  $\beta$  need to be to the assumed values in order for harmonic distortion to be suppressed relative to sinusoidal modulation.

The results are given in Table 5.1, which shows the ratio of the amplitude of the 2nd harmonic of the Hall conductivity at 90 km to the amplitude of the fundamental for a 90 km inv-sin waveform. This ratio is low ( $-31.8$  dB) for a matching ionosphere ( $h' = 84$  km,  $\beta = 0.5$  km $^{-1}$ ) as expected, but also remains below  $-20$  dB for other

| h', km    | $\beta, \text{km}^{-1}$ |       |              |       |       |
|-----------|-------------------------|-------|--------------|-------|-------|
|           | 0.3                     | 0.4   | <b>0.5</b>   | 0.6   | 0.7   |
| 72        | -9.3                    | -6.0  | -6.0         | -6.0  | -6.0  |
| 78        | -11.4                   | -16.1 | -15.9        | -6.0  | -6.0  |
| <b>84</b> | -29.4                   | -35.9 | <b>-31.8</b> | -20.6 | -15.2 |
| 90        | -18.5                   | -18.1 | -17.9        | -17.8 | -17.7 |

Table 5.1: Second harmonic of the Hall conductivity at 90 km expressed in dB relative to the first harmonic from simulations using a 90 km inv-sin waveform created assuming an ionospheric electron density expressed with  $h' = 84$  km and  $\beta = 0.5 \text{ km}^{-1}$ .

| h', km | $\beta, \text{km}^{-1}$ |       |       |       |       |
|--------|-------------------------|-------|-------|-------|-------|
|        | 0.3                     | 0.4   | 0.5   | 0.6   | 0.7   |
| 72     | -2.8                    | -6.0  | -6.0  | -6.0  | -6.0  |
| 78     | -24.5                   | -25.2 | -23.9 | -6.0  | -6.0  |
| 84     | -9.1                    | -9.4  | -10.0 | -11.2 | -14.2 |
| 90     | -7.9                    | -7.8  | -7.7  | -7.7  | -7.7  |

Table 5.2: Second harmonic of the Hall conductivity at 90 km expressed in dB relative to the first harmonic from simulations using a sinusoidal waveform. Distortion is generally lower than 90 km inv-sin for  $h'$  below 84 km and greater for  $h'$  of 84 km and above.

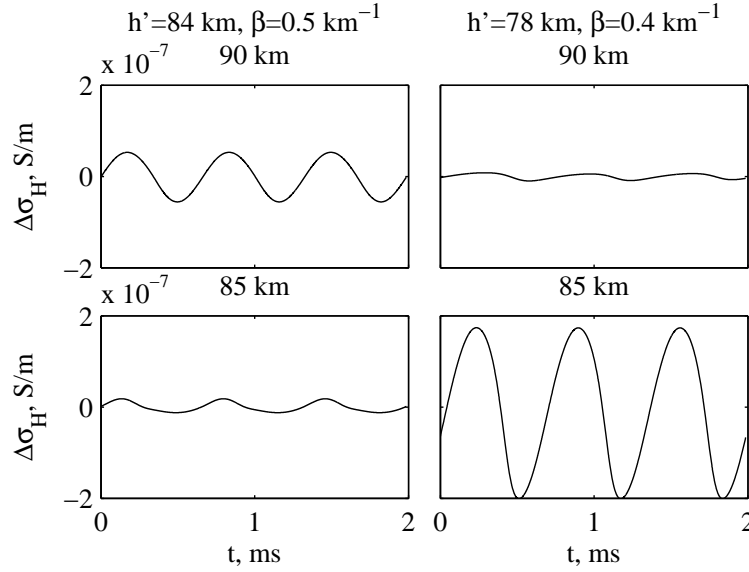


Figure 5.3: Simulated change in Hall conductivity when using a 90 km inv-sin waveform assuming an ionosphere modeled by  $h' = 84$  km and  $\beta = 0.5$  km $^{-1}$ . Plots on the left show the conductivity at 90 and 85 km with a matching ionosphere where the conductivity at 90 km is distortion free. Plots on the right show the conductivity at 90 and 85 km with a mismatched ionosphere. Most of the HF power has been absorbed at lower altitudes and the modulation at 90 km is much weaker and more distorted.

values of  $\beta$  except  $0.7$  km $^{-1}$ . As long as  $h'$  is 84 or 90 km, the second harmonic remains at least  $-15$  dB below the fundamental. There is also less distortion at 90 km altitude than with sinusoidal modulation (Table 5.2). However, for smaller values of  $h'$ , the second harmonic ratio increases to between  $-16$  dB to above  $-10$  dB for inv-sin modulation. Sinusoidal modulation generally has less distortion than 90 km inv-sin modulation when  $h'$  is below 84 km, with the second harmonic roughly 24 dB below the fundamental for  $h' = 78$  km and  $\beta$  between  $0.3$  and  $0.5$  km $^{-1}$ . The harmonic content is not particularly sensitive to  $\beta$  for either modulation waveform as values between  $0.3$  and  $0.5$  km $^{-1}$  do not affect the harmonic content appreciably.

Figure 5.3 shows an example of the simulated Hall conductivity when a 90 km inv-sin waveform designed for a specific value of  $h'$  is applied to an ionosphere for

which the actual value of  $h'$  is smaller. The plots on the left side show the change in Hall conductivity at 90 km and 85 km for the expected  $h' = 84$  km,  $\beta = 0.5 \text{ km}^{-1}$  ionosphere. At 90 km the conductivity appears sinusoidal and distortion free. However, the plots on the right side, which show the conductivity when  $h' = 78$  km,  $\beta = 0.4 \text{ km}^{-1}$ , are notably distorted. Because the ionosphere on the right hand side is more dense at lower altitudes, much of the absorption happens near 85 km and the amplitude of the conductivity at 85 km is greater than for the less dense ionosphere. Thus, less power is available at 90 km, which therefore has a much smaller change in conductivity. The electron density itself does not affect the heating and cooling time constants (*Cohen*, 2009, pg. 45), but the assumptions inherent in calculating the inv-sin waveform are that a certain power density is absorbed before reaching 90 km, which if not correct, result in a distorted conductivity change at that altitude.

## 5.4 Experimental Results

### 5.4.1 Harmonic Minimization

The inv-sin waveforms were transmitted as part of an experiment conducted at HAARP from July 22–26, 2011 for a total of 3 hours of transmission time. The 1-minute format consists of 20 seconds at ELF frequencies of 510, 1510, and 2125 Hz. For each frequency, 10 amplitude modulation waveforms were transmitted for 2 seconds each. These were: square wave with 40% duty cycle, sinusoidal HF amplitude (power varies as sine squared), sqrt-sine HF amplitude (sinusoidal HF power), and seven inv-sin formats optimized for altitudes from 60–90 km in 5 km increments. The assumed ionospheric density profile was taken from the International Reference Ionosphere above 82 km and extrapolated to lower altitudes assuming an exponential decay. This is the same standard nighttime profile from Section 5.3. A full power 2.75 MHz, X-mode HF beam was used for the entire experiment.

ELF measurements were made with the Stanford AWESOME receiver (*Cohen et al.*, 2010c) located at Chistochina, Alaska, 37 km northeast of HAARP. Signals from two

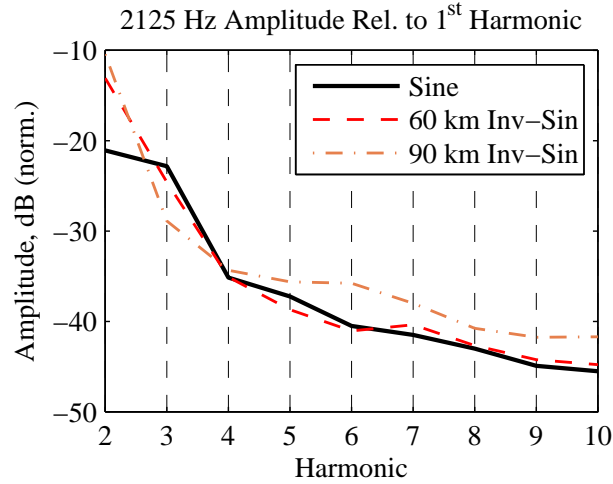


Figure 5.4: Harmonic content of ELF signals received in Chistochina, Alaska for 2125 Hz signals generated using sine wave modulation (black), and 60 km and 90 km inv-sin modulation (red and orange). Amplitudes are in dB relative to the fundamental. The inv-sin waveforms do not have substantially lower harmonic content compared to sine wave.

orthogonal loop antennas are sampled at 100 kHz and digitized with 16 bits of resolution and  $<200$  ns timing error. ELF amplitudes at the carrier and harmonic frequencies are extracted from a Fast Fourier Transform of the data and amplitudes from the two antennas are combined to obtain the total horizontal component of the wave magnetic field.

Signal intensities were strongest during transmissions on July 23 from 0906–0936 UT. The results in Figure 5.4 show the amplitude of each harmonic up to the 10th, relative to the fundamental, for 60 and 90 km inv-sin, as well as sinusoidal modulation. The 60 and 90 km inv-sin waveforms performed the best of the inv-sin waveforms but still did not result in lower harmonic content of the received ELF waves when compared to sinusoidal modulation. The second harmonic was over 20 dB below the fundamental for sinusoidal modulation but only 10–13 dB below for the inv-sin waveforms. In the third harmonic, 90 km inv-sin does show a substantial improvement over sine wave (–29 dB versus –23 dB). In the higher harmonics, 60 km inv-sin and sine perform similarly with 90 km inv-sin being  $\sim 3$  dB worse. The higher amplitude of

the harmonics for the inv-sin waveforms suggests that the ionospheric density profile on the day of the experiment did not match the profile assumed when generating the inv-sin waveform.

### 5.4.2 Total Power and Efficiency

In addition to examining the relative amplitudes of the harmonics, we also compare the power in the fundamental as well as the total power including harmonics for different modulation waveforms. Since different waveforms require different amounts of power to transmit we also compare the efficiency of various waveforms and define efficiency as the ratio of the received power to the power in the waveform. The power in the HF amplitude waveform  $x(t)$  is defined as:

$$\frac{1}{T} \int_0^T x^2(t) dt$$

where  $T$  is the ELF fundamental period. Experimental data for inv-sin waveforms were taken from the same experiment as above. In addition a separate experiment using square-wave modulation with duty cycles from 15 to 85% in 5% increments was also performed from October 2, 5, 9, and 13, 2010 with the strongest generation from 0830–0900 UT on October 13. For this experiment data were taken from an AWESOME receiver near Paxson, Alaska roughly 50 km north of HAARP.

In the duty-cycle experiment, 1 second tones at frequencies of 510, 990, 1530, 2010, 3030, and 5010 Hz are transmitted at each of 15 different duty cycles. This sequence is repeated using 100%, 50%, 25%, and 12.5% power. The entire format thus repeats every 6 minutes. We consider only a full-power beam modulated at 2010 Hz and compare the received signal to the results from the inv-sin experiment at 2125 Hz. Both the inv-sin and duty cycle experiments contain a tone using square-wave modulation with a 40% duty cycle. Thus, to compare modulation waveforms across both experiments and to normalize for different natural conditions, received power is always reported as relative to the received power when 40% duty cycle square wave modulation is used. For example, sine wave modulation has a total received power of 0.55, meaning the average measured power across all harmonics is 55% of the average

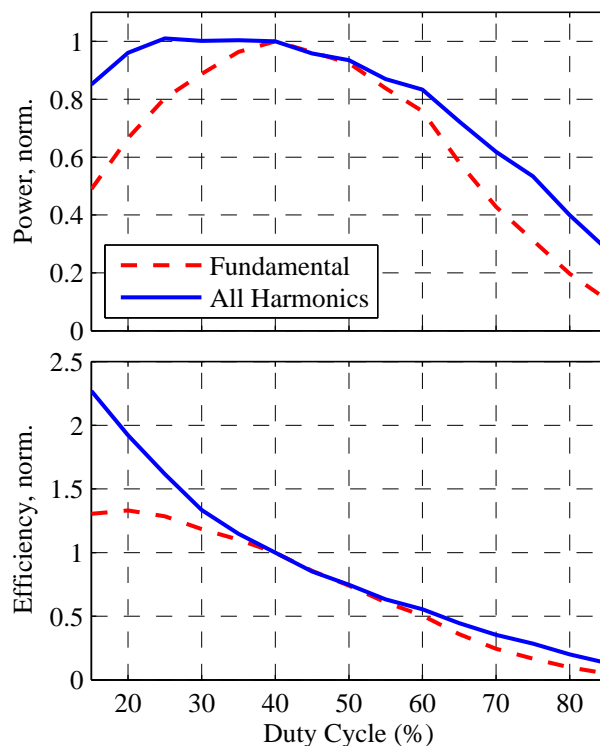


Figure 5.5: Received power and efficiency for 2010 Hz signals generated using square wave modulation of different duty cycles and received at Paxson, Alaska. Red line only includes received power in the fundamental; blue line includes received power in the first five harmonics. All values are normalized so that 40% duty cycle has a value of 1. A 40% duty cycle yielded the most power in the fundamental, while duty cycles between 25-40% have the most total power. Total power efficiency increases for lower duty cycles and fundamental efficiency peaks at 20% duty cycle.



| Waveform      | Input Power | Fundamental |            | All Harmonics |            | Fraction in Fundamental |
|---------------|-------------|-------------|------------|---------------|------------|-------------------------|
|               |             | Power       | Efficiency | Power         | Efficiency |                         |
| 40% Square    | 0.40        | 1           | 1          | 1             | 1          | 0.85                    |
| 20% Square    | 0.20        | 0.67        | 1.33       | 0.96          | 1.92       | 0.59                    |
| Sine          | 0.375       | 0.65        | 0.70       | 0.55          | 0.58       | 0.987                   |
| 60 km Inv-Sin | 0.27        | 0.55        | 0.81       | 0.48          | 0.71       | 0.948                   |
| Sqrt-Sin      | 0.50        | 0.40        | 0.32       | 0.37          | 0.30       | 0.902                   |

Table 5.3: Experimental data for 5 different waveforms including power in waveform, received fundamental power and efficiency, received total power and efficiency, and fraction of received power in the fundamental. Received power and efficiency are referenced against 40% square wave. 40% square wave has the highest received power, 20% square wave has the highest efficiency, and sine wave has the lowest harmonic distortion. 60 km inv-sin has slightly higher distortion than sine wave but is more efficient. Sqrt-sin is worse than sine in every metric.

measured power across all harmonics when 40% duty cycle square wave modulation was used. Similarly, a fundamental power of 0.81 for sine wave modulation means that the average received power in the fundamental is 81% of the average received power in the fundamental with square wave modulation. Efficiency is also normalized in the same way. Figure 5.5 shows the variation of fundamental and total received power and efficiency as a function of duty cycle. Peak power in the fundamental occurs with a duty cycle of 40% and drops rapidly for other duty cycles. When considering all harmonics, there is a broader maximum in received power with duty cycles from 25–40%. Thus, total efficiency is highest for the smallest duty cycle used (15%) since the received power only decreases slightly (about 85% of the highest total power) while the power needed to transmit the waveform decreases. However, when considering only the fundamental, the efficiency peaks at 20% duty cycle. These results are very similar to the ones in *Cohen* (2009, Appendix E), which also showed a peak in the fundamental power near a 40% duty cycle but a peak in fundamental efficiency at 15% duty cycle in measurements at Chistochina, Alaska.

The results of the duty-cycle and inv-sin experiments are summarized in Table 5.3. Square wave modulation with duty cycles below 40% generally produce the strongest ELF waves and have high efficiency. Received signals are strongest for a duty cycle

of 40%, regardless of whether only the fundamental or all harmonics are considered. A duty cycle of 20% resulted in the highest efficiency in the sense of highest received fundamental power relative to the total input power. Although the lower duty cycle generates only 0.67 times the power in the fundamental as for a 40% duty cycle, it only requires half the power to transmit, resulting in a 1.33 times increase in efficiency.

Variants of sinusoidal modulation all had lower levels of harmonic distortion (indicated by a greater percentage of the total power contained in the fundamental), than square wave modulation. Of these variations, sinusoidal modulation had the smallest level of harmonic distortion, with 98.7% of the power in the fundamental. The 60 km inv-sin waveform had slightly higher distortion with 94.8% of the power in the fundamental but is also more efficient than sine wave (0.81 versus 0.70 for the fundamental power). Sqrt-sine, which results in a sinusoidally varying HF power, performs worse in all respects compared to sinusoidal modulation.

## 5.5 Heating and Cooling Time Constants

Generally, the time constants for heating of the electrons by absorption of HF wave energy are faster than for cooling by collisions with neutral molecules. This discrepancy can explain several of the features we observed in our experiments with different modulation waveforms. First, any attempt to create an HF power waveform that produces a sinusoidal conductivity variation must compensate for the asymmetry in the heating and cooling time constants. Thus it makes sense that the inv-sin waveforms in Figure 5.1 have a slower rise time and faster fall time, which helps to decrease the heating and increase the cooling time constant so that the two are balanced. This behavior is most apparent for the 75 km inv-sin waveform where the fall time is especially fast compared to the rise time. Note that the 60 km and 90 km inv-sin waveforms more closely approximate a sine wave. At lower altitudes, the neutral density is much higher so the electrons cool more rapidly, and the heating and cooling time constants are better balanced. As the altitude increases, the cooling rate decreases. However, at very high altitudes, most of the HF power has been absorbed and both the heating and cooling rates have decreased substantially and are again

more balanced. This balancing effect may explain why the 60 and 90 km inv-sin waveforms generated less distortion in experiments than the intermediate altitude inv-sin waveforms as 60 and 90 km inv-sin are the most symmetric and most closely resemble a sinusoid. Because sinusoidal modulation already creates little harmonic distortion near 92 km (Figure 5.2b and c), it may well be that it is already near optimal for minimizing harmonics at that altitude.

However all the inv-sin waveforms also take less power to transmit because the power is high for a shorter fraction of an ELF period. For example, 60 km inv-sin has an effective duty cycle of 27% compared to 37.5% for sine wave. The heating only needs to occur for a short period for the electron temperature to increase to saturation since the heating time constant is fast. Once the electron temperature is near saturation, the HF power can be reduced rapidly, allowing more time for the temperature to recover to its ambient value with the slower cooling time constant. This effect explains why square waves with smaller duty cycles generate stronger ELF waves than ones with higher duty cycles. A 40% duty cycle square wave generated the strongest ELF waves in the fundamental, and smaller duty cycles result in only a small decrease in received power. Duty cycles larger than 40% generate less power and are much less efficient because they result in longer heating and shorter cooling periods, which heat the electrons to saturation but do not allow them to cool very much before the next heating period begins.

This preference for smaller duty cycles also explains why sqrt-sin modulation is worse than sinusoidal modulation in all respects. Sinusoidal modulation means the HF power is proportional to sin squared, which has a lower effective duty cycle than sin (more time at low power than at high power). It may be interesting in future experiments to try waveforms represented by an HF amplitude of  $\sin^k(2\pi ft)$  where  $k$  is some number greater than 0.5. Higher values of  $k$  produce smaller effective duty cycles, which may improve efficiency while still maintaining low values of harmonic distortion compared to square wave. These waveforms would also be easier to implement than the inv-sin waveforms.

## 5.6 Summary

Generation of ELF waves using amplitude modulation of an HF beam results in harmonic distortion due to the nonlinear relationship between HF power and conductivity change in the ionosphere. With a sinusoidal amplitude envelope, 98.7% of the received ELF power is in the fundamental. A sinusoidal power envelope has worse distortion with only 90.2% of the power in the fundamental. To minimize the harmonic distortion we used numerical models to compute a non-sinusoidal HF envelope that would result in a sinusoidal Hall conductivity at a given altitude. In simulation the inv-sin waveforms do minimize harmonic distortion at a specific altitude but are sensitive to ionospheric electron density profiles. The inv-sin waveforms generally perform as intended when the actual ionosphere has a similar or greater value of  $h'$  as the one assumed when generating the waveforms. Otherwise, the inv-sin waveform may result in greater harmonic distortion than sinusoidal modulation. This result was obtained in experiments where the 60 km inv-sin waveform produced the least distortion of all the inv-sin waveforms but still resulted in only 94.8% of the received power in the fundamental.

However, the choice of waveform also affects the received power of the ELF wave. Square wave modulation, though it results in more harmonic distortion (85% of power in the fundamental for a 40% duty cycle) is often used because it generates the most absolute power in the fundamental. Smaller duty cycles trade off a small decrease in received power for a larger savings in the average power needed to transmit the waveform. A duty cycle of 20% was most efficient in the sense of maximizing the received power in the fundamental versus the power needed to transmit. When we consider the power in all the harmonics, even smaller duty cycles are more efficient. Although the inv-sin waveforms resulted in more harmonic distortion than sinusoidal modulation, they require less power to transmit and are more efficient while still having reasonably low levels of distortion. In general, there appears to be a tradeoff between harmonic distortion and efficiency when choosing waveforms.

## Chapter 6

# ELF Communications with Modulated Heating

Throughout this thesis, we emphasized two differences between modulated ionospheric heating and conventional ELF/VLF transmitters: the strong dependence on natural conditions and nonlinear distortion leading to the generation of harmonics. It is now time to see how these differences are relevant in a practical application of ELF transmitters: digital communications.

Past studies summarized in Section 1.1 have thoroughly addressed the challenges of impulsive noise, which affects the reception of ELF waves generated by both large antennas and modulated ionospheric heating. However, no studies have addressed the implications of the strong non-linearity inherent with modulated heating on communications. Because much of the signal energy lies in the harmonics ( $>15\%$ , depending on the type of modulation), it is important to consider how that energy can be used to improve the performance the system. Such a study can be challenging because the characteristics of the ELF/VLF noise environment change with frequency. Figure 6.1 shows a spectrogram of ELF transmissions from HAARP. The fundamental is at 1510 Hz, and there are several harmonics visible. The noise environment below  $\sim 4.5$  kHz appears mostly Gaussian, with occasional impulses from nearby lightning strikes. However, the fourth and higher harmonics are exposed to a much more impulsive environment with many sferics. At higher frequencies, sferics can propagate

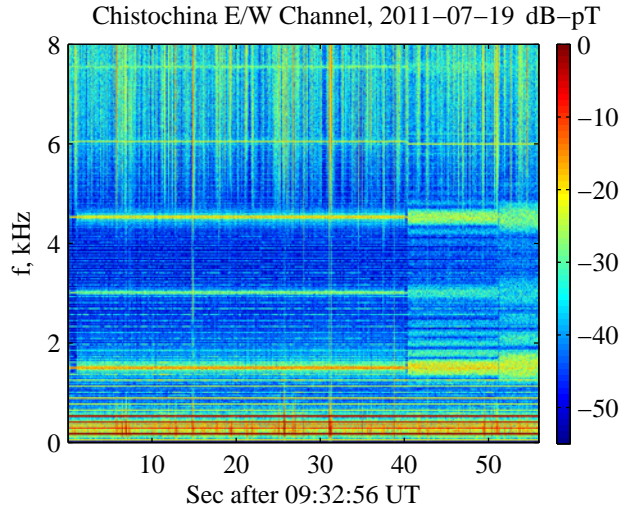


Figure 6.1: Spectrogram showing transmission of 3 packets using square wave modulation at 1510 Hz at bit rates of 100, 400, and 800 bps. Higher bitrates use more bandwidth. Harmonics are clearly visible at integer multiples of 1510 Hz.

in waveguide modes with less attenuation (e.g., *Budden*, 1961, pg. 34), and sferics propagating over very long distances in the Earth-ionosphere waveguide contribute to the higher noise levels.

We examine the results of experiments to transmit digital data using quaternary phase shift keying (QPSK, described below) on an ELF carrier generated via modulated ionospheric heating at HAARP. We show the measured bit error rates (BER) as a function of signal-to-noise ratio at several bit rates and ELF frequencies. We then examine whether the use of more of the harmonic content of the signal can improve the BER because of the higher signal strength available from the energy in the harmonics. We then present results from computer simulations of the encoding, noise addition, and decoding process, which provide more reliable measurements of the BER since these simulations can be repeated as often as necessary, whereas experimental time at the HAARP transmitter is limited. Finally we compare the experimental and simulation results with mathematical models from previous works to better characterize the BER of a communications system using a ELF carrier with many harmonics in an impulsive ELF noise environment.

## 6.1 Phase Shift Keying

The modulation technique used in this paper is quaternary phase shift keying (QPSK) or 4-PSK. Digital data is divided into pairs of bits, which are either 00, 01, 11, or 10. To transmit the bits 00, a symbol, such as a sinusoid of fixed duration is used. The other bit pairs are represented with a sinusoid phase shifted at 90, 180, and 270 degrees relative to the symbol representing 00. The symbol does not necessarily need to be a sinusoid, as modulated heating experiments have shown that other types of heating waveforms such as square waves are more efficient in generating ELF waves (*Jin et al.*, 2012). Non-sinusoidal waveforms have harmonic content that increases the bandwidth used by the transmission. However, even sinusoidal modulation generates harmonic content due to the nonlinear conversion between the HF power waveform and changes in the plasma conductivity. Thus, it may be advantageous to use square waves as the QPSK symbol to take advantage of the greater generated power at the expense of an increase in harmonic content. In this case, the symbols representing 01, 11, and 10 are circularly shifted by a quarter, a half, and three quarters of a fundamental ELF period relative to the symbol representing 00. At the fundamental frequency, the four symbols still have phase shifts of 0, 90, 180, and 270 degrees. The phase shifts at the higher harmonics are integer multiples of the phase shifts in the fundamental (e.g. 0, 180, 0, and 180 degrees in the second harmonic). Thus evenly spacing the phases of the four symbols in the fundamental may not be optimal because phase shifts in the higher harmonics may overlap. In principle different phases can be chosen to maximize the “distance” between the 4 symbols, although such a scheme requires knowledge of the harmonic content at the receiver, which changes due to natural conditions and as the ELF waves propagate through the Earth-ionosphere waveguide.

Fortunately, the optimal receiver implementation is independent of the choice of the 4 symbols used by the transmitter. If the noise introduced in the signal is additive White Gaussian noise (AWGN) then the optimal receiver (the one that minimizes the probability of an error) is a matched filter receiver. The correlation receiver is an equivalent implementation and functions by computing the correlation between

each received symbol and each of the four possible symbols. The symbol with the highest correlation is deemed to be the one most likely to have been transmitted. The probability that a received bit is different than a transmitted bit is the bit error rate (BER) and is only a function of the total energy in a symbol,  $E_s$ , and the noise power spectral density,  $N_0$ , which is constant over frequency for AWGN. Total energy,  $E_s$ , depends on the amplitude of the generated ELF signals, which changes dramatically with natural conditions (*Jin et al.*, 2009) as well as the duration of the symbol. Doubling the duration of the symbol period doubles  $E_s$  at the expense of halving the transmission rate. For QPSK in AWGN, the BER has been shown to be equal to  $Q(\sqrt{2E_b/N_0})$ , where  $E_b$  is the energy per bit ( $E_s/2$  for QPSK), and the  $Q$  function is the tail probability of the normal distribution. However, the actual ELF noise environment is substantially different from an AWGN model. Radio atmospherics (sferics) from lightning strikes are the dominant source of natural noise and have an impulsive character. Nonetheless, we continue to use a standard correlation receiver in this work as it does simplify the analysis. However, experimental and simulated data are passed through a whitening filter before further processing. This filter attempts to level the power spectral density in the signal so that the average noise level throughout the frequency range from  $\sim 1$ –10 kHz may be roughly the same. This procedure at least emulates the “white” aspect of AWGN for which the correlation receiver is optimal, though the impulsive non-Gaussian aspect does remain.

## 6.2 Experimental Summary

The digital data transmitted using modulated HF ionospheric heating at HAARP consists of the string “Stanford VLF” followed by a line feed (new line) encoded in 8-bit ASCII with no parity. The remainder of the data consists of random bits. Three different bit rates are used. The 100 bps transmission lasts a total of 40 seconds and consists of a total of 486 bytes of data. The 400 bps transmission lasts for 11 seconds and contains 536 bytes. The 800 bps transmission lasts for 5 seconds and contains 486 bytes of data. In addition to the data, each transmission contains a header including a 13-bit BPSK modulated sequence to aid in timing synchronization, as well as an



equalization sequence consisting of 80 consecutive 0 bits to establish a phase reference. Together, the header and the data form a packet. Each packet is transmitted at ELF frequencies of 1510, 2125, and 2735 Hz, first with sinusoidal and then with square wave modulation.

The transmissions are received at a site in Chistochina, Alaska, 37 km northeast of HAARP using a Stanford AWESOME receiver (*Cohen et al.*, 2010c). Signals from two orthogonal loop antennas are sampled at 100 kHz and digitized with 16 bits of resolution. A GPS disciplined oscillator allows sampling with  $<200$  ns timing error. For these experiments, only signals from the magnetic east-west oriented antenna are used. After the experiment, the digitized data are processed with a software decoder implemented in MATLAB.

To decode the transmissions, the equalization sequence is analyzed by taking a Fast Fourier Transform (FFT) of the entire sequence and extracting the coefficients corresponding to the fundamental ELF frequency as well as four additional harmonics. The transmission can be decoded with fewer harmonics or only the fundamental, in which case only the FFT coefficients corresponding to the desired frequencies are kept. The inverse FFT of the equalization sequence is taken to obtain a time domain waveform that corresponds to the symbol 00. The waveform is then shifted by a quarter of a period, half a period, and three quarters of a period to obtain the waveform corresponding to the other symbols. The rest of the receiver is implemented as a correlation receiver, where the correlation between the waveform corresponding to a data symbol and each of the four waveforms derived from the equalization sequence is computed. The one with the highest correlation corresponds to the symbol received. After decoding, the received bits are compared to the bits actually transmitted. The number of erroneous bits divided by the number of bits received is the bit error rate (BER).

The signal energy  $E_b$  is also computed and only includes the energy in the harmonics actually used to decode the transmission. For example, if only three harmonics are used to decode the transmission,  $E_b$  includes only the energy contained in the first three harmonics. Here, the first harmonic is synonymous with the fundamental.  $N_0$  is always determined as the average power spectral density between 1.5–4.0 kHz, where

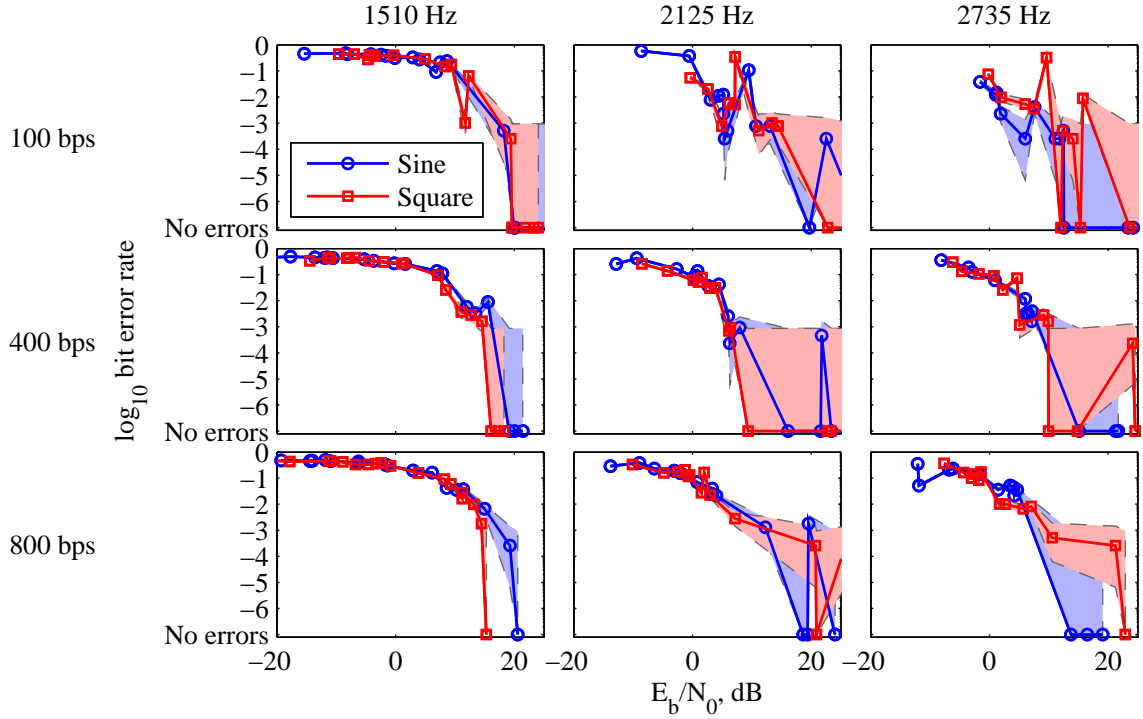


Figure 6.2: Bit error rate as a function of  $E_b/N_0$  for ELF frequencies of 1510, 2125, and 2735 Hz and bit rates of 100, 400, and 800 bps when decoding using only the fundamental. Square wave modulation, higher frequencies, and lower bit rates generally result in higher values of  $E_b/N_0$ , but the curves are otherwise similar.

the noise is primarily gaussian and the power spectral density is reasonably flat. For consistency,  $N_0$  is determined with this frequency range even when the transmission is being decoded using harmonics with frequencies greater than 4.0 kHz. In practice, changes in the noise level and  $N_0$  are small compared to changes in  $E_b$ , and variations in  $E_b/N_0$  are dominated by different generation conditions leading to different signal strengths.

Experiments were conducted in 2011 on July 19 from 0932–1000 UT, July 20 from 0831–0900 UT, July 21 from 0901–0929 UT, July 24 from 0601–0630 UT, July 26 from 0729–0759 UT, and July from 27 0658–0759 UT and 0802–0832 UT.

The results of these experiments are shown in Figure 6.2 for the 3 bit rates and 3 ELF frequencies used. Each plot shows the bit error rate as a function of  $E_b/N_0$  for

both sine and square wave modulation where each point represents the measured error rate in one received packet, and “No errors” indicates that no errors were present. The area surrounding each line represents a 95% confidence interval around the estimated bit error rate. This interval assumes that errors follow a binomial distribution in each packet and is based only on the number of errors, not on variability such as one packet randomly suffering from more sferics than another. Only the fundamental is used to decode the signal. Several features on these plots are apparent. Square wave modulation and the higher frequencies (2125, and 2735 Hz) are more effective at generating ELF radiation, so there are more points with higher values of  $E_b/N_0$ . Lower bit rates also have higher values of  $E_b/N_0$  since each symbol is transmitted for a longer period. However, a lower bit rate also means that each packet (which contains similar numbers of bits regardless of the bit rate) takes longer to transmit. If the ionosphere is highly variable during the 40 seconds it takes to transmit a packet at 100 bps, then the known waveform used as a phase reference may not be accurate for the duration of the transmission. Variation of the phase reference may result in the occasional outliers at 100 bps where the error rate is much higher than expected because there is more time for the phases of the received signal to drift.

Figure 6.3 shows an example of the variation of the bit error rate when using the first three harmonics to decode a 1510 Hz signal at 400 bps. For square wave modulation, the red dashed line representing the use of 3 harmonics is shifted by 5–10 dB to the right indicating the larger signal energy provided by the extra harmonics. When compared to the bit error rate from using only a fundamental with the same energy, the bit error rate improves when  $E_b/N_0$  is less than 10 dB but worsens at higher values of  $E_b/N_0$ . This improvement indicates that having energy in the higher harmonics is better than having it in the fundamental for low values of  $E_b/N_0$ , possibly due to the interference in the 1510 Hz fundamental from a harmonic of 60 Hz power line noise at 1500 Hz. For higher values of  $E_b/N_0$ , the additional energy is unnecessary and may be contributing additional impulsive noise from sferics at higher frequencies. With sine wave modulation, the harmonics are much weaker and including them does not appreciably change the bit error rate.

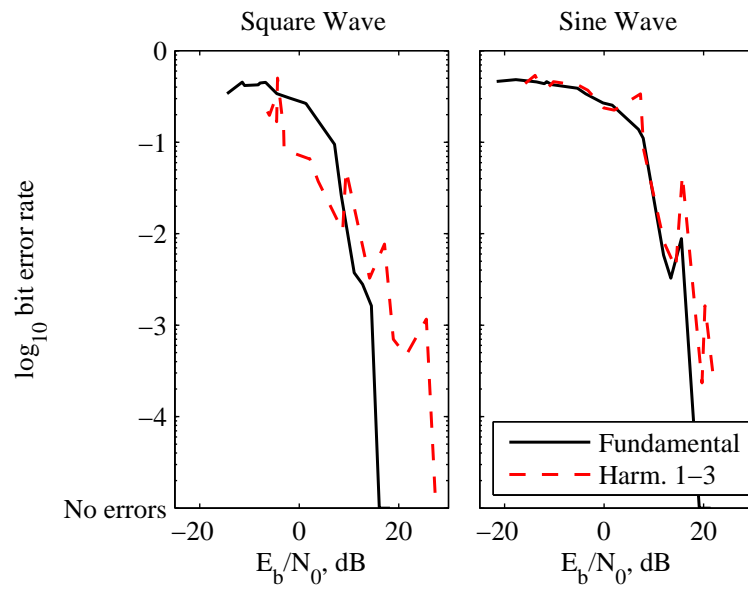


Figure 6.3: Bit error rate as a function of  $E_b/N_0$  for a 1510 Hz ELF frequency at 400 bps when using only the fundamental (black solid) and when using the first 3 harmonics (red dashed). Bit error rate improves when using additional harmonics for square wave modulation when  $E_b/N_0$  is low, but makes little difference for sine wave modulation.

### 6.3 Simulations

Because of limited transmission time at HAARP, the experimental results are limited for the purpose of comparing transmission using one set of parameters to those at another or for comparing with theoretical models of BER performance. A 28-minute block contains only 2 repetitions of a specific, modulation type, ELF frequency, and bit rate. Over the course of the entire campaign, only 16 repetitions of approximately 4000 bits means a total of 64000 bits transmitted using a particular combination of parameters. This data set is not sufficient to deduce BER below  $10^{-4}$  as can occur for very high signal to noise ratios. Thus, it is helpful to develop a simple simulation of this communication system to provide better BER statistics.

In order to simulate the received ELF signal, a typical waveform is extracted from data received at past HAARP campaigns and phase shifted appropriately to encode the data. For example, to simulate transmission using square wave modulation, we use data from an experiment on April 2, 2011 where 2 second square wave pulses were transmitted at HAARP and received at Chistochina under strong generation conditions. One period of the received waveform can then be extracted by dividing the received signal into segments one ELF period in length and averaging all the segments. This procedure retains any components that are periodic while averaging away some of the noise. Alternatively an FFT of the 2 second pulse can be taken, keeping only the terms representing frequencies at integer multiples of the ELF frequency. An inverse FFT can then be taken to obtain a time domain waveform. This canonical waveform is then used to encode the signal in simulations. For example, to simulate transmission of the bits 01, the derived waveform is time-shifted by a quarter of a period. Once the encoding is complete, the entire signal is then scaled to represent stronger or weaker generation resulting in different signal-to-noise ratios. This simulation ignores all heating physics and propagation effects. Waveforms at different phase shifts are simply concatenated together to represent different symbols, leading to sharp discontinuities that are not physical. However the heating and cooling time constants of the ionospheric plasma are no more than  $\sim 100$  microseconds, which is a small fraction of the symbol period of 2.5 ms even at 800 bps, so we assume that

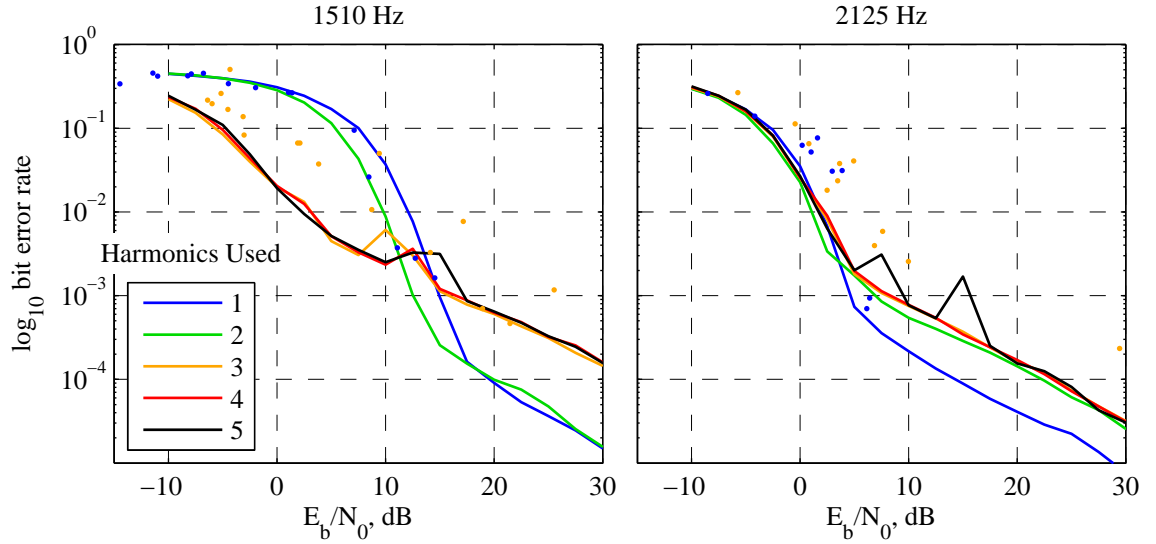


Figure 6.4: Simulated bit error rate as a function of  $E_b/N_0$  for 1510 and 2125 Hz ELF frequencies at 400 bps when using different numbers of harmonics. At 1510 Hz, bit error rate improves for smaller values of  $E_b/N_0$  when using up to 3 harmonics. At 2125 Hz bit error rate only improves after adding the second harmonic. For comparison, dots represent experimental data when using 1 and 3 harmonics.

effects at the symbol boundaries are small. This simulation also does not account for changes in the signal that may occur over the course of the transmission, such as strengthening or weakening of ELF generation, changes in the harmonic content, or drifts of the phase of the received signal due to ionospheric changes.

To simulate the VLF noise environment, actual data from a VLF receiver is also used. A half hour block taken from the campaign on July 22, 2011 at 1100 UT is used since HAARP was not transmitting but the period immediately followed experiments from the campaign. A random segment of this block is added to the scaled, encoded, signal. Both the signal and noise are sampled at 100 kHz. The resulting sum of signal and noise is then passed to the same software decoder used to decode signals from the actual experiment. The decoder outputs the BER, and the simulation can be run as many times as necessary in order to obtain reliable statistics.

Figure 6.4 shows simulated bit error rates for transmissions at 400 bps using square wave modulation at ELF frequencies of 1510 and 2125 Hz with varying numbers of

harmonics used. For the 1510 Hz case, using two harmonics improves the bit error rate by a factor of 2–7 for  $E_b/N_0$  between 7–15 dB. Using three harmonics results in a dramatic improvement, where the BER improves by nearly a factor of 40 for  $E_b/N_0$  of 5 dB. Data from the actual experiment when using 1 and 3 harmonics indicated by the dots show a more modest improvement in BER when using 3 harmonics. The bit error rate when using 3 harmonics is actually worse than using only the fundamental for  $E_b/N_0$  greater than 15 dB. When the received signal is very strong, the error rates are already very low. Using additional harmonics at higher frequencies may expose the received signal to greater levels of impulsive noise, which worsens the bit error rate under these circumstances.

At 2125 Hz, using additional harmonics results in only a slight improvement in BER for  $E_b/N_0 < 3$  dB, while still worsening the BER for the stronger signals. Additional harmonics are more beneficial to the 1510 Hz transmission for several reasons. ELF generation at 1510 Hz is weaker than at 2125 Hz, and the 1510 Hz signal receives greater interference from the very strong 25th harmonic of 60 Hz power line noise at 1500 Hz. Square wave modulation results in a very strong third harmonic component which suffers much less power line interference and reduces the bit error rate dramatically, whereas the weaker second harmonic only contributes to a small improvement in bit error rate. As the number of harmonics increases beyond three, the additional higher harmonics become weaker, in addition to being in a stronger noise environment. Figure 6.1 shows the impulsive noise increases beyond  $\sim 4.5$  kHz. Thus, the fourth and higher harmonics of the 1510 Hz transmission and the third and higher harmonics of the 2125 Hz transmission have poor signal to noise ratios and do not contribute to further reductions in the bit error rate.

## 6.4 Theoretical Performance Models

In order to characterize the bit error rate of this ELF communication system, we would like to fit mathematical expressions for BER developed in past work to this new system with the complication that the characteristics of the noise changes as harmonics at higher frequencies are added. A closed form expression for the bit

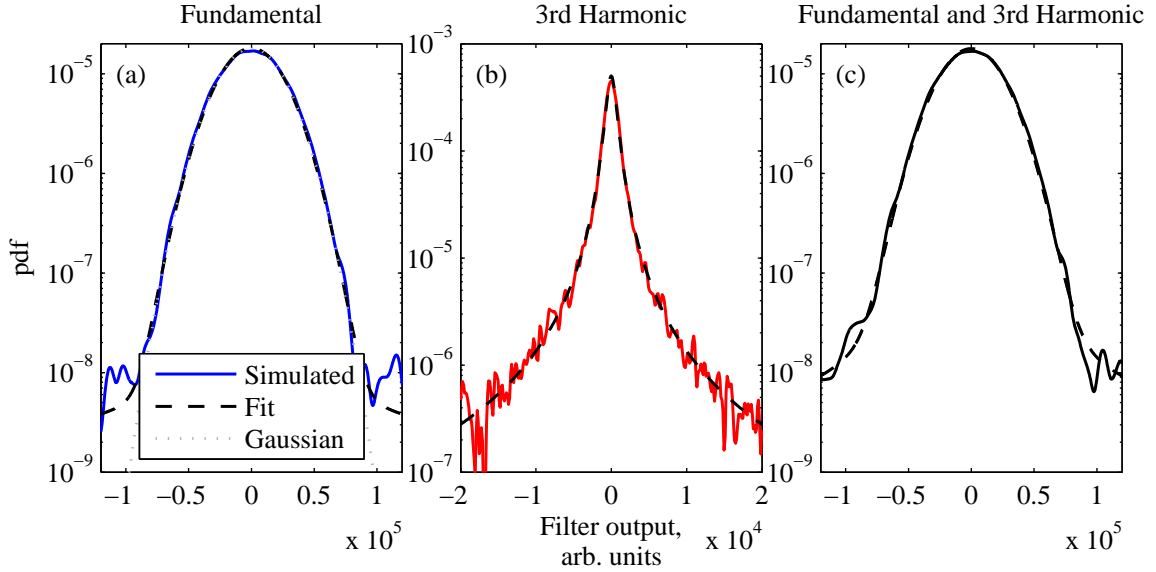


Figure 6.5: Probability density function at output of matched filter derived from 20000 segments of VLF noise 5 ms long and a fit using mathematical models in the dashed lines.

error rate makes it much faster to iterate and optimize over different parameters than repeatedly running large simulations. To examine a simplified version of this problem, we consider only the fundamental and third harmonic of a 2125 Hz signal. The fundamental is received very strongly and is at a frequency that is not strongly affected by either 60 Hz power line harmonics and only affected by strong nearby sferics. The third harmonic at 6375 Hz, however, is subject to primarily impulsive noise from sferics.

A QPSK system is easier to analyze as two independent binary phase shift keying (BPSK) systems. BPSK uses only two phases to transmit one bit (e.g.  $x_0(t) = -\cos(2\pi ft)$  and  $x_1(t) = \cos(2\pi ft)$ ) where  $x_0(t)$  and  $x_1(t)$  are the symbols representing a 0 and 1 bit. Since the sine and cosine functions are orthogonal, a second BPSK signal using  $\sin(2\pi ft)$  and  $-\sin(2\pi ft)$  can be transmitted on the same channel without interference and the BER of QPSK is actually the same as for BPSK. The same holds true if the symbol is a combination of odd harmonics, such as



$x_0(t) = \cos(2\pi ft) + b \cos(6\pi ft + \phi)$ , where  $b$  and  $\phi$  are the amplitude and phase of the third harmonic relative to the first. For a received signal  $y = x(t) + n(t)$ , where  $n(t)$  is the noise, the output of the correlator is:

$$\frac{1}{T} \int_0^T x_1(t)y(t) dt \quad (6.1)$$

$$= E + \frac{1}{T} \int_0^T x_1(t)n(t) dt \quad (6.2)$$

where  $E$  is the energy in the signal. Thus, an error occurs when the noise term is greater than  $E$  since this would cause the correlator output to be the wrong sign and the decision would be for the incorrect bit. The error probability is determined from the probability density function (pdf) of the noise term which can be integrated to determine the probability of the noise term being greater than  $E$ . To estimate the pdf, we examine the output when noise is injected into the correlator. Figure 6.5 shows the pdf of the output of three correlators when 20000 segments of ELF/VLF noise 5 ms in length (corresponding to a 400 bps bit rate) are used as input. The correlators are matched to a typical 2125 Hz ELF signal generated by HAARP using only the fundamental, only the third harmonic, and both the fundamental and third harmonic. At the fundamental, the pdf closely resembles a Gaussian (gray dotted line) until values greater than approximately  $10^5$  where a heavy tail begins. This tail represents the presence of rare but strong sferics that add an impulsive component to the otherwise largely Gaussian noise. A mixture of Gaussian and impulsive noise was modeled in *Ziemer* (1967) and the resulting pdf reproduced below:

$$p_1(n) = (1 - \gamma) \frac{e^{-n^2/(2\sigma_G^2)}}{\sqrt{2\pi\sigma_G^2}} + 2 \left( \frac{\gamma}{\pi} \right)^{3/2} \int_0^{\pi/2} \frac{\exp\left[\frac{-\gamma n^2}{2(\gamma\sigma_G^2 + 2\sigma_I^2 \cos^2 y)}\right]}{\sqrt{2(\gamma\sigma_G^2 + 2\sigma_I^2 \cos^2 y)}} dy \quad (6.3)$$

where  $\sigma_G^2$  and  $\sigma_I^2$  are the variances of the Gaussian and impulsive components of the noise,  $n$ , and  $\gamma$  is the average number of noise impulses occurring during one symbol period. Values of  $\sigma_G = 22000$ ,  $\sigma_I = 6000$ , and  $\gamma = 2.6 \times 10^{-3}$  fit the simulated pdf

well and is shown as the dotted black line.

The pdf of the correlator using only the third harmonic at 6375 Hz is clearly non-gaussian and very heavy-tailed. The third harmonic is also weaker than the fundamental (note the different scales on the  $x$ -axis in Figure 6.5). We found that the generalized “t” model described in *Hall* (1966, pg. 16) provides a better fit in this case:

$$p_3(n) = \frac{\Gamma(\theta/2)}{\Gamma((\theta-1)/2)} \frac{\beta^{\theta-1}}{\sqrt{\pi}(n^2 + \beta^2)^{\theta/2}} \quad (6.4)$$

where  $\Gamma$  is the gamma function,  $\beta$  is a parameter specifying the width of the distribution, which is related to the total noise energy, and  $\theta$  is a parameter specifying the slope of the tail of the distribution. Values of  $\beta = 750$  and  $\theta = 2.282$  were used to fit this distribution to simulations in Figure 6.5b and are consistent with results in *Hall* (1966) where values of  $\theta$  between 2 and 4 fit measured data.

A correlator that incorporates both the fundamental and the third harmonic is equivalent to summing the output of the correlators using only the fundamental and only the third harmonic. The pdf of the output of this correlator is given by the convolution of the pdfs of the correlator using the individual harmonics (equations 6.3 and 6.4) assuming the two noise processes are independent. The noise processes occurring at the fundamental and third harmonic frequencies are not independent as a strong sferic that appears at the fundamental also likely appears in the third harmonic. However, given that strong harmonics in the fundamental are infrequent ( $\gamma \ll 1$ ), then it is reasonable to expect that the primarily Gaussian noise at the fundamental frequency is independent of the large amount of impulsive noise at the third harmonic frequency. Figure 6.5c shows the pdf of the correlator using both the fundamental and third harmonic, as well as the pdf obtained by convolving eq. 6.3 and 6.4. The behavior of this pdf is very similar to that using only the fundamental since the fundamental is stronger and thus weighted more. However the tails of the distribution are elevated because of the large impulsive component from the third harmonic.

The bit error rate can be computed by integrating the pdf to find the probability that the noise at the matched filter output is greater than the energy in the signal:

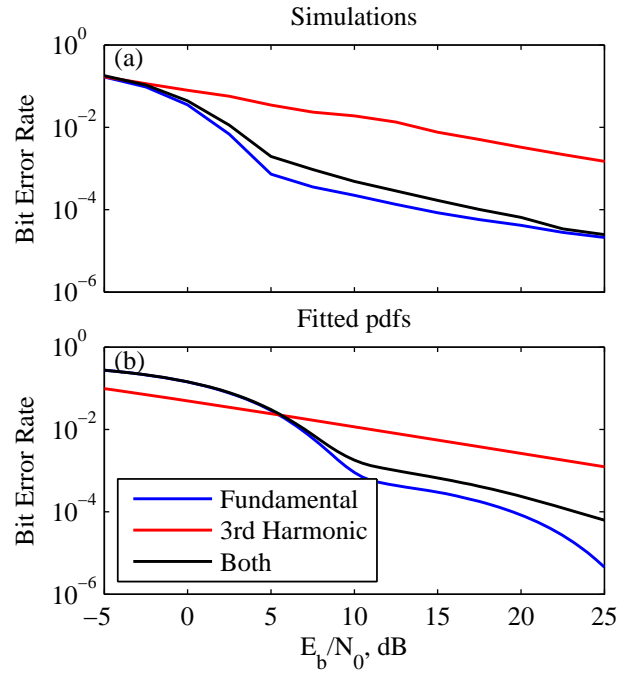


Figure 6.6: Bit error rates computed from simulation (a) and from integrating expressions of the noise pdf (b). Adding the third harmonic generally results in a worse bit error rate compared to using only the fundamental with the same signal energy. The BER from the fitted pdfs is able to reproduce the behavior in the simulations.

$$P_e = \int_E^\infty p(n) dn \quad (6.5)$$

where  $P_e$  is the probability of error, or bit error rate, and  $p(n)$  is the noise pdf at the correlator output. The resulting bit error rates computed by integrating eq. 6.3, 6.4, and their convolution are shown in Figure 6.6 together with the bit error rates from simulations conducted as in Section 6.3. Although there are discrepancies between the two methods of determining the BER that could be the result of inconsistent calculations of the signal energy, the BER computed from the pdfs are still able to reproduce the overall behavior seen in the simulations. Using both the first and third harmonic results in a worse BER compared to using only a fundamental with the same energy as the first and third harmonic combined. This result is especially noticeable at higher values of  $E_b/N_0$  where impulsive noise becomes the dominant source of errors and the noise in the third harmonic is largely impulsive.

## 6.5 Conclusion

Experiments were conducted at HAARP where QPSK modulated signals were used to transmit data using three ELF frequencies (1510, 2125, and 2735 Hz) and using both sine and square wave modulation. We find that bit error rates are lower for square wave modulation at 2125 and 2735 Hz, which generates stronger transmitted signals. Using the strong harmonics generated using square wave modulation further reduced the bit error rate when the signal was weak. When including higher harmonics, the greatest reduction in BER occurred at a frequency of 1510 Hz as the fundamental is weaker and exposed to more interference from power lines. However, simulations of this communication system using waveforms and noise derived from data showed that using additional harmonics only lowers the BER when the harmonics are below  $\sim 4.5$  kHz. Impulsive noise from sferics is the dominant source of errors at higher frequencies and for stronger signals and limits the BER performance in these regimes. The performance of a receiver using a fundamental below 4.5 kHz and a third harmonic above can be modeled by combining existing mathematical expressions for the

noise distribution at these frequencies. This model can reproduce the BER features observed in simulation that show that the inclusion of higher harmonics does not improve the BER when the higher harmonics are exposed to more impulsive noise.

# Chapter 7

## Conclusions and Future Work

### 7.1 Conclusions

ELF and VLF waves have incredibly diverse applications. In geophysics, they can be used to study everything from the deep Earth to near-Earth space in the magnetosphere; for communications, they are the only means of transmitting to submerged submarines over long distances. Yet ELF/VLF waves have always been very difficult to generate due to their long wavelengths. Modulated ionospheric heating, which uses high power HF transmitters to induce natural ionospheric currents to act as an ELF antenna, skirts around the challenges of building an enormous traditional transmitter. Yet this clever technique is no panacea as it introduces new challenges, including a dependence on natural conditions and strong nonlinear distortion. In this work, we presented results that can be of immediate practical use in understanding both challenges, and ended with a demonstration on the manner in which natural conditions and nonlinear distortion affect digital data transmission in an actual communications experiment. We summarize these key results here, before offering some remarks on future directions of this research.

Since modulated ionospheric heating utilizes the electrojet as its current source, it is intuitive that the amplitude of ELF waves generated by modulated heating would correlate directly with magnetometer measurements of the electrojet intensity. In collecting experimental data over two years of experiments, this direct correlation

was in fact observed in most (55%) of cases. Yet there were still cases of negative or poor correlation, as well as a change in the proportionality constant between ELF amplitude and magnetometer data even when the two were well correlated. In particular, disturbed intervals with a very strong electrojet resulted in a smaller proportionality constant—these periods with a very strong electrojet should result in very strong ELF generation, but the actual change in ELF amplitude is small. Conversely though, there is often surprisingly robust ELF generation even during periods of weak electrojet.

As the electrojet strength is the product of both an electric field and the ionospheric conductivity, it helps to include a second instrument to estimate the ionospheric electron density governing the conductivity. We use magnetometer and riometer measurements to train a statistical model for ELF amplitude. This statistical model estimates the ELF amplitude given magnetometer and riometer measurements based on the data used to train it. For a fixed value of riometer absorption, ELF amplitude was linearly correlated with magnetometer measurements of the electrojet as expected. However, when riometer absorption increases, the ELF/magnetometer proportionality constant decreases and vice versa. The inverse relationship between ionospheric density and the ELF/magnetometer proportionality constant is consistent with the proportionality constant decreasing during strong electrojets as strong electrojets are associated with enhancements in ionospheric density. Besides the scientific results provided by the statistical model, there is also the practical application of predicting estimated ELF amplitudes when given measurements from other ionospheric instruments.

We use numerical modeling to explain the theoretical reasons for the change in ELF/magnetometer proportionality constant with ionospheric density. When the ionospheric density is constant, changes in the electric field affect both the electrojet and ELF generation linearly. ELF amplitude and electrojet strength are thus linearly related, and the proportionality constant is fixed. For more dense ionospheric profiles, the numerical models show that the electrojet strengthens more than ELF amplitude, and thus the proportionality constant decreases. For a less dense ionosphere, the electrojet weakens more than the ELF amplitude, and the proportionality

constant increases. Thus, an electrojet driven by a strong electric field is conducive to strong ELF generation even if the ionosphere is less dense and the electrojet is weak. However, even a very strong electrojet may not be conducive to strong ELF generation if the strong electrojet results only from a dense ionosphere as opposed to a strong electric field.

Numerical modeling is also vital in addressing the challenge of nonlinear distortion in ELF generation. The principle behind modulated ionospheric heating is the conversion between HF power and changes in the ionospheric conductivity, a process that is highly nonlinear. Even a sinusoidal variation in HF power produces a non-sinusoidal variation in conductivity, leading to distorted ELF waves with harmonics that occupy bandwidth. To obtain a sinusoidal conductivity variation that minimizes harmonics, we run the numerical HF heating model backwards. We start with a sinusoidal conductivity and determine what the HF power waveform must be. Unfortunately, the conductivity can only be sinusoidal at a specific altitude so that this process also requires knowledge of the correct ionospheric density profile. Modeling shows that an ionosphere that is more dense than the one assumed results in more harmonic distortion compared to simple sinusoidal modulation. Experiments using different waveforms also showed that sinusoidal modulation created slightly less harmonic distortion than the inverted waveforms. Minimizing harmonics is thus a challenging problem and in many applications it may not be a primary concern. Square wave modulation generates very strong harmonics but also generates the most total power, the most power in the fundamental, and can be very efficient at low duty cycles. Sinusoidal modulation has lower distortion but generates less power and is less efficient, while the inverted waveform has intermediate levels of distortion and efficiency. The choice of modulation waveform is then a tradeoff between harmonic distortion and efficiency.

Communications is one example of an application where it is desirable to minimize harmonic distortion if possible, but where harmonics can also be used to decode the signal when harmonic minimization is not possible. In an experiment where digital data is transmitted using QPSK with sine and square wave modulation, square wave resulted in lower bit error rates since it generated stronger signals at the fundamental



frequency. The bit error rate improves further as more harmonics are utilized since the harmonics for square wave modulation are also stronger than those for sine wave modulation. However, there are limitations to the use of harmonics as the higher harmonics are at frequencies which suffer from higher levels of impulsive noise from sferics. Using harmonics beyond  $\sim 4.5$  kHz may actually increase the number of errors because of the impulsive noise. Although the choice of waveform and the harmonics used affect the bit error rate, the variation in the signal strength due to natural conditions is also a major factor in decoding the transmitted signals, illustrating the importance of understanding the role of both natural and human-controllable parameters in ELF generation.

## 7.2 Future Work

Though modulated heating has been around over 30 years, and HAARP for nearly a decade, there are always more questions to answer, more data to sift, and more models to run. Below, are some suggestions for future directions in this area:

### 7.2.1 Correlation with radar data

Experiments at Tromsø showed a very strong correlation between ELF amplitude and radar measurements of the electric field (*Rietveld et al.*, 1987). Unfortunately, HAARP presently lacks a powerful incoherent scatter radar nearby. If one is eventually moved there, any attempt to directly measure *D*-region electron densities and the ionospheric electric field would greatly increase our understanding of precisely how ELF generation changes with ionospheric density and electric field.

### 7.2.2 Electrojet spatial structure

The electrojet varies in intensity overhead, but it also moves spatially and exhibits small scale spatial structure. Further HAARP experiments where the beam is pointed at different areas of the sky might be able to map this structure by observing how ELF amplitude changes with beam position.

### 7.2.3 Harmonic minimization with feedback from ELF measurements

Though a difficult problem, if the observed harmonic content from a ground-based receiver could somehow feed back into a numerical heating model, it may then be possible to iteratively adjust parameters such as the electron density profile until the simulated harmonic content agrees with the measured one. The heating model could also feed new waveforms out and adjust them until harmonic distortion is minimized. Such a procedure would simultaneously solve for both the  $D$ -region ionospheric density and minimize the generated harmonics.

### 7.2.4 Spread spectrum communications and modulated heating

Communications using modulated heating is still vastly unexplored. We use QPSK, which is a narrowband technique for transmitting digital data. However, are spread spectrum techniques possible? For example, orthogonal frequency division multiplexing (OFDM), uses carriers at many frequencies, each of which can be encoded with a narrowband technique such as QPSK. However, such a scheme is very sensitive to nonlinear distortion, and the carriers may interfere with each other. Could such a technique work and would predistorting the signal help?

# Bibliography

- Banks, P. (1966), Collision frequencies and energy transfer. Electrons, *Planet. Space Sci.*, *14*, 1085–+, doi:10.1016/0032-0633(66)90024-9.
- Barr, R. (1998), The generation of ELF and VLF radio waves in the ionosphere using powerful HF transmitters, *Advances in Space Research*, *21*, 677–687, doi:10.1016/S0273-1177(97)01003-X.
- Barr, R., and P. Stubbe (1984), ELF and VLF radiation from the “polar electrojet antenna”, *Radio Science*, *19*, 1111–1122, doi:10.1029/RS019i004p01111.
- Barr, R., W. Ireland, and M. J. Smith (1993), Elf, vlf and lf radiation from a very large loop antenna with a mountain core, *Microwaves, Antennas and Propagation, IEE Proceedings H*, *140*(2), 129–134.
- Baumjohann, W. (1982), Ionospheric and field-aligned current systems in the auro-ral zone - A concise review, *Advances in Space Research*, *2*, 55–62, doi:10.1016/0273-1177(82)90363-5.
- Baumjohann, W., and R. A. Treumann (1997), *Basic Space Plasma Physics*, Imperial College Press, London, doi:10.1007/b97705.
- Belyaev, P. P., D. S. Kotik, S. N. Mityakov, S. V. Polyakov, V. O. Rapoport, and V. Y. Trakhtengerts (1987), Generation of electromagnetic signals at combination frequencies in the ionosphere, *Radiophysics and Quantum Electronics*, *30*, 189–206, doi:10.1007/BF01034491.

- Bernstein, S. L., M. L. Burrows, J. E. Evans, A. S. Griffiths, D. A. McNeill, C. W. Niessen, I. Richer, D. P. White, and D. K. Willim (1974), Long-range communications at extremely low frequencies, *Proceedings of the IEEE*, 62(3), 292 – 312, doi:10.1109/PROC.1974.9426.
- Bilitza, D., C. Koblinsky, R. Williamson, and S. Bhardwaj (1998), Improving the topside electron density model for IRI, *Advances in Space Research*, 22, 777–787, doi:10.1016/S0273-1177(98)00098-2.
- Bittencourt, J. A. (2004), *Fundamentals of Plasma Physics*, 3 ed., Springer, New York, doi:10.1007/b97705.
- Budden, K. G. (1961), *The Wave-Guide Mode Theory of Wave Propagation*, Prentice-Hall, Englewood Cliffs, NJ.
- Budden, K. G. (1985), *The propagation of radio waves: The theory of radio waves of low power in the ionosphere and magnetosphere*, Cambridge University Press, Cambridge.
- Burgess, B., and T. B. Jones (1969), Search for the effect of stellar X-ray on the night-time lower ionosphere., *Nature*, 224, 680–681.
- Carpenter, D. L., and Z. T. Bao (1983), Occurrence properties of ducted whistler-mode signals from the new VLF transmitter at Siple Station, Antarctica, *J. Geophys. Res.*, 88, 7051–7057, doi:10.1029/JA088iA09p07051.
- Chevalier, M., and U. Inan (2006), A Technique for Efficiently Modeling Long-Path Propagation for Use in Both FDFD and FDTD, *IEEE Antennas and Wireless Propagation Letters*, 5, 525–528, doi:10.1109/LAWP.2006.887551.
- Chevalier, M. W., W. B. Peter, U. S. Inan, T. F. Bell, and M. Spasojevic (2007), Remote sensing of ionospheric disturbances associated with energetic particle precipitation using the South Pole VLF beacon, *Journal of Geophysical Research (Space Physics)*, 112, A11306, doi:10.1029/2007JA012425.

- Chisham, G., et al. (2007), A decade of the Super Dual Auroral Radar Network (SuperDARN): scientific achievements, new techniques and future directions, *Surveys in Geophysics*, *28*, 33–109, doi:10.1007/s10712-007-9017-8.
- Cohen, M. B. (2009), ELF/VLF Phased Array Generation via Frequency-matched Steering of a Continuous HF Ionospheric Heating Beam, Ph.D. thesis, Stanford Univ., Stanford, Calif.
- Cohen, M. B., M. Gołkowski, and U. S. Inan (2008), Orientation of the HAARP ELF ionospheric dipole and the auroral electrojet, *Geophys. Res. Lett.*, *35*, 2806–+, doi:10.1029/2007GL032424.
- Cohen, M. B., U. S. Inan, M. Gołkowski, and M. J. McCarrick (2010a), ELF/VLF wave generation via ionospheric HF heating: Experimental comparison of amplitude modulation, beam painting, and geometric modulation, *Journal of Geophysical Research (Space Physics)*, *115*(A14), 2302–+, doi:10.1029/2009JA014410.
- Cohen, M. B., U. S. Inan, M. Gołkowski, and N. G. Lehtinen (2010b), On the generation of ELF/VLF waves for long-distance propagation via steerable HF heating of the lower ionosphere, *Journal of Geophysical Research (Space Physics)*, *115*(A14), 7322–+, doi:10.1029/2009JA015170.
- Cohen, M. B., U. S. Inan, and E. W. Paschal (2010c), Sensitive Broadband ELF/VLF Radio Reception With the AWESOME Instrument, *IEEE Transactions on Geoscience and Remote Sensing*, *48*, 3–17, doi:10.1109/TGRS.2009.2028334.
- Cohen, M. B., M. Golkowski, N. G. Lehtinen, U. S. Inan, and M. J. McCarrick (2012), HF beam parameters in ELF/VLF wave generation via modulated heating of the ionosphere, *Journal of Geophysical Research (Space Physics)*, *117*, A05327, doi:10.1029/2012JA017585.
- Cotts, B. R. T., and U. S. Inan (2007), VLF observation of long ionospheric recovery events, *Geophys. Res. Lett.*, *34*, L14809, doi:10.1029/2007GL030094.

- Dalgarno, A., M. B. McElroy, M. H. Rees, and J. C. G. Walker (1968), The effect of oxygen cooling on ionospheric electron temperatures, *Planetary and Space Science*, *16*, 1371, doi:10.1016/0032-0633(68)90141-4.
- El-Arini, M. B., S. A. Mitry, and R. Lee (1990), Tacamo antenna analysis for the new high power transmit set (hpts), in *Military Communications Conference, 1990. MILCOM '90, Conference Record, A New Era. 1990 IEEE*, vol. 3, pp. 1071–1079, doi:10.1109/MILCOM.1990.117578.
- Ferraro, A. J., H. S. Lee, R. A. Allshouse, K. Carroll, A. A. Tomko, F. J. Kelly, and R. G. Joiner (1982), VLF/ELF radiation from the ionospheric dynamo current system modulated by powerful HF signals, *Journal of Atmospheric and Terrestrial Physics*, *44*, 1113–1122.
- Ferraro, A. J., H. S. Lee, R. Allshouse, K. Carroll, R. Lunnen, and T. Collins (1984), Characteristics of ionospheric ELF radiation generated by HF heating, *Journal of Atmospheric and Terrestrial Physics*, *46*, 855–865.
- Ferraro, A. J., H. S. Lee, T. W. Collins, M. Baker, and D. Werner (1989), Measurements of extremely low frequency signals from modulation of the polar electrojet above Fairbanks, Alaska, *IEEE Transactions on Antennas and Propagation*, *37*, 802–805, doi:10.1109/8.29370.
- Field, E. C., L. R. Kies, P. R. Bannister, R. F. Ingrahm, W. D. Hopkins, and M. A. Roberts (1989), An aerostat supported ELF/VLF transmitter, *Radio Science*, *24*, 235–246, doi:10.1029/RS024i002p00235.
- Fine, T. L. (1999), *Feedforward Neural Network Methodology*, Statistics for Engineering and Information Science, Springer-Verlag, New York, doi:10.1007/b97705.
- Foust, F. R., M. Spasojevic, T. F. Bell, and U. S. Inan (2011), Modeling scattering from lightning-induced ionospheric disturbances with the discontinuous Galerkin method, *Journal of Geophysical Research (Space Physics)*, *116*, A12301, doi:10.1029/2011JA016973.

- Friedrich, M., and M. Rapp (2009), News from the lower ionosphere: A review of recent developments, *Surveys in Geophysics*, *30*, 525–559, 10.1007/s10712-009-9074-2.
- Getmantsev, G. G., N. A. Zuikov, D. S. Kotik, L. F. Mironenko, N. A. Mitiakov, V. O. Rapoport, I. A. Sazonov, V. I. Trakhtengerts, and V. I. Eidman (1974), Combination frequencies in the interaction between high-power short-wave radiation and ionospheric plasma, *Soviet JETP Letters*, *20*, 229–232.
- Gibby, A. R., U. S. Inan, and T. F. Bell (2008), Saturation effects in the VLF-triggered emission process, *Journal of Geophysical Research (Space Physics)*, *113*, A11215, doi:10.1029/2008JA013233.
- Gołkowski, M., U. S. Inan, A. R. Gibby, and M. B. Cohen (2008), Magnetospheric amplification and emission triggering by ELF/VLF waves injected by the 3.6 MW HAARP ionospheric heater, *Journal of Geophysical Research (Space Physics)*, *113*, A10201, doi:10.1029/2008JA013157.
- Gołkowski, M., M. B. Cohen, D. L. Carpenter, and U. S. Inan (2011), On the occurrence of ground observations of ELF/VLF magnetospheric amplification induced by the HAARP facility, *Journal of Geophysical Research (Space Physics)*, *116*, A04208, doi:10.1029/2010JA016261.
- Graf, K. L., U. S. Inan, and M. Spasojevic (2011), Transmitter-induced modulation of subionospheric vlf signals: Ionospheric heating rather than electron precipitation, *Journal of Geophysical Research*, *116*, doi:10.1029/2011JA016996.
- Hagan, M. T., and M. B. Menhaj (1994), Training feedforward networks with the Marquardt algorithm, *IEEE Transactions on Neural Networks*, *5*(6), 989–993.
- Hall, H. M. (1966), New model for impulsive phenomena: application to atmospheric noise communication channels, *Tech. rep.*, Stanford Electronics Laboratories.
- Hedin, A. E. (1991), Extension of the MSIS thermosphere model into the middle and lower atmosphere, *J. Geophys. Res.*, *96*, 1159–1172, doi:10.1029/90JA02125.

- Helliwell, R. A., and J. P. Katsufakis (1974), VLF wave injection into the magnetosphere from Siple Station, Antarctica, *J. Geophys. Res.*, *79*, 2511, doi:10.1029/JA079i016p02511.
- Helliwell, R. A., J. Katsufakis, M. Trimpi, and N. Brice (1964), Artificially Stimulated Very Low Frequency Radiation from the Ionosphere, *J. Geophys. Res.*, *69*, 2391–2394, doi:10.1029/JZ069i011p02391.
- Helliwell, R. A., J. P. Katsufakis, and M. L. Trimpi (1973), Whistler-Induced Amplitude Perturbation in VLF Propagation, *J. Geophys. Res.*, *78*, 4679–4688, doi:10.1029/JA078i022p04679.
- Huxley, L. G. H., and J. A. Ratcliffe (1949), A survey of ionospheric cross-modulation (wave interaction or luxembourg effect), *Proceedings of the IEE - Part III: Radio and Communication Engineering*, *96*(43), 433 –440, doi:10.1049/pi-3.1949.0093.
- Ingram, R. (1984), Performance of the locally optimum threshold receiver and several suboptimal nonlinear receivers for elf noise, *Oceanic Engineering, IEEE Journal of*, *9*(3), 202 – 208, doi:10.1109/JOE.1984.1145615.
- International Association of Geomagnetism and Aeronomy, C. C., Working Group V-MOD. Participating members Finlay, et al. (2010), International geomagnetic reference field: the eleventh generation, *Geophysical Journal International*, *183*(3), 1216–1230, doi:10.1111/j.1365-246X.2010.04804.x.
- James, H. G. (1985), The ELF spectrum of artificially modulated D/E-region conductivity, *Journal of Atmospheric and Terrestrial Physics*, *47*, 1129–1142.
- James, H. G., R. L. Dowden, M. T. Rietveld, P. Stubbe, and H. Kopka (1984), Simultaneous observations of ELF waves from an artificially modulated auroral electrojet in space and on the ground, *J. Geophys. Res.*, *89*, 1655–1666, doi:10.1029/JA089iA03p01655.



- Jin, G., M. Spasojevic, and U. S. Inan (2009), Relationship between electrojet current strength and ELF signal intensity in modulated heating experiments, *Journal of Geophysical Research (Space Physics)*, *114*(A13), 8301–+, doi:10.1029/2009JA014122.
- Jin, G., M. Spasojevic, M. B. Cohen, U. S. Inan, and N. G. Lehtinen (2011), The relationship between geophysical conditions and ELF amplitude in modulated heating experiments at HAARP: Modeling and experimental results, *Journal of Geophysical Research (Space Physics)*, *116*, A07310, doi:10.1029/2011JA016664.
- Jin, G., M. Spasojevic, M. B. Cohen, and U. S. Inan (2012), Harmonic minimization waveforms for modulated heating experiments at HAARP, *Journal of Geophysical Research (Space Physics)*, doi:10.1029/2012JA018102, in press.
- Kamide, Y., S.-I. Akasofu, B.-H. Ahn, W. Baumjohann, and J. L. Kisabeth (1982), Total current of the auroral electrojet estimated from the IMS Alaska meridian chain of magnetic observatories, *Planet. Space Sci.*, *30*, 621–625, doi:10.1016/0032-0633(82)90022-8.
- Kapustin, I. N., R. A. Pertsovskii, A. N. Vasil'Ev, V. S. Smirnov, O. M. Raspopov, L. E. Solov'eva, A. A. Ul'Yachenko, A. A. Arykov, and N. V. Galakhova (1977), Generation of radiation at combination frequencies in the region of the auroral electric jet, *Soviet JETP Lett.*, *25*, 228–+.
- Kassam, S. A. (1988), *Signal Detection in Non-Gaussian Noise*, Springer-Verlag, New York.
- Kirkwood, S., H. Opgenoorth, and J. S. Murphree (1988), Ionospheric conductivities, electric fields and currents associated with auroral substorms measured by the EISCAT radar, *Planet. Space Sci.*, *36*, 1359–1380, doi:10.1016/0032-0633(88)90005-0.
- Kuo, S., A. Snyder, P. Kossey, C.-L. Chang, and J. Labenski (2012), Beating HF waves to generate VLF waves in the ionosphere, *Journal of Geophysical Research (Space Physics)*, *117*, A03318, doi:10.1029/2011JA017076.

- Le, G., J. A. Slavin, and R. J. Strangeway (2010), Space Technology 5 observations of the imbalance of regions 1 and 2 field-aligned currents and its implication to the cross-polar cap Pedersen currents, *Journal of Geophysical Research (Space Physics)*, *115*, A07202, doi:10.1029/2009JA014979.
- Lehtinen, N. G., and U. S. Inan (2008), Radiation of ELF/VLF waves by harmonically varying currents into a stratified ionosphere with application to radiation by a modulated electrojet, *Journal of Geophysical Research (Space Physics)*, *113*(A12), 6301–+, doi:10.1029/2007JA012911.
- Little, C. G., and H. Leinbach (1958), Some measurements of high-latitude ionospheric absorption using extraterrestrial radio waves, *Proceedings of the IRE*, *46*(1), 334–348, doi:10.1109/JRPROC.1958.286795.
- Lunnen, R. J., H. S. Lee, A. J. Ferraro, T. W. Collins, and R. F. Woodman (1984), Detection of radiation from a heated and modulated equatorial electrojet current system, *Nature*, *311*, 134, doi:10.1038/311134a0.
- Lunnen, R. J., A. J. Ferraro, H. S. Lee, R. Allshouse, K. Carroll, D. Werner, and T. W. Collins (1985), Detection of local and long-path VLF/ELF radiation from modulated ionospheric current systems, *Radio Science*, *20*, 553–563, doi:10.1029/RS020i003p00553.
- McKinnell, L., and M. Friedrich (2007), A neural network-based ionospheric model for the auroral zone, *Journal of Atmospheric and Solar-Terrestrial Physics*, *69*, 1459–1470, doi:10.1016/j.jastp.2007.05.003.
- Mentzoni, M. H., and R. V. Row (1963), Rotational Excitation and Electron Relaxation in Nitrogen, *Physical Review*, *130*, 2312–2316, doi:10.1103/PhysRev.130.2312.
- Milikh, G. M., K. Papadopoulos, M. McCarrick, and J. Preston (1999), ELF emission generated by the HAARP HF-heater using varying frequency and polarization, *Radiophysics and Quantum Electronics*, *42*, 639–646, doi:10.1007/BF02676849.

- Moore, R. C. (2007), ELF/VLF wave generation by modulated HF heating of the auroral electrojet, Ph.D. thesis, Stanford Univ., Stanford, Calif.
- Moore, R. C., U. S. Inan, and T. F. Bell (2006), Observations of amplitude saturation in ELF/VLF wave generation by modulated HF heating of the auroral electrojet, *Geophys. Res. Lett.*, *33*, L12106, doi:10.1029/2006GL025934.
- Oikarinen, A., J. Manninen, J. Kultima, and T. Turunen (1997), Observations of intensity variations and harmonics of heater induced VLF waves, *Journal of Atmospheric and Solar-Terrestrial Physics*, *59*, 2351–2360.
- Papadopoulos, K., T. Wallace, M. McCarrick, G. M. Milikh, and X. Yang (2003), On the efficiency of ELF/VLF generation using HF heating of the auroral electrojet, *Plasma Physics Reports*, *29*, 561–565.
- Pashin, A. B., and W. B. Lyatsky (1997), On spectra of ionospheric conductivity variations during a heating experiment, *Radio Science*, *32*, 1513–1522, doi:10.1029/97RS00908.
- Pasko, V. P., and U. S. Inan (1994), Recovery signatures of lightning-associated VLF perturbations as a measure of the lower ionosphere, *J. Geophys. Res.*, *99*, 17,523–17,538, doi:10.1029/94JA01378.
- Payne, J. A. (2007), Spatial structure of very low frequency modulated ionospheric currents, Ph.D. thesis, Stanford Univ., Stanford, Calif.
- Payne, J. A., U. S. Inan, F. R. Foust, T. W. Chevalier, and T. F. Bell (2007), HF modulated ionospheric currents, *Geophys. Res. Lett.*, *34*, L23101, doi:10.1029/2007GL031724.
- Piddyachiy, D., U. S. Inan, T. F. Bell, N. G. Lehtinen, and M. Parrot (2008), DEMETER observations of an intense upgoing column of ELF/VLF radiation excited by the HAARP HF heater, *Journal of Geophysical Research (Space Physics)*, *113*, A10308, doi:10.1029/2008JA013208.

- Raghuram, R., R. Smith, and T. Bell (1974), Vlf antarctic antenna: Impedance and efficiency, *Antennas and Propagation, IEEE Transactions on*, 22(2), 334 – 338, doi:10.1109/TAP.1974.1140777.
- Rietveld, M. T., H. Kopka, E. Nielsen, P. Stubbe, and R. L. Dowden (1983), Ionospheric electric field pulsations - A comparison between VLF results from an ionospheric heating experiment and STARE, *J. Geophys. Res.*, 88, 2140–2146.
- Rietveld, M. T., H.-P. Mauelshagen, P. Stubbe, H. Kopka, and E. Nielsen (1987), The characteristics of ionospheric heating-produced ELF/VLF waves over 32 hours, *J. Geophys. Res.*, 92, 8707–8722.
- Rietveld, M. T., H. Kopka, and P. Stubbe (1988), Pc 1 ionospheric electric field oscillations, *Annales Geophysicae*, 6, 381–388.
- Rodriguez, J. V. (1994), Modification of the Earth's Ionosphere by Very-Low-Frequency Transmitters, Ph.D. thesis, Stanford Univ., Stanford, Calif.
- Ruohoniemi, J. M., and K. B. Baker (1998), Large-scale imaging of high-latitude convection with Super Dual Auroral Radar Network HF radar observations, *J. Geophys. Res.*, 103, 20,797–20,811, doi:10.1029/98JA01288.
- Sen, H. K., and A. A. Wyller (1960), On the Generalization of the Appleton-Hartree Magnetoionic Formulas, *J. Geophys. Res.*, 65, 3931, doi:10.1029/JZ065i012p03931.
- Shepherd, S. G., and J. M. Ruohoniemi (2000), Electrostatic potential patterns in the high-latitude ionosphere constrained by SuperDARN measurements, *J. Geophys. Res.*, 105, 23,005–23,014, doi:10.1029/2000JA000171.
- Storey, L. R. O. (1953), An Investigation of Whistling Atmospherics, *Royal Society of London Philosophical Transactions Series A*, 246, 113–141, doi:10.1098/rsta.1953.0011.
- Stubbe, P. (1996), Review of ionospheric modification experiments at Tromsø, *Journal of Atmospheric and Terrestrial Physics*, 58, 349–368.

- Stubbe, P., and W. S. Varnum (1972), Electron energy transfer rates in the ionosphere, *Planetary and Space Science*, *20*, 1121, doi:10.1016/0032-0633(72)90001-3.
- Stubbe, P., H. Kopka, and R. L. Dowden (1981), Generation of ELF and VLF waves by polar electrojet modulation Experimental results, *J. Geophys. Res.*, *86*, 9073–9078, doi:10.1029/JA086iA11p09073.
- Stubbe, P., H. Kopka, M. T. Rietveld, and R. L. Dowden (1982), ELF and VLF wave generation by modulated HF heating of the current carrying lower ionosphere, *Journal of Atmospheric and Terrestrial Physics*, *44*, 1123–1131.
- Sun, W., Y. Kamide, J. R. Kan, and S. I. Akasofu (1993), Inversion of the auroral electrojet from magnetometer chain data based on the Flexible Tolerance method, *J. Geomag. Geoelect.*, *45*, 1151.
- Thorne, R. M., and T. R. Larsen (1976), An investigation of relativistic electron precipitation events and their association with magnetospheric substorm activity, *J. Geophys. Res.*, *81*, 5501–5506, doi:10.1029/JA081i031p05501.
- Tomko, A. A. (1981), Nonlinear phenomena arising from radio wave heating of the lower ionosphere, Ph.D. thesis, Pennsylvania State Univ., University Park, PA.
- Velikhov, E., A. Zhamaletdinov, A. Shevtsov, A. Tokarev, Y. Kononov, L. Pesin, G. Kadyshevich, M. Pertel, and A. Veshchev (1998), Deep electromagnetic studies with the use of powerful ELF radio installations, *Izvestiya, Physics of the Solid Earth*, *34*, 615–32.
- Wait, J. R., and K. Spies (1964), Characteristics of the earth-ionosphere waveguide for VLF radio waves, *NBS technical note 300*, National Bureau of Standards.
- Wanke, M., and M. Lee (2011), The terahertz frontier, *Spectrum, IEEE*, *48*(9), 44–61, doi:10.1109/MSPEC.2011.5995900.
- Wilkinson, D., and M. J. Heavner (2006), Geophysical Institute Magnetometer Array, *AGU Fall Meeting Abstracts*, pp. B1417+.

- Ziener, R. (1967), Error probabilities due to additive combinations of gaussian and impulsive noise, *IEEE Transactions on Communication Technology*, 15(3), 471–474, doi:10.1109/TCOM.1967.1089608.